Developing Small-scale Quantum Information Processors based on Electronic Spins in Diamond

by

Won Kyu Calvin Sun

B.AS., Nanotechnology Engineering, University of Waterloo (2014)

Submitted to the Department of Nuclear Science and Engineering
in partial fulfillment of the requirements for the degree of

Doctor of Philosophy in Quantum Science and Engineering

at the

MASSACHUSETTS INSTITUTE OF TECHNOLOGY

September 2021

Author .....
Department of Nuclear Science and Engineering
August 31, 2021

Certified by .....
Paola Cappellaro
Professor of Nuclear Engineering and Professor of Physics
Thesis Supervisor

Certified by .....
William D. Oliver
Professor of Electrical Engineering and Computer Science and Professor of Physics
Thesis Reader

Accepted by .....
Ju Li
Battelle Energy Alliance Professor of Nuclear Science and Engineering
and Professor of Materials Science and Engineering

Developing Small-scale Quantum Information Processors based on Electronic Spins in Diamond

by

Won Kyu Calvin Sun

Submitted to the Department of Nuclear Science and Engineering
on August 31, 2021, in partial fulfillment of the
requirements for the degree of
Doctor of Philosophy in Quantum Science and Engineering

Abstract

Isolated optically-active solid-state spins such as the Nitrogen-Vacancy (NV) center in diamond have demonstrated good properties as qubits for quantum information tasks. However, engineering larger quantum registers around a central NV enables more powerful applications. For example, a register of nuclear spins around the NV has already demonstrated many quantum protocols such as quantum error correction and entanglement distillation. Still, thanks to their stronger coupling to the NV and external fields, a register of electronic spins would enable new complementary applications, such as quantum enhanced sensing and scalable architectures for quantum computation.

In this thesis, three critical steps are demonstrated toward the goal of developing a small-scale quantum information processor based on electronic spins in diamond.

First, we develop a method to systematically scale up a system of electronic spins starting from one qubit – the optically-addressable NV – by characterizing the Hamiltonian of nearby optically-dark electron-nuclear spin defects in its microscopic environment. The knowledge of the system Hamiltonian, which characterizes spin defects in the solid, further enables coherent control over the system.

Second, we characterize the quantum register of electronic spins with respect to two important aspects: entanglement and decoherence.

As entanglement is critical to many quantum information tasks, an accurate characterization of entanglement generated by a quantum device is desired. Therefore, to improve upon the conventional entanglement witness based on the state fidelity, we develop a new metric, called the subspace witness, that is more robust in the presence of local unitary control errors. The subspace witness, at the cost of additional measurements, is insensitive to any combination of single-qubit phase errors accrued during the state-preparation-and-measurement of the target entangled state.

Furthermore, as the power of quantum devices is limited by decoherence, a practical (i.e., classical) and predictive noise model for the device is desired. As the first step to characterize the coherence of a multi-qubit register, we demonstrate a method to build a self-consistent classical noise model for individual qubits. For the NV qubit,

well isolated from the bath, it is possible to develop a self-consistent model, which not only characterizes the bath but can help develop more robust quantum gates and circuits. However, for a nearby qubit, this is not possible due to a possibly a more complex and quantum bath for this qubit – which, after future investigation, may further scale up the size of the quantum register.

Finally, to demonstrate the potential advantage of an electronic spin register, we implement a quantum information task in sensing of external fields. The electronic spins serve to enhance the sensitivity not only via entanglement, but also through a repetitive readout scheme. This result paves the way towards practical quantum advantage in sensing.

The methods and results presented in this thesis outline a path toward developing small-scale quantum registers based on electronic spins in diamond and demonstrate their practical applications to enhance a broad range of tasks in quantum information processing.

Thesis Supervisor: Paola Cappellaro
Title: Professor of Nuclear Engineering and Professor of Physics

Thesis Reader: William D. Oliver
Title: Professor of Electrical Engineering and Computer Science and Professor of Physics

Acknowledgments

My Ph.D. journey and this thesis have been made possible due to the generous and incredible help of many.

First and foremost, I would like to thank my advisor Prof. Paola Cappellaro, without whom I would not be where I am today. From the beginning of my Ph.D. to the end, she has provided continual support and guidance, with much patience and encouragement needed for me to learn and grow. Academically, she has been a thoughtful and dedicated mentor at every interaction, guiding me through every project in my (many) setbacks or detours; theoretical gaps; and experimental obstacles. She believes in and wants good for every student, both academically and personally. I am incredibly grateful to have had her as my advisor, and while I still have much to learn, I hope that I could emulate her more in the future.

I would also like to thank my thesis committee members.

First, I am very grateful for Prof. Dirk Englund, who has supported me from the start of my Ph.D. candidacy. Through regular meetings, I have been encouraged by his point to always ask questions and to make observations on which were of practical significance or potential directions for future investigation. His incredible multidisciplinary knowledge and openness in research have made every interaction very exciting and enjoyable.

I am also very grateful for Prof. Mingda Li, whom I first met in my first graduate course at MIT and who has been answering my many (simple) questions even from day one. In my research discussions with Prof. Mingda Li, I have benefitted not only from his many insightful questions as well as potential solutions for the challenges I discussed but also from his kindness and encouragement. As well, I am very grateful for his openness to guide and advise not only in but also outside of research.

As well, I am very grateful for Prof. William D. Oliver, who has kindly accepted to be the thesis reader despite my last-minute request. Despite my unfortunate timing, he has already provided thoughtful and important feedback in my presentation of the defense and thesis. Given our latest interest and work on noise spectroscopy, I believe

I would further benefit from his insight and expertise.

Finally, I am also very grateful for Prof. Bilge Yildiz, who has supported me as not only the defense chair but also my committee member at the start of my Ph.D. even though I was not in her field. From our meetings she has given me important feedback on presenting before an audience outside of my field; as well her insightful questions on our work on system identification of unknown spin defects has broadened my understanding of the work beyond its results.

I have also many colleagues to thank, both in and outside of QEG.

First I would like to thank the generation of QEG before me who have helped me immensely. First, I would like to thank my mentor Alexandre Cooper, who has taught me everything I needed to know to take on my work with electronic spins in diamond. His theoretical knowledge and experimental acuity in the lab, combined with his attitude towards work and openness to invite and collaborate with others, have always amazed me. I have also benefitted from Alex's help in many ways outside the lab, starting from his help in arriving at MIT (as a fellow Canadian), advice about future directions after grad school, or sporadic discussions about life. I would also like to thank Jean-Christophe Jaskula, who has also supported me in the lab in my troubles with the optics or electronics. I have benefitted from not only his in-depth understanding of and comfort in analyzing and debugging experimental setups and codes, but also many discussions outside the lab with his wide range of knowledge both in and outside of physics. As well, I would also like to thank other senior members of QEG, with whom I did not get to work with but still learned from and enjoyed many discussions in or outside the office: Masashi Hirose, Ashok Ajoy, Kasturi Saha, Luca Marseglia, and Xuan (Ken) Wei.

Second, I am also very grateful for my generation (or office mates) of QEG: Akira Sone, YiXiang Liu, Mo Chen, David Layden, and Scott Alsid. They have continually inspired and supported me from their lives in and outside the lab. I've first worked with and learned from Mo the basics on how to run experiments systematically – and since then enjoyed and learned from many discussions and his explanations; I've benefitted greatly from Akira and YiXiang's help in surviving the quals and classes

and enjoyed many physics lessons from them; I've always been inspired by David's wealth of knowledge and ability to communicate it clearly, as well as by Scott's fierce work ethic, cheery attitude, and insatiable hunger for physics. Outside of work, especially in times of personal difficulty, I've benefitted especially from my office mates YiXiang, Mo, and Akira by their help and care.

I am also very grateful for the younger generation of QEG – Changhao Li, Pai Peng, Guoqing Wang, Abtin Ameri, and Yuan Zhu – who are not only incredibly brilliant but also always open for help and discussions. They have taught and inspired me greatly throughout my time at QEG.

Finally, I would also like to thank many other colleagues I've had the chance to interact with. First I would like to thank Joonhee Choi, from whom I've learned greatly not only through his work but also his advice on future directions. I am also grateful to many others: Christopher Foy, Emma Rosenfeld, Junghyun (Paul) Lee, and Kristine Rezai for discussions on NV centers and/or dark spins in diamond; to Zhenjie Yan and Sergio Cantu for their help in diagnosing and improving the optical setup; and Alex Keeling, Joonhee, and Christian Nguyen as Phys 271 TFs for teaching and leading many interesting discussions outside the class.

I would also like to thank all the NSE office and administrative assistants who have helped me from my first visit to MIT to my setting up for the defense: Brandy Baker, Clare Egan, Heather Barry, Peter Brenton, Lisa Magnano-Bleheen, Dianne Lior, Chihiro Watanabe, Janice Balzer. I would especially like to thank Brandy who has supported me immensely in the last few months to make my graduation possible.

As well I am grateful for all my friends from and outside MIT who have made my time at MIT more enjoyable. Aside from the many highlight moments with QEG (at the NanoMRI conference at the University of Waterloo; QEG dinners; and Akira's wedding), the enjoyable trips with friends from NSE (at the Atomic Retreat and the many road trips with Max Carson and YiXiang) as well as my involvement at Ashdown (especially being in AHEC with Lisa Guay, Chris Foy, Andrew Rzeznik, Sai Gautam Gopalakrishnan, and Orpheus Chatzivasileiou) have marked special moments at MIT. I am also very grateful for Doug Lauffenburger who has made time for me

regarding my questions about MIT and also welcomed me when I first arrived. I am also grateful for Adam Mabry and many others from Aletheia Church as well as fellow students at Harvard or MIT who have answered my many questions about life and God.

Finally, I would like to thank my parents, Keum Hee Lee and Hee Joo Sun, most especially for loving me more than I could ever do myself. Their continual support in every way they can I am very grateful for; and their desire for and rejoicing in my good has made life more meaningful. I am also grateful to my sister Kyung Eun Kate Sun who has not only overcome a difficult period in her life but also has filled in these last few years to support my family in Korea during difficult times.

Finally, I would like to thank God for the entire journey thus far, in both the ups and downs and perhaps most especially for giving me the people I needed along the way so that, while still far from perfect, I could get to where I am today.

Contents

List of Figures

List of Tables

Chapter 1

Introduction

1.1 Thesis Overview

The objective of this Thesis is to develop a small-scale, general-purpose quantum information processor based on electronic spins in diamond – starting from a single Nitrogen-Vacancy (NV) center in diamond.

While a single NV center in diamond has proved a great candidate for quantum sensing [112, 106, 20] and quantum communication networks [97, 113, 92], a single NV with a register of (optically) dark spins has enabled more powerful applications. Predominantly, a *nuclear* spin register around a central NV qubit has thus far demonstrated enhanced quantum memory [93, 52], quantum error correction [110, 24], and multi-qubit quantum information protocols [58, 118].

In this work, we wish to develop a coherent register of dark *electronic* spins around the NV. Thanks to stronger coupling to the NV and to external fields, an electronic spin register would enable novel, complementary applications, e.g., in enhanced sensing protocols (e.g., to achieve quantum advantage [22] or increase the range of nanoscale sensing [106]), quantum error correction, and scalable architectures for quantum computation [123, 122, 90, 100].

We present our work towards this objective in three steps – schematically outlined in Fig. 1-1 – divided into Chapters 2, 3, and 4.

In Chapter 2, we systematically scale up a system of interacting electronic spins,

starting from a single NV center in diamond interacting with unknown electron-nuclear spin defects. To achieve this, we first develop a general method to identify the interaction Hamiltonian of unknown spins via sweeping an external static magnetic field. Then, applying this method, we identify the hyperfine interaction Hamiltonian of two electron-nuclear spin defects (to denote as X spins) interacting with a particular NV center, as well as the dipolar coupling between the NV and X electronic spins. The knowledge of the Hamiltonian not only characterizes the electron-nuclear spin molecule in solid (via hyperfine interaction) and the relative spatial positions (via dipolar coupling), but also allows coherent control over the quantum register.

In Chapter 3, given a controllable quantum register of electronic spins, we characterize the performance of this quantum register. More specifically, we characterize the entanglement generated as well as the decoherence (noise) experienced by this quantum device.

In Chapter 3.1, to characterize entanglement, we develop a novel metric, called the subspace witness, in order to more accurately detect the entanglement generated with respect to the conventional entanglement witness based on state fidelity. The subspace witness, at the cost of additional measurements, becomes insensitive to any combination of single-qubit phase errors accrued during the quantum circuit preparing and measuring the target entangled state. Indeed, for two-qubit entanglement, we theoretically demonstrate – and experimentally verify with NV and X electronic spins – the advantage of the subspace witness. For genuine multipartite entanglement, the subspace witness can still be very efficient in the number of measurements required depending on the target entangled state; furthermore, the subspace witness, beyond entanglement detection, also facilitates lower bound estimation of entanglement via the metric called GME concurrence.

In Chapter 3.2, as the first step to characterize the noise affecting a multi-qubit register, we demonstrate a protocol to build a self-consistent classical noise model for individual qubits. By performing noise spectroscopy of both NV and X electronic spins, we report two results. First, for the NV qubit which is well isolated (distinguished) from the bath, it is possible to build a noise model that is self-consistent

or predictive over a varied set of dynamics – indicating an accurate characterization of the bath. However, for the nearby X qubit, it is not possible – rather, we find evidence for a more complex and quantum bath for the X qubit that precludes a self-consistent classical noise model. This bath of X, which may contain a group of coherently interacting electronic spins, may be of interest for future investigation – in order to further scale up the electronic spin register.

Finally, in Chapter 4, putting this device to the test we implement a quantum information task in quantum sensing. Utilizing a two-qubit electronic spin register, we demonstrate environment-assisted sensing of external classical fields to achieve practical quantum advantage in two steps. As the first step, we experimentally demonstrate sensitivity enhancement via entanglement, but find that it is insufficient to overcome the 'cost' of generating and maintaining the entangled state to allow quantum advantage. Therefore, to make one more step towards quantum advantage, we further enhance the sensitivity by repurposing the second electronic spin (after entangled sensing) as a classical memory register. This allows repetitive readout of the sensed information, enhancing the sensitivity by another factor of SNR. Enhancing the sensitivity by entanglement and memory, the electronic register paves the path towards practical quantum advantage in sensing.

In order to streamline the presentation and discussion of results in Chapter 2, 3, and 4, in this Chapter we present the relevant background.

In Section 1.2, we first give a general overview of electronic spins in diamond, namely that of the NV and dark electronic spins, with which we build our quantum register.

In Section 1.3, we review the experiments commonly performed with such spins and as well used throughout the Thesis.

In Section 1.4, we review the metric of interest for sensing, called the sensitivity, as background for quantum sensing in Chapter 4.

In Section 1.5, we give the background for noise spectroscopy as relevant for the characterization of noise affecting a nanoscale quantum device composed of electronic spins in Chapter 3.2.

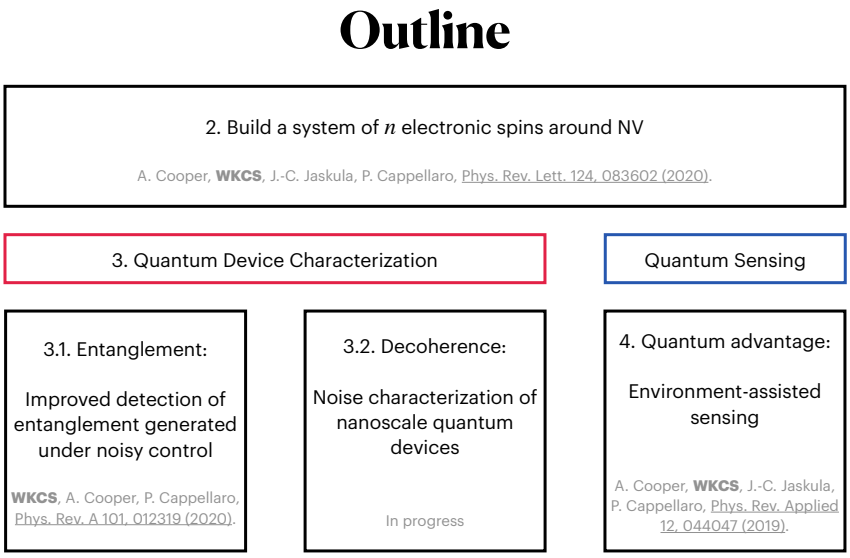

Figure 1-1: **Thesis Outline** Towards the goal of developing a quantum register of electronic spins around a central NV, three critical steps are demonstrated in this Thesis. First, we systematically build up a system of dark electronic spins around a central NV (Chapters 2). We then characterize the performance of the nanoscale quantum device composed of interacting electronic spins (Chapter 3). Finally, to demonstrate the advantages of engineering an electronic spin register, we implement a quantum information task in sensing to achieve practical quantum advantage (Chapter 4).

1.2 Electronic Spins in Diamond

Given our goal to develop small-scale quantum information processors based on electronic spins in diamond, in this section we present a limited review of existing electronic spins in diamond. More specifically, we review the main spin defects of interest, namely the NV center and the (optically) dark electronic spins in diamond.

In Section 1.2.1, we review the properties of a Nitrogen-Vacancy (NV) center in diamond that are attractive a building block – qubit – of quantum information processors.

In Section 1.2.2, we briefly review the existing literature on optically dark electronic spins in diamond, which could be engineered as a quantum register around a central NV. While most earlier works studied ensembles of electronic spins in diamond – and their cause of decoherence for the NV – in more recent years works on electronic spins isolated (distinguishable) from the bath and interacting with a nearby NV have been reported – noting their potential to form a coherent register of electronic spins. However, still much work is required to advance the capabilities of an electronic spin register, namely in the identification of the various possible electronic spin defects in a solid (Chapter 2), characterization of such nanoscale quantum devices of electronic spins (Chapter 3), and development of coherent control for implementation of quantum information tasks of interest (Chapter 4). We will address such steps throughout the rest of the Thesis.

1.2.1 Nitrogen-Vacancy (NV) centers in diamond

The Nitrogen-Vacancy (NV) center in diamond is a defect in diamond formed by a substitutional nitrogen and an adjacent vacancy site in diamond (Fig 1-2). To see why an NV center makes a good qubit, we refer to the DiVincenzo criteria [33] which outline the requirements of a good building block (qubit) for a quantum information processor: namely, the qubit should form an isolated two-level system that can be initialized, coherently manipulated, and readout.

In most literature, the 'NV center' refers to the negatively charged state of the NV

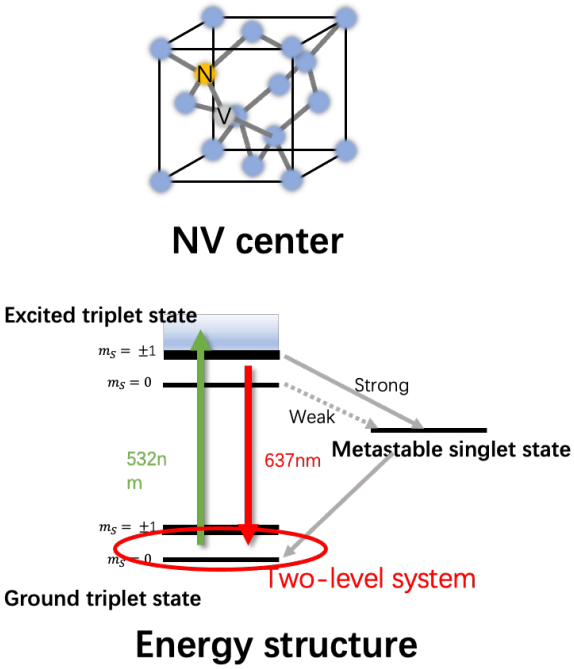

Figure 1-2: **Nitrogen-Vacancy (NV) centers in diamond** (Top) Schematic of a nitrogen-vacancy center inside the carbon matrix of diamond. (Bottom) Energy levels of an NV center. *Courtesy of Guoqing Wang.*

center that forms an electronic spin $S = 1$ system in its optical ground state (Fig 1-2). Therefore, the NV center makes a three-level system (qutrit) given the three magnetic sublevels $m_s = \{0, \pm 1\}$, where the $m_s = \pm 1$ sublevels are degenerate at zero external magnetic field. However, the NV center also makes a more convenient two-level system (qubit) in the presence of an external field (which splits the $m_s = \pm 1$ sublevels), given that an isolated two-level system (e.g., $m_s = \{0, -1\}$) can be identified.

As well, the spin state of the NV center can be readily initialized and readout optically [99]. By an excitation laser (typically in green at 532 nm), the spin state of the NV can be initialized to the $m_s = 0$ state, preparing a quantum state with high purity. This optical pumping into the $m_s = 0$ state occurs due to an intersystem crossing in the optical excited state of the NV (Fig 1-2). More specifically, the $m_s = \pm 1$ states in the excited state undergo a non-radiative non-spin-conserving decay, through the spin singlet state, to the optical ground state – at a higher rate than that of the $m_s = 0$. Therefore, after a finite duration of a green laser pulse, the NV

electronic spin state is initialized to $m_s = 0$. Furthermore, by the same intersystem crossing, the spin state of the NV center can also be readout: given the preferential decay of $m_s = \pm 1$ states through the non-radiative (less bright) channel, the rate of fluorescence measured in a time interval can distinguish between $m_s = 0$ and $m_s = \pm 1$.

Finally, the spin state of the NV center can be coherently manipulated by an external microwave on resonance with the two magnetic sublevels forming the qubit.

Combined with optical and room-temperature stability, as well as a nuclear spin degree of freedom from the native nitrogen $^{14(15)}N$, the properties of the NV center make it an attractive qubit platform.

Thus far, the NV center has been utilized to demonstrate state-of-the-art performance in many quantum sensing and communications tasks. The electronic spin of the NV center, thanks to the dependence of its internal Hamiltonian to external physical quantities such as magnetic field [112, 20, 106], temperature [81, 65, 119, 71], electric field [35, 10] and strain [115, 86, 16, 61], has been applied as a versatile sensor. As well, given its optical interface as well as a native nuclear spin register, it has demonstrated quantum information protocols as required to form practical quantum communication networks [97, 113, 92].

1.2.2 Dark electronic spins in diamond

While an isolated NV center is a powerful qubit, more powerful and interesting applications can be achieved with a quantum register around a central NV. With our focus on developing a register of dark electronic spins, here we give a brief and limited review of existing literature on dark electronic spins in diamond.

The first and most prominent ensemble of electronic spins encountered for the NV center is of substitutional nitrogen defects in diamond, called P1 centers [48, 34, 109, 28, 29, 120, 79, 94]. Their ubiquity may be explained by the NV fabrication process. To create NV centers in diamond, nitrogen ions are introduced into the diamond (either via ion implantation or during chemical vapor deposition); given that the typical conversion efficiency of the nitrogen to NV center is below 10% [80, 98, 85],

the non-NV nitrogens could form the substitutional defects contributing to the larger electronic spin bath. And this bath has been shown to be the dominant source of decoherence for the NV centers over a large range of concentration [120, 5, 6]. With respect to their potential to form coherent registers for the NV, given that an ensemble of indistinguishable spins makes for a nontrivial system to control, not much progress has been made in this direction thus far, except a few early works reporting the discovery of coherent coupling between a single NV and a single N defect [39, 49]. However, in the last year, a pioneering experiment to isolate, coherently control, and generate entanglement between individual P1 centers from the larger spin bath was demonstrated [32], confirming the potential to build quantum registers out of a bulk spin bath.

Aside from the P1 bath, a bath of 'surface' spins has been identified due to the engineering of shallow NV centers given the interest in nanoscale sensing of single molecules on the surface. In addition to the P1 bath, the surface spin bath acts as another dominant source of decoherence for shallow NVs [79, 94, 78]. While a bath of spins is difficult to utilize as a coherent register, nonetheless a potential advantage of an electronic spin register was demonstrated earlier on with the surface spins. More specifically, in a pioneering experiment, given a system of NV and a coherently coupled surface spin, the surface spin acted as a 'reporter' spin that extended the sensing volume of the shallow NV center – and reported the first detected signal arising from a single proton spin [106].

However, due to the difficulty of working with an ensemble of spins – which tends towards a spin bath causing decoherence – a system of isolated electronic spins (distinguishable from the bath) is desired for the goal of developing a coherent register of electronic spins. To this end, in recent years, there have been increasing interest in engineering electronic spin defects, either inside diamond or on the surface, and to subsequently identify and control the (un)known electronic spins coherently coupled to the NV [63, 100, 95, 91].

Still, much work is required to advance the capabilities of a quantum register of electronic spins. First, a general method to characterize the (a priori unknown)

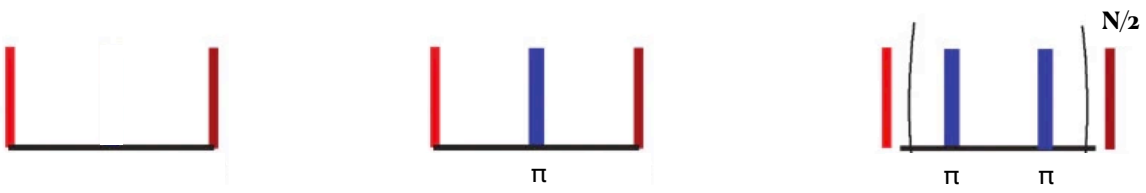

Figure 1-3: **Pulse Sequence of Common Single-qubit Experiments** (Left) Ramsey. (Center) Spin Echo. (Right) CPMG with N cycles. *Adapted from [112].*

electronic spin defect in a solid is desired, not only to increase the library of various possible electronic spin defects in the solid but also enable coherent control over the initially unknown spin – this will be the topic of Chapter 2. Then, given a controllable quantum register of electronic spins, characterization of such quantum devices, as any other quantum device, is desired – this will be the topic of Chapter 3. Finally, to demonstrate the advantages of engineering an electronic spin register, implementation of quantum information tasks is desired – this will be the topic of Chapter 4.

In the next section, we review the most common experiments performed with such single-qubit (and two-qubit) systems: namely the Ramsey, Spin Echo, and CPMG.

1.3 Most Common NV Experiments

The goal of this section is to introduce the most common single-qubit experiments, namely the Ramsey, Spin Echo (or Echo for short), and CPMG experiments, that are also utilized throughout the Thesis. In Chapter 3.2, Ramsey, Echo and CPMG are used to reveal information about the qubit bath; we discuss how in Section 1.5. In Chapter 4, the Echo experiment is used to compare the performance of a single-qubit sensor vs. a two-qubit entangled sensor in order to demonstrate quantum advantage in sensing. Finally, in Chapter 2, a modified echo – called Spin Echo Double Resonance (SEDOR) or Double Electron-Electron Resonance (DEER) experiments – is used to reveal the spectrum of the Hamiltonian of unknown interacting spins.

In this section, we will first discuss the role of each experiment, as intended, for a single isolated qubit. But given our interest in a coherent register of electronic spins with a central NV, we will also discuss their role (either in original or modified form)

given a system of two heterogeneous, interacting electronic spins. To streamline the discussion of the significance of each experiment, we begin by reviewing the pulse sequence for each experiment and review the necessary mathematical background to better understand each experiment.

The pulse sequences of Ramsey, Echo, and CPMG (Fig. 1-3) show they are composed of the same building blocks: namely, the same state preparation (red $\pi/2$-pulse), free evolution under the Hamiltonian, π-pulse(s) as appropriate, and a final $\pi/2$-pulse to readout the remaining qubit coherence. Let us discuss the purpose of each block.

The first $\pi/2$-pulse – i.e., a qubit rotation by $\pi/2$ – exists to prepare a coherent superposition state, assuming the initial state $\rho_0 = |0\rangle\langle 0| = (\mathbb{I} + \sigma^z)/2$. Here $\mathbb{I}$ is the identity operator, and σ^α, with $\alpha = \{x, y, z\}$, is the single-qubit Pauli operator. Therefore, the first $\pi/2$-pulse, defined as the rotation $R_y(\theta{=}\pi/2) = e^{-i\theta\sigma^y/2}$, prepares the following initial state ρ_i:

$$\begin{aligned}\rho_i &= R_y(\pi/2)|0\rangle\langle 0|R_y^\dagger(\pi/2),\\ &= (\mathbb{I} + R_y(\pi/2)\sigma^z R_y^\dagger(\pi/2))/2,\\ &= (\mathbb{I} + \sigma^x)/2.\end{aligned}$$

Similarly, the last $\pi/2$-pulse exists to readout the remaining coherence at time T, assuming the available measurement operator $M = \sigma^z$ reads the population at the end of the pulse sequence. Thus, with the last $\pi/2$-pulse, the effective measurement operator becomes:

$$M = R_y^\dagger(\pi/2)\sigma^z R_y(\pi/2) = \sigma^x,$$

measuring the coherence as desired.

Let us now discuss the free-evolution unitary operator U_n present in each experiment, for the single-qubit $n = 1$ and two-qubit $n = 2$ case.

For the single qubit, its lab frame Hamiltonian is given by $H_{lab} = \omega_0/2\sigma^z + \Omega_0\cos(\omega t)\sigma^x$, where $\Omega_0 \neq 0$ when a pulse is applied. Then, with the Rotating Wave

Approximation, the rotating frame Hamiltonian is given by $H = \delta/2\sigma^z + \Omega_0/2\sigma^x$, where the detuning $\delta = (\omega_0 - \omega)$. Thus during free evolution ($\Omega_0 = 0$), the relevant single-qubit unitary U_1 is:

$$U_1(T) = e^{-iHT} = e^{-i(\delta T/2)\sigma^z}.$$

Now, for two interacting qubits, its lab frame Hamiltonian is given by $H_{lab} = \sum_{k=1,2} \omega_{0,k}/2\sigma_k^z + H_{int}$, where $k = 1, 2$ refers to the k-th qubit. For convenience, we drop the k label when only discussing single-qubit experiments as shown above (and below).

For two electronic spin qubits, H_{int} is given by the dipolar interaction; however, given a large energy mismatch between the two spins $|\omega_{0,1} - \omega_{0,2}| \gg ||H_{int}||$, we can make the so-called secular approximation, i.e., to keep only the terms in H_{int} that commute with the internal Hamiltonian. This secular approximation, allowing $H_{int} \approx d/2\sigma_1^z\sigma_2^z$, is equivalent to assuming energy conservation during the state evolution. Now, in the rotating frames at the resonance of each spin, the Hamiltonian is $H = H_{int}$, such that the relevant two-qubit unitary U_2 during free evolution is:

$$U_2(T) = e^{-iHT} = e^{-i(dT/2)\sigma^z\sigma^z}.$$

We are now ready to calculate the resulting signal $S(T) \equiv \mathrm{Tr}\{M\rho(T)\}$ measured after each experiment, beginning with the simplest experiment.

Ramsey Recall that Ramsey (Fig. 1-3), aside from the two $\pi/2$-pulses for state preparation and measurement, is a free evolution. Therefore, the total unitary under Ramsey $U_R(T) = U_1(T)$, which yields the state

$$\begin{aligned}
\rho_R(T) &= U_1(T)\rho_i U_1^\dagger(T), \\
&= (\mathbb{I} + U_1(T)\sigma^x U_1^\dagger(T))/2, \\
&= (\mathbb{I} + \sigma^x \cos(\delta T) + \sigma^y \sin(\delta T))/2.
\end{aligned}$$

Therefore, the measured signal after Ramsey is:

$$\begin{aligned} S_R(T) &= \mathrm{Tr}\{M\rho(T)\}, \\ &= \mathrm{Tr}\{\sigma^x \rho_R(T)\}, \\ &= \cos(\delta T). \end{aligned}$$

In other words, the Ramsey experiment yields information about the qubit detuning $\delta = (\omega_0 - \omega)$ between the qubit resonance ω_0 and the applied drive ω. Hence, Ramsey is typically used to calibrate the frequency of the qubit driving.

Now, in the presence of a non-degenerate qubit interacting with the above driven qubit, the Ramsey can be used to detect the presence of such a spin. For simplicity, let us assume a good calibrated driving for the first qubit ($\delta = 0$) and that the unknown qubit is in thermal equilibrium, such that $\rho_i = \rho_{i,1} \otimes \rho_{i,2} = |0\rangle\langle 0| \otimes \mathbb{I}/2$. The resulting state after the Ramsey experiment is:

$$\begin{aligned} \rho_R(T) &= U_2(T)\rho_i U_2^\dagger(T), \\ &= (\mathbb{I} + U_2(T)(\sigma_1^x \otimes \mathbb{I})U_2^\dagger(T))/4, \\ &= (\mathbb{I} + \sigma_1^x \cos(dT) + \sigma_1^y \sigma_2^z \sin(dT))/4. \end{aligned}$$

Therefore, the measured signal after Ramsey is:

$$\begin{aligned} S_R(T) &= \mathrm{Tr}\{M\rho(T)\}, \\ &= \mathrm{Tr}\{(\sigma_1^x \otimes \mathbb{I})\rho_R(T)\}, \\ &= \cos(dT). \end{aligned}$$

In other words, the Ramsey experiment yields information about the dipolar coupling strength d in the presence of an interacting spin. While the above closed system of two qubits yields a non-decaying signal, for an open system, the qubit coherence Ramsey will decay with characteristic decay time T_2^*. Thus, in practice, Ramsey can be used to detect for 'strongly' coupled spin, with $(dT_2^*) > 1$.

Of course, there may very well exist 'weakly' interacting spins, with $(dT_2^*) < 1$, that will not be detected by Ramsey. We will see how such weakly coupled spins may be detected at the end of this section.

Here, note that the measurement operator M acts only on the first qubit – representing the optically-active NV center – while the second qubit – representing a nearby dark spin – is not measured by the green laser pulse.

Spin Echo The pulse sequence for the Echo (Fig. 1-3), aside from the two $\pi/2$-pulses for state preparation and measurement, consists of a free evolution with a π-pulse in the center.

Therefore, the total unitary under (single-qubit) Echo is $U_E(T) = U_1(T/2)\sigma^x U_1(T/2)$, which can be simplified to

$$\begin{aligned} U_E(T) &= U_1(T/2)\sigma^x U_1(T/2), \\ &= \mathbb{I}U_1(T/2)\sigma^x U_1(T/2), \\ &= \sigma^x(\sigma^x U_1(T/2)\sigma^x)U_1(T/2), \\ &= \sigma^x U_1'(T/2)U_1(T/2), \\ &= \sigma^x U_1(-T/2)U_1(T/2), \\ &= \sigma^x \mathbb{I}. \end{aligned}$$

Here, in the third equality, we used the relation $\mathbb{I} = \sigma^x\sigma^x$; in the fourth equality we defined $U_1'(T/2) = \sigma^x U_1(T/2)\sigma^x = e^{-i(\delta T/2)\sigma^x\sigma^z\sigma^x} = e^{+i(\delta T/2)\sigma^z} = U_1(-T/2)$.

Therefore, while a non-zero detuning $\delta \neq 0$ can occur during free evolution because of noise from the bath, the Echo cancels out such quasi-static (low frequency) noise experienced by the qubit – resulting in a unitary evolution independent of δ: $U_E(T) = \sigma^x$. Here, the noise $\delta \neq 0$ is quasi-static or low frequency if slowly varying with respect to the total echo time T.

Therefore, the state after Echo is:

$$\begin{aligned}\rho_E(T) &= U_E(T)\rho_i U_E^\dagger(T),\\ &= \sigma^x\rho_i\sigma^x,\\ &= (\mathbb{I}+\sigma^x\sigma^x\sigma^x)/2,\\ &= \rho_i.\end{aligned}$$

This yields a constant signal:

$$\begin{aligned}S_E(T) &= \mathrm{Tr}\{M\rho(T)\},\\ &= \mathrm{Tr}\{\sigma^x\rho_E(T)\},\\ &= 1.\end{aligned}$$

Because the Echo is insensitive to any quasi-static detuning during the free evolution, its characteristic coherence time T_2 can be significantly longer than T_2^* of Ramsey if the dominant noise is at low frequency. We will see in our system of two proximal electronic spins, whose dominant noise is at low frequency, T_2 is an order of magnitude longer than T_2^*.

Now, in the presence of a non-degenerate qubit interacting with the above driven qubit, the Echo will cancel out its interaction – similar to the detuning. The total unitary under Echo is $U_E(T) = U_2(T/2)\sigma^x U_2(T/2)$, which can be simplified to

$$\begin{aligned}U_E(T) &= U_2(T/2)\sigma_1^x U_2(T/2),\\ &= \sigma_1^x(\sigma_1^x U_2(T/2)\sigma_1^x)U_2(T/2),\\ &= \sigma_1^x U_2'(T/2)U_2(T/2),\\ &= \sigma_1^x U_2(-T/2)U_2(T/2),\\ &= \sigma_1^x\mathbb{I},\end{aligned}$$

where $U_2'(T/2) = e^{-i(dT/2)\sigma_1^x(\sigma_1^z\sigma_2^z)\sigma_1^x} = e^{+i(dT/2)\sigma_1^z\sigma_2^z} = U_2(-T/2)$. In other words, even in the presence of a coherent interacting electronic spin, the Echo cancels out its

interaction – becoming independent of d: $U_E(T) = \sigma^x$.

To calculate the state evolution, again for simplicity let us assume a good calibrated driving for the first qubit ($\delta = 0$) and that the unknown qubit is in thermal equilibrium, such that $\rho_i = \rho_{i,1} \otimes \rho_{i,2} = |0\rangle\langle 0| \otimes \mathbb{I}/2$. The resulting state after the Echo experiment is:

$$\begin{aligned}\rho_E(T) &= U_E(T)\rho_i U_E^\dagger(T), \\ &= (\mathbb{I} + \sigma_1^x(\sigma_1^x \otimes \mathbb{I})\sigma_1^x)/4, \\ &= \rho_i.\end{aligned}$$

Therefore, the measured signal after Echo is:

$$\begin{aligned}S_E(T) &= \mathrm{Tr}\{M\rho(T)\}, \\ &= \mathrm{Tr}\{\sigma^x\rho_E(T)\}, \\ &= 1.\end{aligned}$$

CPMG The pulse sequence of CPMG (Fig. 1-3), aside from the two $\pi/2$-pulses for state preparation and measurement, consists of the spin echo block repeated N times. Defining the inter-pulse duration as 2τ, the total experiment time $T = N(2\tau + L) \approx N(2\tau)$, assuming the π-pulse length $L \ll \tau$.

Therefore, the total unitary under (single-qubit) CPMG, for even N, is $U_{CP}(T) = [U_1(\tau)\sigma^x U_1(2\tau)\sigma^x U_1(\tau)]^{N/2}$, which can be simplified to

$$\begin{aligned}U_E(T) &= [U_1(\tau)\sigma^x U_1(2\tau)\sigma^x U_1(\tau)]^{N/2}, \\ &= [U_1(\tau)U_1(-2\tau)U_1(\tau)]^{N/2}, \\ &= [\mathbb{I}]^{N/2}.\end{aligned}$$

Therefore, the state after CPMG is:

$$\begin{aligned}\rho_{CP}(T) &= U_{CP}(T)\rho_i U_{CP}^{\dagger}(T),\\ &= \rho_i.\end{aligned}$$

This yields a constant signal:

$$\begin{aligned}S_{CP}(T) &= \mathrm{Tr}\{M\rho(T)\},\\ &= \mathrm{Tr}\{\sigma^x\rho_{CP}(T)\},\\ &= 1.\end{aligned}$$

Similar to Echo, CPMG also cancels out any quasi-static or low frequency noise experienced by the qubit, becoming independent of δ: $U_{CP}(T) = \mathbb{I}$. However, as will be seen in Section 1.5, the bandwidth of low frequencies canceled out by CPMG can be made much larger than Echo by decreasing the cycle period (2τ). In turn, by becoming less sensitive to lower frequency noise, the characteristic decay time $T_{2,CP} > T_2$ can be increased than that of Echo.

Finally, also similar to Echo, CPMG also cancels out any coherently interacting spin by the same math as shown above.

Spin Echo Double Resonance (SEDOR) Finally, we discuss a modified version of Echo – called Spin Echo Double Resonance (SEDOR) or Double Electron-Electron Resonance (DEER) experiments – which now drives two spin species. Such SEDOR or DEER experiments can re-introduce the otherwise canceled interaction between two electronic spins via the (single-qubit) echo sequence.

The SEDOR pulse sequence is identical to that of Echo except for an additional π-pulse for the second qubit species, applied at the time of π-pulse for the first qubit, as shown in the inset of Fig. 2-2. This simple change now allows recoupling between

spins, as can be seen by the total unitary under SEDOR $U_S(T)$:

$$\begin{aligned} U_S(T) &= U_2(T/2)\sigma_1^x\sigma_2^x U_2(T/2) \\ &= \sigma_1^x\sigma_2^x(\sigma_1^x\sigma_2^x U_2(T/2)\sigma_1^x\sigma_2^x)U_2(T/2), \\ &= \sigma_1^x\sigma_2^x U_2'(T/2)U_2(T/2), \\ &= \sigma_1^x\sigma_2^x U_2(T/2)U_2(T/2), \\ &= \sigma_1^x\sigma_2^x U_2(T), \end{aligned}$$

where $U_2'(T/2) = e^{-i(dT/2)\sigma_1^x\sigma_2^x(\sigma_1^z\sigma_2^z)\sigma_1^x\sigma_2^x} = e^{-i(dT/2)\sigma_1^z\sigma_2^z} = U_2(T/2)$. In other words, in the presence of a coherent interacting electronic spin, the SEDOR allows evolution under such interaction. Note, if no interacting spin exists at the resonance of the additional π-pulse, SEDOR simply reverts to (single-qubit) Echo since the additional π-pulse does nothing.

Therefore, for the closed system of two coupled electron spins, the SEDOR signal reverts to the Ramsey signal. Again for simplicity, let us assume a good calibrated driving for the both qubits ($\delta = 0$) and that the unknown qubit is in thermal equilibrium, such that $\rho_i = \rho_{i,1} \otimes \rho_{i,2} = |0\rangle\langle 0| \otimes \mathbb{I}/2$. The resulting state after SEDOR is:

$$\begin{aligned} \rho_S(T) &= U_S(T)\rho_i U_S^\dagger(T), \\ &= (\mathbb{I} + U_S(T)(\sigma_1^x \otimes \mathbb{I})U_S^\dagger(T))/4, \\ &= (\mathbb{I} + \sigma_1^x\sigma_2^x(\sigma_1^x\cos(dT) + \sigma_1^y\sigma_2^z\sin(dT))\sigma_1^x\sigma_2^x)/4 \\ &= (\mathbb{I} + (-\sigma_1^x\cos(dT) + \sigma_1^y\sigma_2^z\sin(dT)))/4. \end{aligned}$$

Therefore, the measured signal after SEDOR is:

$$\begin{aligned} S_R(T) &= \mathrm{Tr}\{M\rho(T)\}, \\ &= \mathrm{Tr}\{\sigma^x\rho_S(T)\}, \\ &= -\cos(dT). \end{aligned}$$

In other words, for a closed system of two interacting electronic spins, SEDOR is equivalent to the Ramsey experiment. However, recalling that the coherence time under Echo can be longer than that of Ramsey ($T_2 > T_2$), SEDOR is able to detect spins that cannot be detected via Ramsey. More specifically, SEDOR can also reveal spins with 'weak' coupling strength $|d|$, where $(dT_2) > 1 > (dT_2^*)$.

In fact, our system of electronic spins will be weakly coupled, so as not to be detectable under Ramsey, but revealed and controlled via SEDOR. More specifically, by changing the frequency of the additional π-pulse, we can measure the resonance of the unknown system of electronic spins as seen in Fig. 2-2. As well, by sweeping the interaction time, we can measure the effective dipolar coupling strength d as seen in Fig. 2-4.

In the remaining two sections, we review the relevant background for Chapter 3.2 and Chapter 4.

1.4 AC Magnetomery and Quantum Sensitivity η

One prominent application of isolated NV centers in diamond has been in quantum sensing, i.e., the measurement a physical quantity of interest via the use of a quantum object [31]. Here we review the main metric to characterize the performance of a quantum sensor: sensitivity η.

In Chapter 4, our goal will be to demonstrate practical quantum advantage with an electronic spin register, i.e., to surpass the sensitivity allowed for a single-qubit sensor by use of an additional spin from the environment. With knowledge of η, it will be straight-forward to understand the path towards achieving practical quantum advantage in sensing.

Metric of Interest: Sensitivity η

Here we recall the definition of the sensitivity η of a sensor:

$$\eta \equiv \frac{\sigma_S}{\left|\frac{dS}{db}\right|_{max}} \frac{1}{\sqrt{N}} \tag{1.1}$$

Here S is the signal yielded by the sensor (whose exact form depends on the specific sensing protocol), σ_S the uncertainty or noise in the signal S, b the parameter of interest to be sensed, and N the number of repeated measurements.

To better understand this metric, let us first for simplicity consider sensitivity at $N = 1$, i.e., $\eta_{N=1} = \frac{\sigma_S}{\left|\frac{dS}{db}\right|_{max}}$. This quantity compares the optimal rate of change $\left|\frac{dS}{db}\right|_{max}$ of the sensor signal vs. its uncertainty σ_S. Therefore, the smaller this quantity, the more sensitive the sensor is to a change in the parameter of interest.

Now, given a fixed total experiment time T, one can improve the sensitivity by repeating the sensing protocol $N = T/(\tau + t_d)$ times to achieve $\eta = \eta_{N=1}/\sqrt{N}$. Here, each sensing protocol takes time τ for sensing while also requiring idle time t_d to both initialize and reset the sensor for another iteration.

Signal of Interest: AC Magnetometry $S(b)$

The specific sensing task used to compare the performance of the single-qubit vs. environment-assisted sensor will be spin-echo ac magnetometry [75, 112, 67, 27, 20], which we briefly review.

The goal of spin-echo ac magnetometry is to estimate the unknown field strength b of an external oscillating B-field: $b(t) = b\sin(\omega t + \phi)$. Its protocol, as the name suggests, is to subject the qubit sensor to a spin-echo sequence of duration τ in the presence of $b(t)$. Then the qubit gains a phase $\phi = \phi(b)$ carrying information of the parameter of interest b.

More specifically, for a qubit initially in $|\psi\rangle = \frac{|0\rangle+|1\rangle}{\sqrt{2}}$, the resulting signal is [75,

112, 67, 27, 20, 22]:

$$S_1(\tau) = \alpha_1(\tau)\sin(\phi(b)), \tag{1.2}$$

$$\alpha_1(\tau) \equiv \alpha_1(0)e^{-\chi_1(\tau)},$$

$$\phi(b) = b\gamma_e f\tau, \tag{1.3}$$

where $\alpha_1(\tau) = \langle 0|\rho(\tau)|1\rangle + h.c.$ describes the decoherence of $n = 1$-body (single-qubit) coherence under spin-echo. Due to imperfect control in preparing the sensor state $|\psi\rangle$, or due to state-preparation-and-measurement (SPAM) errors, typically $|\alpha_1(0)| < 1$. Here γ_e is the electronic spin gyromagnetic ratio, and $f \leq 2/\pi$ quantifies the overlap of the sinusoidal $b(t)$ and the spin-echo sequence, which saturates the equality for $\omega\tau = 2\pi$ [22].

This is generalized for the n-maximally entangled state, initially in $|\psi\rangle = \frac{|00..0\rangle + |11..1\rangle}{\sqrt{2}}$, to yield the signal:

$$S_n(\tau) = \alpha_n(\tau)\sin(n\phi(b)), \tag{1.4}$$

$$\alpha_n(\tau) \equiv \alpha_n(0)e^{-\chi_n(\tau)},$$

where now $\alpha_n(\tau) = \langle 00..0|\rho(\tau)|11..1\rangle + h.c.$ describes the decoherence of n-body coherence under spin-echo.

Before moving on, we make a few remarks on the important parameters affecting the resulting sensing signal $S_n(\tau)$.

Perhaps the most important parameter is n, which confirms that the n-maximally entangled sensor is in principle n-times more sensitive to b. In the limit of small b (as is of interest for nanoscale imaging of e.g., single molecules),

$$\sin(n\phi(b)) \sim n\phi(b) \propto nb,$$

$$\left|\frac{dS}{db}\right|_{max} \propto n,$$

i.e., resulting in n-fold increase in sensitivity. In Chapter 4, we will experimentally

verify the $n = 2$ gain with our system over a large range of τ.

The next parameter of interest is the n-body coherence remaining after sensing time τ: $\alpha_n(\tau) \equiv \alpha_n(0)e^{-\chi_n(\tau)}$. It is instructive to piece out a term independent of the sensing task ($\alpha_n(\tau = 0)$), and one dependent ($e^{-\chi_n(\tau)}$).

$\alpha_n(0)$ is *related* to the amount of n-maximally entangled state generated (more exactly it is the amount of n-body coherence generated)—right before the sensing task $\tau = 0$. In other words, the magnitude of $\alpha_n(0)$ depends on the 'goodness' or fidelity of the quantum circuit required to prepare (and then measure) the desired n-entangled state. Any sub-unity $\alpha_n(0) \leq 1$, associated with the larger state-preparation-and-measurement (SPAM) errors for n-entangled states, will cost in sensivity.

Apart from the control errors, the second term $e^{-\chi_n(\tau)} \leq 1$ accounts for decoherence during sensing time τ. Just as n-maximally entangled state is more sensitive to the signal of interest than $n = 1$, it is also more sensitive to noise and thus decoheres faster: $\chi_n(\tau) > \chi_{n-1}(\tau)$. Thus a faster-decaying signal for n-entangled states will also cost in sensitivity.

Finally, given knowledge of $S_n(\tau)$, we can calculate η:

$$\eta_n = \frac{\sigma_S}{\alpha_n(\tau) n \gamma_e f \tau} \frac{1}{\sqrt{N}}. \tag{1.5}$$

1.5 Noise Spectroscopy

In this section we review the relevant background for Chapter 3.2, in which our goal is to characterize the noise of NV and X electronic spins due to their spin bath. More specifically, in order, we briefly review: the Ornstein-Uhlenbeck (OU) noise model of a many-body electronic spin bath, single-qubit noise spectroscopy (based on CPMG CP_m sequences), and Ramsey and Echo experiments under OU noise.

Noise Model of Electronic Spin Bath: Ornstein-Uhlenbeck (OU) Noise Process

It is often advantageous to approximate the effects of an unknown, potentially quantum, bath by a classical noise model. In fact, such simplification may be necessary for practicality, given that to understand the effect of a quantum bath on a quantum system in its entirety would require a full-fledged quantum simulator [60]. Instead, reducing the effect of the quantum bath to a physically meaningful noise model would not only aid understanding, but also the quantitative characterization of the bath by identification of physically relevant model parameters. Finally, such classical noise model is known to always exists for a qubit or qutrit under a fixed dynamics [25, 51], and naturally emerges from single-qubit noise spectroscopy (1QNS).

Here we discuss one specific noise model, the Ornstein-Uhlenbeck (OU) noise process, which has been proposed and as well experimentally confirmed to describe well a central electronic spin interacting with an electronic or nuclear spin bath in solid [60, 34, 28]. The OU noise model $b(t)$ is completely determined by two parameters (b, τ_c) that define the exponential decay of noise auto-correlation:

$$\langle b(t)b(0)\rangle \;=\; b^2 e^{-t/\tau_c}$$

where b represents the characteristic noise strength, and τ_c the correlation time or memory time of the noise process. The corresponding noise spectrum of the OU noise, per Eq. 1.7, is given by a zero-mean Lorentzian:

$$\begin{aligned} S^{OU}(\omega|b,\tau_c) &= \int \langle b(t)b(0)\rangle e^{-i\omega t} dt \\ &= \frac{b^2(2\tau_c)}{1+(\omega\tau_c)^2}. \end{aligned}$$

We can ascribe physical meaning to the parameters (b, τ_c) for the OU model describing the noise on a central qubit due to a many-body electronic spin bath. b gives

the characteristic noise or interaction strength between the qubit and its bath, and τ_c gives the (qubit-independent) 'correlation' time of the bath, or the timescale of change in the bath configuration typically via spin flip-flops.

In addition to the absolute value of each parameter, their dimensionless product $(b\tau_c)$ also characterizes the bath. More specifically, $(b\tau_c) \gg 1$ indicates a 'quasi-static' bath, or a bath whose internal dynamics is much slower relative to the interaction rate with the qubit. While this is numerically an extreme limit, over a wide range of spin concentration, in simulations and in most experimental samples so far it seems that almost every spin system has $(b\tau_c) > 1$ [120]. Indeed this may be expected, given that the spin-flip process not only is limited by the interaction strength ($\sim b$), but additionally requires that the difference of their spin resonances to be smaller than the interaction strength

Now, this model of a single OU noise source has been used to describe single NV centers interacting with a 'bulk' bath of like/homogeneous electronic spins. Then, the noise model is fully characterized by two free parameters $\hat{S}(\omega) \sim S^{OU}(\omega|b, \tau_c)$, that, in the typical quasi-static limit, can be identified from by Ramsey and Echo experiments (as will be seen below).

However, in recent studies of shallow/near-surface NV centers in diamond, it was proposed heuristically that a double OU process should better describe the true noise by an electronic spin bath [79, 94]. This model was motivated given that a shallow NV should be sensitive to both 'surface' bath spins and 'bulk' bath spins — or more generally, a homogeneous and heterogeneous groups of spins — which should have sufficiently distinct timescales of dynamics τ_c.

We will see in Chapter 3 that we explicitly verify a double OU structure for the particular NV in our system, suggestive of two effectively distinct groups of electronic spin baths. Nonetheless, given that our particular NV center has not been verified to be shallow (as typically done via detection of protons in an oil drop on the diamond surface [89]), the reason may not be strictly due to 'surface' vs. 'bulk' spins, but more simply due to the presence of a homogenous and heterogenous groups of spins, as arising from our desire to engineer a cluster of strongly coupled electronic spins

(see Section 2.1).

Single Qubit Noise Spectroscopy (1QNS)

Here we briefly introduce the established method of single-qubit noise spectroscopy (1QNS), which experimentally reveals the spectrum of noise experienced by an isolated qubit. 1QNS has been successfully applied across many physical platforms to characterize the effective noise spectrum of the native quantum bath. Given many existing excellent references on the topic [15, 89, 107], we keep to a minimal and rather intuitive introduction.

Under a specific set of assumptions (discussed below), the qubit coherence $C(T)$ at time T is given by

$$\begin{aligned} C(T) &= \langle e^{-i\phi(T)} \rangle = e^{-\langle \phi^2(T) \rangle / 2}, \\ \langle \phi^2(T) \rangle &= \int_{-\infty}^{\infty} \frac{d\omega}{2\pi} S(\omega) F(\omega). \end{aligned} \tag{1.6}$$

In other words, the qubit decoherence is completely determined by the variance of the qubit phase, $\langle \phi^2(T) \rangle$, which in turn is completely determined by two quantities: the (unknown) spectrum $S(\omega)$, which carries information about the noise $b(t)$, and the (known) so-called filter function $F(\omega)$, which is given by the particular experimental sequence applied to the qubit.

Therefore, if $S(\omega)$ is known, the qubit decoherence can be calculated.

Here we give the relevant definitions for the above quantites:

$$\begin{aligned} \phi(T) &= \int_0^T b(t) f(t), \\ F(\omega) &= \left| \int f(t) e^{-i\omega t} dt \right|^2, \\ S(\omega) &\equiv \int \langle b(t) b(0) \rangle e^{-i\omega t} dt \end{aligned} \tag{1.7}$$

The qubit phase $\phi(T)$ follows the trajectory determined by the random noise $b(t)$

and the time-domain filter $f(t) = \{\pm 1\}$. This filter $f(t)$ describes the experimental control sequence applied to the qubit, namely a series of π-pulses (spin-flips) applied to the qubit at the time of its sign switch, and also determines its frequency-domain counterpart $F(\omega)$. Finally, the noise spectrum $S(\omega)$ is defined as the Fourier transform of the noise auto-correlation.

We now review the two main assumptions that were involved to yield Eq. 1.6: namely that the qubit decoheres by dephasing, and the noise $b(t)$ is a Gaussian and classical random number. We will see that, while the dephasing assumption is strictly required (and can be verified easily experimentally), there has been increasing evidence that the Gaussianity assumption may not be as strict, given that under typical dynamical decoupling sequences the noise may be effectively made Gaussian [107].

The first assumption of 1QNS is that the qubit dominantly decoheres by dephasing. In other words, the interaction Hamiltonian H_{int} between the qubit and its bath is proportional to σ_z operating on the qubit: $H_{\text{int}} = z \otimes B$, where the operator B acts on the bath.

This constraint sets the first equality in Eq. 1.6: $C(T) = \langle e^{-i\phi(T)} \rangle$. More specifically, for simplicity, consider a classical bath, such that $H_{\text{int}} = z \otimes B$, where $B = b(t)$ is a stochastic process. Since the bath can (only) affect the qubit via σ_z, the initial qubit state $|\psi(0)\rangle = (|0\rangle + |1\rangle)/\sqrt{2}$ can only evolve by rotation about z: $|\psi(T)\rangle = (|0\rangle + e^{-i\phi(T)}|1\rangle)/\sqrt{2}$. Thus for this single-shot evolution, $C(T) \equiv \langle 0|\psi\rangle\langle\psi|1\rangle = e^{-i\phi}$. Given a randomly fluctuating $b(t)$, the final measurement yields $C(T) = \langle e^{-i\phi} \rangle$, averaged over many realizations of $b(t)$.

The motivation behind the dephasing assumption is two-fold. First, it is required to allow a simple analytical treatment. More importantly, it does not significantly limit its applicability, because many physical systems do tend to decohere by dephasing, an energy-conserving process. One intuitive justification for this observation may be that, if an energy-exchanging process (depolarizing) were to be the dominant mode of decoherence, then there must be sufficent noise concentrated close to the qubit resonance. On the other hand, dephasing is not so constrained, since the

presence of noise at any frequency will contribute to dephasing. This assumption can be verified readily in experiments, by measuring the coherence time $T_2^{(*)}$ and the energy-relaxation time T_1 of the qubit. If $T_1 \gg T_2$, the qubit is dominated by dephasing.

The second assumption made, required for the second equality to strictly hold, is that the noise strength $b(t)$ is a classical, Gaussian random number.

First of all, the motivation for assuming a classical Gaussian random process is that its cumulants higher than second order vanish [64]. Here, the first cumulant, which is its average $\langle b(t) \rangle$, can be set to zero without loss of generality. Thus the only remaining term affecting the qubit coherence is the second-order cumulant, its variance $\langle b^2(t) \rangle$.

In other words, if the Gaussian assumption is not held, to truly charcterize decoherence, one should also characterize the higher-order cumulants. In such a case, 1QNS would only be one step of characterization.

Recall that in general, a classical noise model is always possible to describe the qubit (or qutrit) decoherence under a particular dynamics [25, 51]; the problem is that this model may not be predictive or consistent with a different evolution.

It has been shown that, if the noise is instead quantum, $b(t) = e^{-iH_B t} B e^{iH_B t}$, but still Gaussian, measured decoherence will be equal to first order decay $C(T) = e^{-\chi(T)} = 1 - \chi(T) + (B^3)$, where $\chi(T) = \langle \phi^2(T) \rangle$ as defined above [107]. In other words, for sufficiently weak noise strength $b(t)$, the method of 1QNS will hold equally well for either a classical or quantum bath.

Finally, what if the noise is non-Gaussian? Then strictly the equality does not hold, and so the higher-order cumulants should be characterized. Indeed, it has been shown both theoretically and experimentally that for highly non-Gaussian noise, the higher-order spectra improve the predictability of the classical model [83, 105]. Nonetheless, the successful application of 1QNS to characterize various physical platforms seems to suggest that the assumption of Gaussianity of the noise is not very limiting in practice. While there are various arguments for why or when in general the Gaussian approximation should be good [107], there is also evidence that certain

dynamical decoupling sequences, such as CPMG, could effectively average out the higher-order cumulants, thereby reducing non-Gaussian baths into Gaussian [26].

In the next section, we describe one specific method of 1QNS, based on CPMG sequences, which will be used to measure the noise spectrum of NV and X.

Method. We are now ready to discuss the method of 1QNS to experimentally reconstruct the qubit noise spectrum $S(\omega)$. The main idea can be seen from Eq. 1.6. To identify the unknown $S(\omega)$, we apply a specific experimental sequence $F(\omega)$ to the qubit, and observe its decoherence or decay rate $\langle\phi^2(T)\rangle$.

While there is no one unique way, one simple method to reconstruct $S(\omega)$ is to create a filter that is a delta function: $F_m(\omega) = \delta(\omega-\omega_m)$. If this filter can be achieved, each experiment $F_m(\omega)$ will reveal one point of the underlying noise spectrum via the measured decay: $\langle\phi_m^2(T)\rangle = \int_{-\infty}^{\infty}\frac{d\omega}{2\pi}S(\omega)F_m(\omega) = S(\omega_m)$. This leads to a simple protocol to reconstruct the noise spectrum: apply $F_m(\omega)$ at various frequencies ω_m to map out the entire $S(\omega_m)$.

This protocol is behind the most common method for 1QNS, where an approximate delta function can be obtained from periodic dynamical decoupling (DD) sequences. The simplest DD sequence is called CPMG, which a series of periodic π-pulses applied N times with inter-pulse spacing of $2\tau_m$ on the qubit. This CP filter, in the limit of many cycles N, approaches a comb of delta functions at odd harmonics of its principal frequency $\omega_m \sim (2\pi)(4\tau_m)^{-1}$, with the delta functions at higher harmonics strongly attentuated[124, 2]:

$$F_m(\omega) \;=\; \delta(\omega_m) + \sum_{j=1}^{\infty}\frac{\delta((2j+1)\omega_m)}{(2j+1)^2}$$

This rapid attenuation, whereby the next largest correction is approximately 10 times smaller, allows the approximation of $F_m(\omega)$ as a single delta function at the principal frequency. This approximation is especially good given a noise spectrum decaying with frequency, e.g., as in the OU spectrum or the $1/f$ noise spectrum common in solid-state devices. Nonetheless, in the presence of significant higher-

frequency noise processes, further improvements should be made beyond the above approximation, e.g., by taking into account the higher-order terms in the CP filter [2] or designing filters without higher-order leakage [82].

Utilizing CP sequences, the method of 1QNS is straightforward. We first measure the decay at specific sequence CP_m:

$$\begin{aligned} \chi_m(T) \equiv \langle \phi_m^2(T) \rangle / 2 &= \int_{-\infty}^{\infty} d\omega S(\omega) F_m(\omega) \\ &\sim \frac{\pi^2}{4} S(\omega_m) T. \end{aligned} \tag{1.8}$$

Then we repeat this for a different inter-pulse spacing $2\tau_m = \pi/\omega_m$, so as to reconstruct the noise spectrum $S(\omega_m)$.

We end this section by noting the working range of the CPMG-based 1QNS: $1/T_2 \leq \omega_m \ll \Omega_0$, where Ω_0 is the pulse Rabi power.

The lower limit, i.e., the minimum noise frequency ω_{min} one could sample, is given by characteristic decay time T_2 from echo for two reasons. First, the qubit coherence and hence the signal $\to 0$ by T_2, such that any CPMG experiments with longer free evolution time $2\tau_m$ will provide no information. In addition, an indirect, more technical reason limiting $2\tau_m \leq T_2$ is given by our method of approximating $S(\omega_m)$ via the observed CPMG decay $\chi_{CP}(T)$ (recall Eq. 1.8): the (exact) proportionality constant is reached only in the limit of $N \to \infty$. This is not strictly held for CPMG with long evolution time, as full coherence decay may occur in just a few N. However, this limit could be improved by deconvolution via sinc transform.

On the other hand, the maximum noise frequency we could sample is limited by the pulse Rabi power Ω_0 with pulse length $L = (2\Omega_0)^{-1}$. As $\omega_m = (2\pi)(2(2\tau_m + L))^{-1} \to \Omega_0$, the time spent under free evolution $\tau_m \to 0$. In other words, instead of sampling the noise $b(t)$ effected by H_{int}, the qubit spends (more) time under the control Hamiltonian of strength $\Omega_0 \gg b(t)$. Thus the signal will carry less information about the true noise of interest to be characterized.

Ramsey & Echo Decays — under OU Noise

Here we discuss the two simplest experiments as measurements of decoherence: Ramsey and Echo (refer to as R and E, respectively, for convenience). We describe them under the same filter function formalism as in the previous section, and also review their specific analytical forms under an OU noise.

Ramsey under OU Noise. Ramsey, the simplest experiment, prepares the qubit in a superposition state (by a $\pi/2$-pulse) at time $T = 0$ and allows a free-evolution for time T – during which the qubit interacts with the bath – after which its coherence is measured. Hence its time-domain filter function is simply $f_R(t) = 1$ for $T \geq t \geq 0$ and zero elsewhere; equivalently, in the frequency-domain, the Ramsey filter function $F(\omega) = |\tilde{f}_R^2(\omega)|$ is a sinc centered around $\omega = 0$. In other words, a Ramsey experiment R will dominantly sample the low frequencies present in the noise spectrum $S(\omega)$.

Thus the expected decay $e^{-\chi_R(T)}$ under a Ramsey experiment for a noise spectrum $S(\omega)$ is:

$$\begin{aligned} \chi_R(T) &= 1/2 \int_{-\infty}^{\infty} \frac{d\omega}{2\pi} S(\omega) |\tilde{f}_R^2(\omega)|, \\ |\tilde{f}_R^2(\omega)| &= T^2 \ \mathrm{sinc}^2(\omega T/2) \end{aligned}$$

Defining the noise power $\sigma^2 \equiv \int_{-\infty}^{\infty} \frac{d\omega}{2\pi} S(\omega)$, one can see that if the underlying $S(\omega)$ is sufficiently concentrated at low frequencies ($S(\omega) \sim 0$ for $\omega > 1/T$), s.t. $\sigma^2 \sim \int_{-1/T}^{1/T} \frac{d\omega}{2\pi} S(\omega)$, R yields a Gaussian decay independent of the exact shape of $S(\omega)$ [107]:

$$\begin{aligned} \chi_R(T) &\sim T^2/2 \ \mathrm{sinc}^2(0) \int_{-1/T}^{1/T} \frac{d\omega}{2\pi} S(\omega) \\ &= \sigma^2 T^2/2 \\ &\equiv (T/T_2^*)^2 \end{aligned}$$

In turn, this means that, given strong noise at low frequency, Ramsey will not provide much information about the shape of the noise spectrum. However, it still

yields the noise power σ^2. In the last equality we have defined the characteristic coherence time T_2^*.

For example, if the noise is given by an OU process (a zero-mean Lorentzian),

$$S^{OU}(\omega) = b^2 \frac{2\tau_c}{1+(\omega\tau_c)^2},$$

Ramsey will yield the characteristic noise strength b:

$$\begin{aligned} \chi_R^{OU}(T) &= T^2/2 \int_{-1/T}^{1/T} \frac{d\omega}{2\pi} S^{OU}(\omega) \\ &\approx (bT)^2/2. \end{aligned}$$

The low frequency approximation in the last line requires $S^{OU}(\omega|b,\tau_c)$ to be very narrow with respect to the Ramsey filter $|\tilde{f}_R^2(\omega)|$, or equivalently that $(b\tau_c) \gg 1$. This condition is also called the quasi-static regime, where the bath configuration is relatively slow with respect to the strength of qubit-bath coupling and qubit dynamics.

More generally, without any approximation, the Ramsey under OU noise gives the following decay [30]:

$$\chi_R^{OU}(T) = b^2\tau_c^2(T/\tau_c + (e^{-T/\tau_c} - 1))$$

which, in the long-time limit $T \gg \tau_c$, reduces to an exponential decay

$$\chi_R^{OU}(T) \sim (b^2\tau_c T)$$

whereas, in the limit of quasi-static OU noise or low frequency noise $T \ll \tau_c$, as expected reduces to

$$\chi_R^{OU}(T) \sim (bT)^2/2.$$

Given that the most general decay form of R under OU noise depends on both model parameters (b,τ_c), we would expect that it should be possible to extract both

parameters from two R experiments at different times T. However, in the two limits above, the decay is proportional to T, $\chi \propto T^{\alpha}$, and we can extract only one parameter or the product (either b^2 or $b^2\tau_c$). In other words, in such limits, it is no longer possible to fully characterize the OU noise model from a single type of experiment.

We will see a similar issue in the next section with the Echo decay; however, equipped with the set of both measurements $\{R, E\}$, one can estimate the full model paramters (b, τ_c) if indeed the viable model is a single OU noise source. In addition to the past literature, we will observe this with the dark spin X.

Echo under OU Noise. After Ramsey, the next simplest experiment to measure decoherence is the spin echo (E), which prepares the qubit in a superposition (by a $\pi/2$-pulse) and allows a free-evolution for duration T except for a single π-pulse applied at time $T/2$. Its time-domain filter function is $f_E(0 \leq t < T/2) = 1$ and $f_E(T/2 \leq t < T) = -1$ and zero elsewhere. Thus, in contrast to the constant f_R, the Echo filter function $F(\omega) = |\tilde{f}_E^2(\omega)|$ is now shifted away from $\omega = 0$, with its (dominant) center frequency proportial to 1/T: $\omega_c \propto T^{-1}$.

More formally,

$$\begin{aligned} \chi_E(T) &= 1/2 \int_{-\infty}^{\infty} \frac{d\omega}{2\pi} S(\omega) |\tilde{f}_E^2(\omega)|, \\ |\tilde{f}_E^2(\omega)| &= 16 \sin^4(\omega T/4)/\omega^2 \end{aligned}$$

The echo under OU noise gives the following decay[30, 79]:

$$\chi_E^{OU}(T) = b^2\tau_c^2(T/\tau_c - 3 + 4e^{-T/(2\tau_c)} - e^{T/\tau_c})$$

which, in the long-time limit $T \gg \tau_c$, reduces to an exponential decay

$$\chi_E^{OU}(T) \sim (b^2\tau_c T)$$

whereas in the limit of quasi-static OU noise or low frequency noise $T \ll \tau_c$,

reduces to:

$$\begin{aligned} \chi_E^{OU}(T) &\sim (b^2T^3/12\tau_c) \\ &\equiv (T/T_2)^3 \end{aligned}$$

Note that the decay in the first limit is the same as that from R, indicating that for short correlation noise, the echo is unable to refocus the noise trajectories before and after the π-pulse as they are not correlated [30].

On the other hand, if we observe E with the latter decay shape (cubic in exponential), we can learn two things. First we verify the noise model is a single OU noise source in the quasistatic limit $b\tau_c \gg 1$. In addition, given prior knowledge or estimate of b from R, we can estimate τ_c from the coherence time $T_2^3 = 12\tau_c/b^2$.

As observed for Ramsey, even the decay form of E under OU noise reduces to the product of the model parameters in the limits, such that E (even if measured at different times) cannot fully characterize the model. Nonetheless, in the case of a (single) quasi-static or slow OU, the set $\{R, E\}$ is necessary and sufficient to characterize the noise model: $\hat{S}(\omega) = \hat{S}_{slow}^{OU}(\omega|b_s, \tau_s)$.

Chapter 2

Hamiltonian identification of a quantum register of electron-nuclear spin defects in diamond

Recall our goal of developing a quantum register of electronic spins in diamond. In this Chapter we take the first step towards this goal by systematically scaling up a system of interacting electronic spins, starting from a single NV center in diamond interacting with unknown electron-nuclear spin defects.

As the first main result, we develop a general method to identify the interaction Hamiltonian of unknown spins via sweeping an external static magnetic field. As the second main result, we apply this method to characterize two unknown electron-nuclear defects near the NV. More specifically, we first identify the hyperfine interaction Hamiltonian of two electron-nuclear spin defects (to denote as X spins) that characterizes each electron-nuclear spin molecule in the solid. In addition, we characterize the dipolar coupling between the NV and X electronic spins, which also reveals the relative spatial positions of the spin defects. This method to identify the Hamiltonian of unknown spin defects not only allows characterization of unknown spin defects in the solid via sweeping an external field but also enables coherent control over the larger spin system.

Before discussing the characterization of the electronic spin register, we first briefly

discuss how to physically realize such a system in diamond in the next section.

2.1 Creation of Localized Electronic Spin Clusters in Diamond

In this section, we describe and give an intuitive reasoning for the fabrication steps designed to realize a system of dark electronic spins around a central NV center in diamond. The exact fabrication and sample preparation steps are reported in [22].

Recall our target system: a central NV spin in diamond with a *coherent* register of *dark electronic spin(s)*. In other words, we want to simultaneously achieve the three italicized conditions.

First, let us start with the established knowledge of NV center formation. NVs are formed by ion implantation of the electron-donor N into diamond and subsequent annealing, but the N-to-NV conversion ratio is typically well below ten percent [80, 98, 85]. In other words, for every NV center successfully created, there can be more than ten other electronic spins in the vicinity.

However, in order to realize entangling operations before decoherence, we further require that such spins interact coherently, i.e., the coupling strength $|d|$ between spins should be larger than the inverse coherence time T_2^{-1}, $(dT_2) > 1$. However, this is difficult to optimize, given that both d and T_2^{-1} increase with the electronic spin concentration [34, 120].

Given that it is difficult to achieve $(dT_2) \gg 1$ via ion implantation alone, the approach here is to implant through a mask with nano-apertures of varying size to control the total number of implanted ions in a nanoscale volume. More specifically, we fix the implantation condition to give an average dipolar coupling strength to $d \sim 11$ kHz (from SRIM simulations) [22]. At the same time, by limiting the total number of the electronic spins, we attempt to reach $(dT_2) > 1$ at fixed d given there are fewer spins that contribute to a large, quasi-continuous spin bath background, which is the dominant cause of decoherence [34, 120]. In addition, aside from the

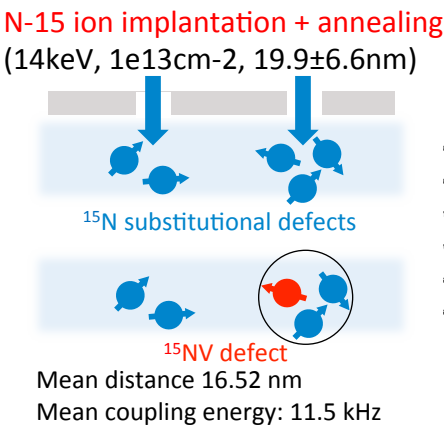

Figure 2-1: **Sample Preparation via Ion Implantation through Nano-apertures.** Given sub-ten percent conversion efficiency of implanted donor ions N (blue) into NV centers (red) in diamond, in principle up to several dark electronic spins nearby a single NV can be expected. Given implantation of electronic spins (forming the many-body e-spin bath leading to decoherence—the topic of Chapter 3.2), we aim to minimize decoherence by implanting through a nano-aperture (to limit the total number of bath spins that can randomly flip-flop) into an isotopically purified 12C diamond layer (removing the natural abundance of 13C spin bath).

decoherence due to the electronic spin bath (expected to be dominant), we also remove the next more important noise process due to the naturally abundant 13C spin bath by utilizing an isotopically purified 12C diamond layer [23].

2.1.1 Our system: NV and nearby electron-nuclear spin defects

Given such a sample, having searched over 150 implanted regions of xx nm-diameter, we identify 3 regions with single NV centers, while typically multiple NVs were found per implantation spot. Out of the 3 single NVs, one NV showed a nontrivial electronic spin spectrum as in Fig. 2-2. This is the NV we work with for the rest of the Thesis, beginning with the characterization of the two unknown electron-nuclear defects in the next Section giving rise to the observed resonances.

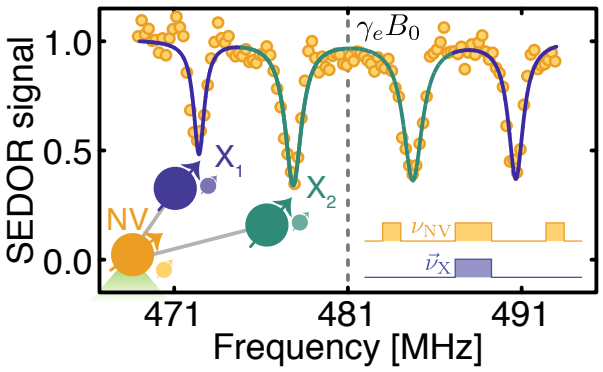

Figure 2-2: **Electronic Spin Resonance (ESR) Spectrum Seen by the NV.** We identify a single NV with a nontrivial electronic spin environment, as shown by the (non-flat) electronic spin spectrum seen from the NV. More specifically, the dips indicate presence of electronic spin defect (at that resonance) interacting with the NV. The center of the four dips is the free electron Zeeman energy at the given external static magnetic field. *Adapted from [23].*

2.2 Hamiltonian Identification of Unknown Spins

Having identified a single NV center with interacting electron-nuclear spin defects (Fig. 2-2), we now present our main results.

In Section 2.2.1, we characterize two electron-nuclear defects—henceforth called X_1 and X_2—by identifying their hyperfine tensors A_1 and A_2 respectively (their molecular fingerprint).

In Section 2.2.2, we characterize the dipolar coupling strengths d_1 and d_2 between the electronic spin of NV and that of X_1 and X_2 respectively, which also reveal and constrain the probable spatial location of the defects. As well, this coherent interaction between the electronic spins will allow the generation and detection of entangled states—which will be the topic of Chapter 3.

2.2.1 Hyperfine Interaction of X Defects

Here, we present the method to characterize the hyperfine tensor of an electron-nuclear defect via sweeping an external magnetic field. The external magnetic field (e.g., from a moveable permanent magnet above the sample) acts as the experimental handle by which the total Hamiltonian of the spin defect can be transformed non-

trivially. Then, by measuring the energies as a function of external field B, we can constrain the parameters of the hyperfine tensor, to be consistent with all available measurements.

Intuitively, this method is akin to tomographic reconstruction of 3D objects given a limited sample of 2D projections or images at various angles. In our case, the object of interest is the hyperfine tensor, and given a set of hyperfine energies measured at various field orientations, the goal is to reconstruct the tensor that yields those measurements.

The Hamiltonian of an electronic spin $S = 1/2$ interacting with a nuclear spin $I = 1/2$ is given by:

$$\begin{aligned} \mathcal{H}(\vec{B}) &= \mathcal{H}_e(\vec{B}) + \mathcal{H}_h + \mathcal{H}_n(\vec{B}), && (2.1) \\ \mathcal{H}_{e(n)} &= \gamma_{e(n)} \vec{B} \cdot \vec{S}(\vec{I}), && (2.2) \\ \mathcal{H}_h &= \vec{S} \cdot \hat{\hat{A}} \cdot \vec{I}, && (2.3) \end{aligned}$$

where the last equation describes the hyperfine interaction between the electron and nuclear spins, characterized by the hyperfine tensor $\hat{\hat{A}}$.

At sufficient magnetic field strengths $|B|$, one can satisfy the condition $\omega_n \ll \|A\| \ll \omega_e$, where $\omega_{e(n)} = \gamma_{e(n)}|B|$, due to $\gamma_e/\gamma_n > 10^3$. Given this condition, one can make the so-called secular approximation to simplify the fully general 9-term $\mathcal{H}_h$, by keeping only the terms in Hamiltonian that commutes with the dominant energy term (here the electron Zeeman energy $\mathcal{H}_e(\vec{B})$). This approximation is equivalent to assuming energy conservation during the state evolution.

More concretely, for simplicity, let us consider $\vec{B} = (0, 0, B_z)$, such that $\mathcal{H}_e(\vec{B}) = \omega_e S_z$. Then, taking the secular approximation, the hyperfine interaction simplifies to:

$$\begin{aligned} \mathcal{H}_h &= \vec{S} \cdot \hat{\hat{A}} \cdot \vec{I} && (2.4) \\ &\approx S_z \hat{A}_z \cdot \vec{I} = S_z(A_{zx} I_x + A_{zy} I_y + A_{zz} I_z), && (2.5) \end{aligned}$$

giving rise to an effective hyperfine frequency shift of $C_z = \sqrt{A_{zx}^2 + A_{zy}^2 + A_{zz}^2}$.

Here, the LHS (C_z) is the experimentally observed hyperfine splitting (modifying the free electronic spin resonance to $\omega_e + C_z/2$) as seen from Fig. 2-2. The analytical RHS now relates the experimental measurements to a function of (unknown) hyperfine parameters $A_{\alpha,\beta}$ that we wish to identify.

Then for general $\vec{B}$, we can obtain C_z via:

$$C_z = \sqrt{\mathrm{Tr}\{(H_e \otimes I_x)H_h\}^2 + \mathrm{Tr}\{(H_e \otimes I_y)H_h\}^2 + \mathrm{Tr}\{(H_e \otimes I_z)H_h\}^2}/4\omega_e. \quad (2.6)$$

Before we present the results, we first summarize the method.

Experimentally, we rotate the external field $\vec{B}$, such that the electronic spin-1/2 Zeeman Hamiltonian rotates relative to the (fixed) hyperfine tensor, $\mathcal{H}_h \neq \mathcal{H}_h(\vec{B})$. Measuring the projection of the hyperfine interaction $C_z(\vec{B})$ at several field orientations, we can fit for the parameters of interest $A_{\alpha,\beta}$ of the hyperfine tensor, where $\alpha, \beta = \{x, y, z\}$.

The number of necessary free parameters can be reduced from nine $A_{\alpha,\beta}$ to a maximum of six by the following steps. First, the hyperfine tensor is defined in its principal frame such that it is fully characterized by 3 parameters: $A = \mathrm{diag}(A_x, A_y, A_z)$. Then, in order to relate this frame to the diamond crystal frame, 3 more parameters for the Euler angles $\{\alpha, \beta, \gamma\}$ are required. Then the principal hyperfine parameters can be rotated to the crystal frame by:

$$\hat{\hat{A}} = R^T \cdot A \cdot R, \quad (2.7)$$

where R is the rotation matrix describing the transformation of the hyperfine matrix from its principal coordinate frame to the crystal frame,

$$R = \begin{pmatrix} \cos(\gamma)\cos(\beta)\cos(\alpha) - \sin(\gamma)\sin(\alpha) & \cos(\gamma)\cos(\beta)\sin(\alpha) + \sin(\gamma)\cos(\alpha) & -\cos(\gamma)\sin(\beta) \\ -\sin(\gamma)\cos(\beta)\cos(\alpha) - \cos(\gamma)\sin(\alpha) & -\sin(\gamma)\cos(\beta)\sin(\alpha) + \cos(\gamma)\cos(\alpha) & \sin(\gamma)\sin(\beta) \\ \sin(\beta)\cos(\alpha) & \sin(\beta)\sin(\alpha) & \cos(\beta) \end{pmatrix}. \quad (2.8)$$

Finally, we introduce the external static field vector

$$\underline{B}(\theta,\phi) = B_0(\sin(\theta)\cos(\phi), \sin(\theta)\sin(\phi), \cos(\theta)),$$

defined with respect to the crystal frame. Prior to the Hamiltonian characterization experiments, the external field $\underline{B}(\theta,\phi)$ at the site of the NV, introduced by a 1-inch permanent magnet above the sample, is mapped out as a function of 'magnet position' (placed on a 1D-stage following the $\langle 110 \rangle$ crystal direction). Additional details on characterization of the external static field can be found in [23].

We present the analytical results given for the interacting system of electron and nuclear spins $S, I = 1/2$.

In the case of an isotropic hyperfine tensor $A_x = A_y = A_z$, we have

$$C_z^{\text{iso}} = A_z, \tag{2.9}$$

whereas in the case of an axially symmetric tensor $A_x = A_y$, we have

$$\begin{aligned} C_z^{\text{ax}} \; &= \tfrac{1}{2\sqrt{2}} \left[5A_x^2 + 3A_z^2 - \left(A_x^2 - A_z^2\right) \times \right. \\ &\left. \left(4\cos(2\delta)\sin^2(\beta)\sin^2(\theta) + 4\cos(\delta)\sin(2\beta)\sin(2\theta) + \cos(2\beta)(3\cos(2\theta)+1) + \cos(2\theta)\right)\right]^{1/2}, \end{aligned} \tag{2.10}$$

where $\delta = \alpha - \phi$.

In the general case of an arbitrary tensor, we can also obtain an explicit expression, which is given by

$$\begin{aligned} C_z = \frac{1}{4} \Big[& 5\left(A_x^2 + A_y^2\right) + 6A_z^2 + 8\left(A_x^2 - A_y^2\right)\sin(2\gamma)\left(\cos(\beta)\sin(2\delta)\sin^2(\theta) - \sin(\beta)\sin(\delta)\sin(2\theta)\right) \\ & + \left(A_x^2 - A_y^2\right)\cos(2\gamma)\left(2(\cos(2\beta)+3)\cos(2\delta)\sin^2(\theta) - 4\sin(2\beta)\cos(\delta)\sin(2\theta) + 2\sin^2(\beta)(3\cos(2\theta)+1)\right) \\ & + \left(2A_z^2 - A_x^2 - A_y^2\right)\left(4\sin^2(\beta)\cos(2\delta)\sin^2(\theta) + 4\sin(2\beta)\cos(\delta)\sin(2\theta) + \cos(2\beta)(3\cos(2\theta)+1) + \cos(2\theta)\right)\Big]^{1/2}. \end{aligned} \tag{2.11}$$

Finally, we present the characterized hyperfine parameters of the two electron-nuclear defects nearby the NV in Fig. 2-3. From simultaneous fitting both sets of data (sweeping the field orientiations along θ or ϕ as shown inf Fig. 2-3) to the axially symmetric equation above, we obtain $A_\perp = 17.2(3)$, $A_\parallel = 29.4(2)$, $\alpha_X = 0(2)$,

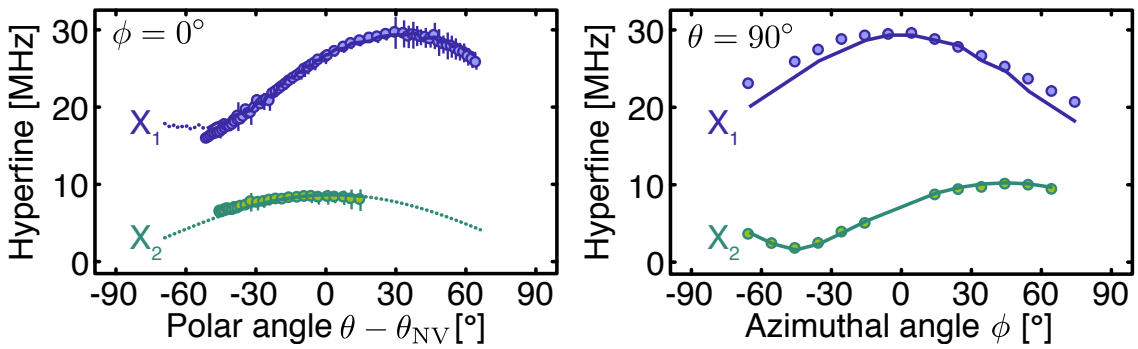

Figure 2-3: **Characterizing the hyperfine tensors of two spin defects in diamond.** (Left) Measured hyperfine strengths for various polar angles (θ) of the external applied magnetic field, plotted with respect to the polar angle of the NV center (θ_{NV}) in the azimuthal plane $\phi = 0°$. (Right) Measured hyperfine strengths for various azimuthal angles of the static magnetic field (ϕ) in the polar plane $\theta = 90°$. The solid lines are the best least-square fit of both sets of data to the eigenvalues of an axially-symmetric hyperfine tensor with four free parameters. *Adapted from [23].*

$\beta_X = 87(2)$ for X_1 and $A_\perp = 1.6(3)$, $A_\parallel = 11.2(2)$, $\alpha_X = 45(2)$, $\beta_X = 66(2)$ for X_2. We note that the axially symmetric model yielded a slightly better fit than the fully general model.

We remark that the observed hyperfine parameters were not found in the following literature [73, 56, 116, 37, 70, 3, 42], suggesting that they may never have been detected using conventional spectroscopy methods. These defects are possibly nitrogen- or silicon-related centers resulting from nitrogen-ion implantation through a 10-nm amorphous SiO_2 layer introduced to mitigate ion channeling [114]. Further triple-resonance measurements on the X nuclear spins should enable unambiguous identification of the nuclear spin species [23].

2.2.2 Dipolar Interaction between NV and X Electronic Spins

We now present the characterization of interaction between the electronic spins of the NV and the two characterized X spins, given by the dipolar Hamiltonian:

$$\mathcal{H}_{\mathrm{NV-X}} = -\frac{\mu_0}{4\pi}\frac{\gamma_{\mathrm{NV}}\gamma_{\mathrm{X}}\hbar^2}{r^3}(3(\underline{S}_{\mathrm{NV}}\cdot\underline{r})(\underline{S}_{\mathrm{X}}\cdot\underline{r}) - (\underline{S}_{\mathrm{NV}}\cdot\underline{S}_{\mathrm{X}})), \tag{2.12}$$

where $\underline{r} = (\sin(\zeta)\cos(\xi), \sin(\zeta)\sin(\xi), \cos(\zeta))$ is the interatomic vector of norm 1 that join the NV center and X spin defect, parameterized by the distance r between the two centers and the polar and azimuthal angles (ζ, ξ) defined with respect to the NV molecular axis.

First, let us note that the NV is a spin-1 system $S_{NV} = 1$, in contrast to $S_X = 1/2$, and thus has a zero-field splitting $\Delta = 2\pi \cdot 2870$ MHz quantized along its $\langle 111 \rangle$ molecular axis. Therefore, at sufficiently weak static magnetic field strength $\gamma_e B_0 \ll \Delta$, the NV electronic spin quantization axis is only slightly tilted away from its molecular axis while the X electronic spin is predominantly quantized along the external field. This behavior leads to a non-trivial transformation of the dipolar interaction tensor under rotation of the field.

Given $\omega_{NV} > \omega_X \gg ||\mathcal{H}_{\mathrm{NV-X}}||$, the dipolar Hamiltonian acts as a weak perturbation to both the internal Hamiltonian of NV and X, $\mathcal{H}_{\mathrm{NV}}, \mathcal{H}_{\mathrm{X}}$. Then, via the secular approximation, the remaining terms of $\mathcal{H}_{\mathrm{NV-X}}$ must commute with *both* $\mathcal{H}_{\mathrm{NV}}$ and $\mathcal{H}_{\mathrm{X}}$. In other words, given a general $\vec{B}$ orientation (which the NV spin follows only slightly whilst X almost completely), we first diagonalize the interal Hamiltonian $\mathcal{H}_{\mathrm{NV(X)}}$ by a unitary rotation $U_{\mathrm{NV(X)}}$, such that the commutator $[U_{\mathrm{NV(X)}}\mathcal{H}_{\mathrm{NV(X)}}U^{-1}_{\mathrm{NV(X)}},\ S^z_{\mathrm{NV(X)}}] = 0$.

Then we accordingly rotate the dipolar Hamiltonian

$$\tilde{\mathcal{H}} = U_{\mathrm{X}}^{-1}U_{\mathrm{NV}}^{-1}\mathcal{H}_{\mathrm{NV-X}}U_{\mathrm{NV}}U_{\mathrm{X}}, \tag{2.13}$$

and via secular approximation keep the only commuting (energy-conserving) term $\propto S^z_{\mathrm{NV}}S^z_{\mathrm{X}}$.

By projecting the NV electron spin $S = 1$ onto an effective two-level system (by keeping only the $m_s = \{0, -1\}$ manifold and eliminating the never-populated state $m_s = 1$), we can analytically evaluate the secular dipolar strength. In this

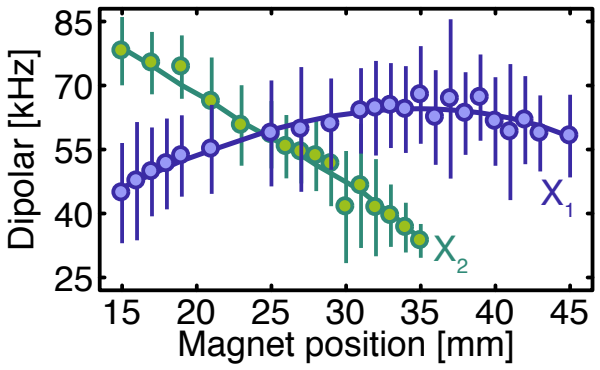

Figure 2-4: **Characterizing the dipolar doupling between electronic spins in diamond.** Measured dipolar coupling strengths between the NV electron spin and the X_1 (blue) and X_2 (green) electron spins for various magnet positions. The solid line is the best least-square fit to the eigenvalues of the interacting spin Hamiltonian with three free parameters $(r, \zeta, \xi$, see Eq. 2.14), which parametrize the relative position of the two X spins with respect to the NV center. *Adapted from [23].*

approximation, valid when the $m_s = +1$ level is energetically isolated, we obtain:

$$\begin{aligned} d &= \frac{d_c}{r^3}\frac{A+B+C}{D}, \qquad (2.14)\\ A &= 3\sin(2\zeta)\cos(\xi)\sin(\theta')[\Delta - 3\gamma_e B_0\cos(\theta')],\\ B &= -6\gamma_e B_0\sin^2(\zeta)\cos(2\xi)\sin^2(\theta'),\\ C &= (3\cos(2\zeta)+1)(\Delta\cos(\theta') - \gamma_e B_0\cos(2\theta')),\\ D &= 4\sqrt{2(\gamma_e B_0\sin(\theta'))^2 + (\Delta - \gamma_e B_0\cos(\theta'))^2}, \end{aligned}$$

where $d_c = 2\pi \cdot 52.041$ MHz is the dipolar constant for two electronic spins at a distance of 1 nm and $\theta' = \theta - \theta_{\mathrm{NV}}$ is the angle between the static magnetic field and the NV molecular axis in the $\mathbf{y}_{\mathrm{NV}} = 0$ plane.

Similarly to previous case, the effective dipolar strength d is the experimentally observed value, while the RHS of Eq. 2.14 relates the measured d to the parameters (r, ζ, ξ) describing the relative position of the X electronic spin with respect to a central NV.

Finally, we present the experimental results in Fig. 2-4. Given the set of measured dipolar strengths at various field orientations, we compare it to the expected (calculated) dipolar strengths. By calculating the least-square error, we can produce a

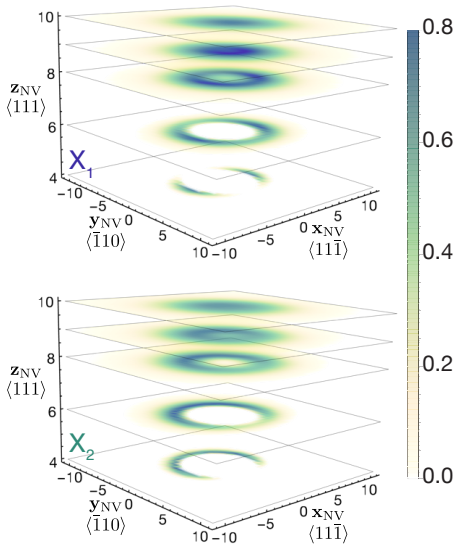

Figure 2-5: **Locating two spin defects in diamond.** Probability distribution maps of the location of the X_1 (top) and X_2 (bottom) spins defined with respect to the coordinate frame of the NV center placed at the origin. The darker color indicates a higher probability of finding the X spin at this specific location. *Adapted from [23].*

relative probability distribution map of spatial location of $X_{1,2}$ with respect to a central NV as shown in Fig. 2-5. At the most probable location, we find $r_1 = 9.23(3)$ nm and $r_2 = 6.58(3)$ nm for X_1 and X_2 respectively.

Conclusion Having developed a general method to identify the interaction Hamiltonian of unknown electron-nuclear defects via the sweep of an external field, we characterized a system of two electron-nuclear spin defects around the NV, forming a quantum register of electronic spins. Given this controllable system of NV and X electronic spins, we characterize the performance of this quantum device in the next Chapter.

Chapter 3

Characterize performance of a quantum register: Entanglement detection and noise spectroscopy

In the previous Chapter, we characterized a system of electronic-nuclear spin defects around the central qubit (NV), thus identifying a controllable register of dark electronic spins around the NV. In this Chapter, we characterize the performance of this quantum device with respect to two aspects: the entanglement generated (in Chapter 3.1) and the noise experienced (in Chapter 3.2) by this device.

In Chapter 3.1, we develop a novel metric, called the subspace witness, to improve upon the conventional entanglement witness based on state fidelity. Given that entanglement is critical for many quantum information tasks, an accurate characterization of entanglement generated by a device is desired, not only to verify its non-classical nature but also to validate its use for the quantum information task of interest. As the main result, the subspace witness, at the cost of additional measurements, is more robust against local unitary control errors – more specifically, it is insensitive to any combination of single-qubit phase errors accrued during the quantum circuit preparing and measuring the target entangled state. Indeed, for two-qubit entanglement, we theoretically demonstrate – and verify experimentally with NV and X electronic spins – the advantage of the subspace witness. For genuine multipartite entanglement, we

first show that, depending on the target entangled state, the subspace witness can still be very efficient in the number of measurements required; furthermore, the subspace witness, beyond entanglement detection, also facilitates lower bound estimation of entanglement via the metric called GME concurrence.

In Chapter 3.2, as the first step to characterize the noise affecting a multi-qubit register, we demonstrate a protocol to build a self-consistent classical noise model for individual qubits. Given that the lifetime of quantum devices is limited by decoherence, a practical (classical) and predictive model of the noise is desired not only to better characterize the unknown, potentially quantum, bath but also to develop more robust quantum devices. By performing noise spectroscopy of both NV and X electronic spins, we find two results. First, for the NV qubit which is well isolated (distinguished) from the bath, it is possible to build a noise model that is self-consistent or predictive over a varied set of dynamics – indicating an accurate characterization of the bath. However, for the nearby X qubit, it is not possible – rather, we find evidence for a more complex and quantum bath for the X qubit that precludes a self-consistent classical noise model. As we note at the end, this bath of X, which may contain a group of coherently interacting electronic spins, may be of interest for future investigation, in order to further scale up the electronic spin register.

We start by discussing our work on more robust entanglement detection in the presence of local unitary errors.

3.1 Improved Entanglement Detection under Local Unitary Errors

In this section, we exploit universal control of our system of electronic spins to generate and verify $n = 2$ entanglement between NV and X spins. More generally, we develop a novel method, called entanglement subspace witness, to detect entanglement more accurately and robustly in the presence of local unitary (i.e., single-qubit) errors, improving upon the existing conventional method based on state fidelity.

Background: Entanglement Witness Entanglement, while critical for many quantum applications, is difficult to characterize both theoretically and even more so experimentally. The most direct way is via quantum state tomography (QST), whose goal is to identify the density operator ρ describing the (true) state; then, given knowledge of ρ, use one of several proposed metrics of quantifying entanglement in ρ. Unfortunately, QST has a measurement cost scaling exponentially with the qubit number n, such that QST quickly becomes intractable for moderate n. Even for small n systems, errors in state preparation and measurement (SPAM) compound the difficulty in identifying ρ with high accuracy [103, 76, 11, 4].

Instead of *quantifying* entanglement, when the goal is more simply to *detect* whether entanglement is present or not, an attractive alternative is to utilize the so-called entanglement witnesses W [88, 53]. The witness operator W is designed to 'witness' or detect a specific entangled state $|\psi\rangle$: its expectation value $\langle W_\psi \rangle = \mathrm{tr}(\rho W_\psi)$ is designed to be negative for specific entangled states, while positive for all separable states. And given that one measures an operator W, instead of the state ρ, the number of measurements for a witness scales much more favorably with respect to n in contrast to QST.

While designing a witness for an arbitrary entangled state is nontrivial [45, 46, 55, 40], for NPT entangled states $|\psi\rangle$ (states that have negative eigenvalues under positive partial transpose) [9], such as the well-known Bell, GHZ, W, and Dicke states, the witness is based on the state fidelity measurement $\langle F_\psi \rangle \equiv \langle \psi|\rho|\psi\rangle$, or more specifically:

$$W_\psi = \alpha - |\psi\rangle\langle\psi|. \tag{3.1}$$

Here α is the squared maximum overlap of $|\psi\rangle$ with all possible separable states [13] so as to conservatively detect entanglement.

Limitations of the 'state' entanglement witness W_ψ One problem with this entanglement witness (that we call 'state' witness W_ψ) is that it can severely under-

estimate the amount of entanglement present in ρ in the presence of local unitary (i.e., single-qubit) errors. Recall that local unitaries do not change the amount of entanglement—but still can rotate the true ρ away from ideal target $|\psi\rangle\langle\psi|$. Therefore, in general, the presence of local unitary errors leads to a smaller overlap $\langle F_\psi\rangle$ and hence under-estimation of entanglement.

For concreteness, let us demonstrate this explicitly for the simplest entangled state between $n = 2$ qubits. For a two-qubit system, there are four canonical maximally entangled states, the Bell states [7, 19, 8]. The Bell states $\{|\Phi^\pm\rangle, |\Psi^\pm\rangle\}$ form an orthogonal basis, thus any state (and in particular entangled states) can be written in terms of their superpositions. Choosing the computational basis to describe the energy eigenbasis, we can explicitly write a Bell state as $|\Phi^\pm(\Psi^\pm)\rangle = (|k\rangle \pm |\bar{k}\rangle)/\sqrt{2}$, with $|k\rangle = |00\rangle(|01\rangle)$ and $|\bar{k}\rangle$ the corresponding spin-flipped states. Each pair of Bell states, $|\Phi^\pm\rangle$ and $|\Psi^\pm\rangle$, span a subspace with constant energy. For many applications, such as entanglement-enhanced quantum sensing [12, 77, 21] or decoherence-protected subspaces [87, 69, 66, 38, 17, 18], states inside this subspace are equally beneficial. In particular, we can identify the family of maximally entangled states inside such subspaces, parametrized by a phase ϕ,

$$|\Phi(\phi)\rangle = \cos(\phi/2)|\Phi^+\rangle + i\sin(\phi/2)|\Phi^-\rangle, \tag{3.2}$$

and similarly for $|\Psi^\pm\rangle$. Here ϕ describes the phase degree of freedom that leaves unchanged the state desired properties (e.g., for enhanced sensing or decoherence-protected memory respectively).

Fixing ϕ, we can build a canonical 'state' witness as in Eq. 3.1 (with $\alpha = 1/2$). This is a good witness to detect the presence of two-qubit entanglement in any state ρ, given that all two-qubit entangled states are NPT. The expectation value of the witness depends on the state fidelity, $W_\psi = 1/2 - F_\psi$, where the state fidelity is a function of ϕ:

$$\langle F_\psi\rangle = \langle\psi(\phi)|\rho|\psi(\phi)\rangle = P + C(\phi) \leq P + |\rho_{k\bar{k}}|. \tag{3.3}$$

Using the notation $\rho_{jk} = \langle j|\rho|k\rangle$, here $P = 1/2(\rho_{kk} + \rho_{\bar{k}\bar{k}})$ is the sum of populations in the $|k\rangle, |\bar{k}\rangle$ subspace and

$$\begin{aligned} C(\phi) &= \mathrm{Re}(\rho_{k\bar{k}})\cos(\phi) + \mathrm{Im}(\rho_{k\bar{k}})\sin(\phi) \\ &= |\rho_{k\bar{k}}|\cos(\phi + \theta_{k\bar{k}}) \end{aligned} \tag{3.4}$$

are the relevant coherences, with $\tan(\theta_{k\bar{k}}) = \mathrm{Im}(\rho_{k\bar{k}})/\mathrm{Re}(\rho_{k\bar{k}})$.

Recalling that the family of entangled states $|\Phi(\phi)\rangle$ (whose state fidelity is being measured) is *maximally* entanlged, ideally the witness should (i) successfully detect the entanglement, and (ii) detect it at the maximum possible violation, i.e., minimum $\langle W_\psi\rangle = 1/2 - \langle F_\psi\rangle = -1/2$.

However, we see instead the coherence $C(\phi)$ is maximum only for $\theta_{k\bar{k}} = -\phi$. Unfortunately, $\theta_{k\bar{k}}$ might be unknown due to the unitary component of SPAM errors. Then, while $P < 1/2$ always reflects a suboptimal (or absent) entanglement, $C(\phi)$ might even be negative, leading to the false conclusion that the state is not entangled—although the state is maximally entangled.

Main Results In order to improve upon the state witness W_ψ, we develop a novel witness measurement called 'subspace' witness $\langle W_s\rangle$, which at the cost of additional measurements, becomes robust against a specific type of local unitaries, namely (any combination of) single-qubit phase errors ϕ:

$$\langle W_s\rangle = \min_\phi \langle W_\psi\rangle = \alpha - \max_\phi \langle\psi(\phi)|\rho|\psi(\phi)\rangle. \tag{3.5}$$

We call this a 'subspace' witness because it successfully detects any entangled state $|\psi(\phi)\rangle$ inside the subspace spanned by the relevant entangled-state basis (e.g., the space spanned by either $|\Phi^\pm\rangle$ or $|\Psi^\pm\rangle$ as was seen above). In other words, with respect to the state witness which is designed for a specific ϕ, the subspace witness detects a larger family of entangled states $|\psi(\phi)\rangle$ for all ϕ—and always at maximum possible violation (i.e., most negative) $\langle W_s\rangle = \min_\phi\langle W_\psi\rangle$. Note this is equivalent to the statement that the subspace witness can successfully detect the entangled state

in the presence of unknown local phase errors ϕ over the n qubits—and always at the maximum possible violation.

With respect to the existing characterizations of entanglement, namely the entanglement witness (for detection) and an entanglement measure (for quantification), we see qualitatively that the subspace witness is an intermediate metric between them. More specifically, while the entanglement measure is optimized over all possible local unitaries and the witness over none, the subspace witness is optimized over local unitaries (only) along the z-direction (to be invariant under relative phase). In fact, we find a more quantitative link between the three methods, as that the subspace witness (beyond detection) also facilitates lower-bound quantification of entanglement via generalized concurrences.

In the following section, we first discuss the case of $n = 2$-qubit entanglement, for which the subspace witness can be directly shown to outperform the conventional state witness both theoretically (since for $n = 2$ an analytical quantification of entanglement is known) and experimentally (with our two-qubit system of NV and X). Then in the last section, we discuss the extension to $n > 2$, i.e., genuine multipartite entanglement (GME).

3.1.1 Two-qubit Entanglement

In this section, we demonstrate the advantage of the proposed subspace witness $\langle W_s \rangle$ over the conventional state witness $\langle W_\psi \rangle$ in three parts. The first two parts will be the theoretical and experimental comparisons of the two methods of entanglement detection. Afterwards, we will discuss their relation to (lower bound) quantification of entanglement.

Theory: Example for Bell States Here we give an example for the two qubit case, given that an analytical expression of the entanglement measure called concurrence C_2 (not to be confused with coherence C below) can be obtained. In this section we will explicitly see the subspace entanglement witness $\langle W_s \rangle$ detects a larger share of entangled states than does a typical state witness $\langle W_\psi \rangle$, and does so with a strictly

larger violation.

Consider a generic state in the subspace spanned by one pair of Bell states (e.g., $|\Phi^{\pm}\rangle$), which can be written as

$$\rho_\Phi = \frac{\mathbb{I}_\Phi}{2} + \frac{\epsilon}{2}(\sin\phi_0\cos\theta\,\Phi_x + \sin\phi_0\sin\theta\,\Phi_y + \cos\phi_0\,\Phi_z),$$

where Φ_α are Pauli matrices in the (sub)space, e.g., $\Phi_x = |\Phi^+\rangle\langle\Phi^-| + |\Phi^-\rangle\langle\Phi^+|$ and $\mathbb{I}_\Phi$ is the identity in the subspace. $\rho_\Phi(\epsilon,\theta,\phi_0)$ is uniquely defined in the following range: $\epsilon \geq 0$, $\theta \in [0, 2\pi)$, and $\phi_0 \in [0,\pi]$, where $\epsilon = 0$ indicates a classical mixture.

In order to gain insight into this generic state, first let us inspect the double-quantum coherence C (necessarily nonzero for entanglement):

$$C = \langle 00|\rho_\Phi(\epsilon,\theta,\phi_0)|11\rangle = (\epsilon/2)(\cos\phi_0 + i\sin\phi_0\sin\theta). \tag{3.6}$$

This shows that maximum entanglement of ρ_Φ—i.e., when $|C| = \epsilon/2$—occurs either when $\sin^2\phi_0 = 0$ or $\sin^2\theta = 1$. The former indicates a state with fully real coherence $C = \epsilon/2$, and the latter case refers to a more general complex coherence $C = e^{i\phi_0}\epsilon/2$.

Now, to determine when ρ_Φ is entangled, we can calculate the concurrence C_2 for this generic state. In fact, C_2 reveals that in general $\rho_\Phi(\epsilon>0,\theta,\phi_0)$ is entangled (except at the special point at $\theta = 0, \phi_0 = \pi/2$). More explicitly:

$$\begin{aligned} C_2 &= \sqrt{a + b|\epsilon|} - \sqrt{a - b|\epsilon|}, \\ a &= (1 - \epsilon^2\sin^2\phi_0(1+\cos 2\theta))/4; \\ b &= \sqrt{b_1 b_2}/2, \\ b_1 &= 2 - \sin^2\phi_0(1+\cos 2\theta) \geq 0, \\ b_2 &= 2 - \sin^2\phi_0(1+\cos 2\theta)\epsilon^2 \geq 0. \end{aligned} \tag{3.7}$$

Recall that $C_2 > 0$ indicates entanglement. Given that $C_2 > 0 \Rightarrow 2b|\epsilon| > 0$, due to positivity of b, in general $\rho_\Phi(\epsilon>0,\theta,\phi_0)$ is entangled.

Returning to our goal of comparing the witnesses, this means that an ideal entanglement witness, when applied to $\rho_\Phi(\epsilon>0,\theta,\phi_0)$, should *always* detect entanglement

(except at the special point). Let us now compare the performance of the two witnesses of interest.

Let us first examine the state witness $\langle W_\psi \rangle$—and identify the 'range' of states it can detect as well as its magnitude of violation. Here the target state is either $|\psi\rangle = |\Phi^\pm\rangle$; we choose $|\Phi^+\rangle$ as it makes no difference in the detectable range or the degree of violation. More specifically, we see that

$$\begin{aligned}\langle W_\psi \rangle =& \frac{1}{2} - \langle \Phi^+ | \rho_\Phi | \Phi^+ \rangle \\ =& -\frac{\epsilon}{2} \cos\phi_0 \\ =& -\mathrm{Re}(\langle 00 | \rho_\Phi(\epsilon, \theta, \phi_0) | 11 \rangle) = -\mathrm{Re}(C).\end{aligned} \tag{3.8}$$

In other words, the range of detectable states for $\langle W_\psi \rangle$ is limited to $\phi_0 \in [0, \pi/2)$—even though all of $\phi_0 \in [0, \pi]$ are entangled. Furthermore, $\langle W_\psi \rangle$, being oblivious to θ, either underestimates or completely misses all the entanglement in the imaginary part of the coherence.

Finally, we show that the subspace witness $\langle W_s \rangle$ captures a larger share of entangled states, i.e., all the entangled states in the subspace, and also with a larger violation. The subspace witness yields

$$\begin{aligned}\langle W_s \rangle =& \frac{1}{2} - \max_\phi \langle \Phi(\phi) | \rho_\Phi | \Phi(\phi) \rangle \\ =& -\frac{\epsilon}{2} \max_\phi \{\sin\theta \sin\phi_0 \sin\phi + \cos\phi_0 \cos\phi\} \\ =& -\frac{\epsilon}{2} (\sin^2\theta \sin^2\phi_0 + \cos^2\phi_0)^{1/2} \max_\phi \{\cos(\phi - \theta')\} \\ =& -|\langle 00 | \rho_\Phi(\epsilon, \theta, \phi_0) | 11 \rangle| \max_\phi \{\cos(\phi - \theta')\} \\ =& -|\langle 00 | \rho_\Phi(\epsilon, \theta, \phi_0) | 11 \rangle| = -|C|.\end{aligned} \tag{3.9}$$

In other words, the subspace witness detects—with maximum violation $|C|$—all of $\rho_\Phi(\epsilon > 0, \theta, \phi_0)$ except at the special (unentangled) point mentioned above.

Experiment: Generating and Detecting NV-X Entanglement Here we present the experimental results of the detection via the two witnesses of interest of entan-

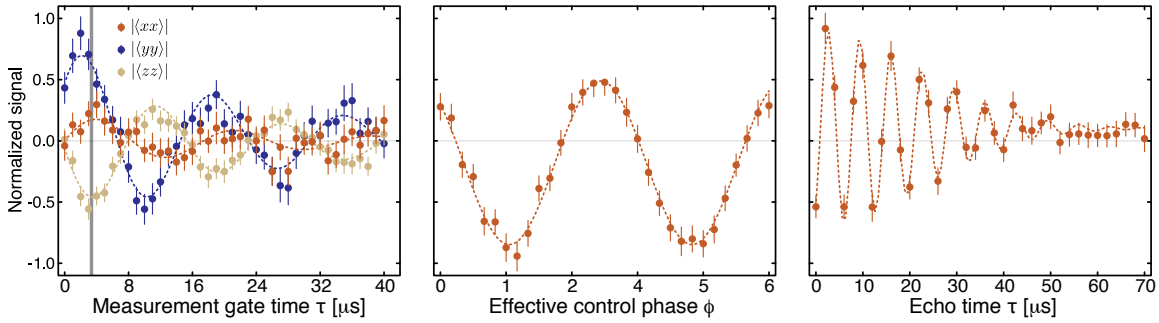

Figure 3-1: **Demonstration of witness measurements $\langle W_\psi \rangle$ and $\langle W_s \rangle$ for $d = 2$ target entangled state** (Left) We measure the 'state' entanglement witness measurement, based on Bell state fidelity, which successfully detects entanglement by $\langle W_\psi \rangle = \alpha - \langle \Phi^+ | \rho | \Phi^+ \rangle = -0.07421(4)$. Grey vertical line denotes the optimal measurement gate time that would yield the desired two-body correlators $\langle \sigma_1^j \sigma_2^j \rangle$ in the absence of decoherence. To account for decoherence, the signal is fit (dotted lines) to exponentially decaying oscillation with characteristic decay time $T = 25\mu s$. Given the short optimal gate time, we see little difference when accounting or not for the decay. The measured two-body correlations are $|\langle \sigma_1^x \sigma_2^x \rangle| = 0.2142(1)$, $|\langle \sigma_1^y \sigma_2^y \rangle| = 0.5857(2)$, and $|\langle \sigma_1^z \sigma_2^z \rangle| = 0.4970(0)$. (Center) Sweeping the control phase ϕ reveals oscillations between the real and imaginary part of the coherence ρ_{14}. By fitting the oscillations (dotted line) we extract the coherence amplitude and calculate the entangled state fidelity maximized over the Bell subspace, thereby improving entanglement detection by $\langle W_s \rangle = \alpha - \langle \Phi | \rho | \Phi \rangle = -0.1827(4)$. (Right) Measuring the spin echo after preparing the entangled state also yields the subspace witness, as the coherence ρ_{14} time evolution is equivalent to sweeping a phase $\phi \equiv \nu\tau$; this detection method further estimates the time-scale of (detectable) entanglement. The two electronic spin system in diamond, after entangled state preparation to ρ, decohere under the spin echo pulse sequence, yielding a characteristic decay time $T_2 = 31(3)\mu s$ when fitted to a Gaussian decay (dotted line). As the population $P = 0.371$ is constant over the timescale of experiment, as measured independently, we witness entanglement until $\tau^* \leq T_2 \ln(C(0)/(\alpha - P))^{1/p} = 33(3)\mu s$. *Adapted from [104].*

glement generated between the electronic spins NV and X. Experimental details of entanglement generation we leave in the paper [104].

We now discuss the measurement results of the (true) generated state ρ, with the attempt to create the (target) Bell state $|\Phi^+\rangle$.

First, we measure the state witness $\langle W_\Phi(\phi = 0) \rangle$ which requires the measurement of the Bell state fidelity $M = |\Phi^+\rangle\langle\Phi^+|$, to yield the signal $S = \mathrm{tr}(\rho M) = \langle \Phi^+ | \rho | \Phi^+ \rangle$. Or equivalently, given $\langle \Phi^+ | \rho | \Phi^+ \rangle = \frac{1}{4}(1 + \langle \sigma_1^z \sigma_2^z \rangle + \langle \sigma_1^x \sigma_2^x \rangle - \langle \sigma_1^y \sigma_2^y \rangle)$, one can measure the three correlators, $\langle \sigma_1^\alpha \sigma_2^\alpha \rangle$ with $\alpha = \{x, y, z\}$. From the 3 measurements shown in

Fig. 3-1, we obtain $F_{\Phi^+} = 1/4(1+0.497+0.2142+0.5857) = 0.57421(4) > 1/2$. From this fidelity we have $\langle W_\Phi \rangle = -0.07$ which successfully detects entanglement.

Still, this measurement might underestimate the amount of entanglement in the presence of coherent local errors. We thus measure the subspace witness $\langle W_s \rangle$, to extract the coherence $|\rho_{k\bar{k}}| = |\langle 00|\rho|11\rangle|$. More specifically, in contrast to the (fixed) Bell state fidelity operator $M = |\Phi^+\rangle\langle\Phi^+|$, we can modulate the measurement operator to $M(\phi) = |\Phi(\phi)\rangle\langle\Phi(\phi)| = R_z(\phi)|\Phi^+\rangle\langle\Phi^+|R_z^\dagger(\phi)$, where $R_z^\dagger(\phi)$ is single-qubit phase modulation about z on one of the two qubits. Then one can find a resulting signal up to a constant (see Fig. 3-1:

$$\begin{aligned} S(\phi) &= \mathrm{tr}(\rho M(\phi)) \\ &= \frac{\langle \sigma_1^x \sigma_2^x - \sigma_1^y \sigma_2^y \rangle}{2} \cos(\phi) - \frac{\langle \sigma_1^x \sigma_2^y + \sigma_1^x \sigma_2^y \rangle}{2} \sin(\phi) \\ &= 2\mathrm{Re}(\rho_{14}) \cos(\phi) - 2\mathrm{Im}(\rho_{14}) \sin(\phi) \\ &= 2C(\phi), \end{aligned} \tag{3.10}$$

where $\rho_{14} = \langle 00|\rho|11\rangle$ is the coherence of interest, and the (undersired) constant is the part invariant under R_z: $P = (1 + \langle \sigma_1^z \sigma_2^z \rangle)/4$. (Note that while the exact $M(\phi)$ used in our experiment is not the same as $R_z(\phi)|\Phi^+\rangle\langle\Phi^+|R_z^\dagger(\phi)$ [104]—the signal is only different in the (undesired) constant, and hence signal amplitude in Fig. 3-1 still yields the coherence of interest) We thus obtain a maximum fidelity of $\langle \Phi|\rho|\Phi\rangle = 0.6827(4)$, corresponding to $\langle W_s \rangle = -0.1827(4)$, having optimized over the $|\Phi\rangle$ subspace. This indicates that we have indeed coherent errors affecting our state preparation and measurement process.

As an aside, we note that the subspace witness can also help determine the entanglement coherence time. The (entangled) prepared state $\rho(\tau = 0)$ will evolve under the environment influence and the natural (or engineered) Hamiltonian. By measuring the subspace witness after a time τ, one can then detect whether entanglement is still present, at the net of local, unitary evolution. By setting $\max_\phi[F_\psi(\tau^*)] = \alpha$ we can further define a threshold time τ^* after which entanglement in $\rho(\tau \geq \tau^*)$ is no longer witnessed.

In estimating such entanglement coherence time, to simplify the measurement of the subspace witness, we can apply the phase ϕ rotation at each time point measured, such that $\phi = \nu\tau$. Then, from the decay of the oscillations in C one can directly extract W_s at $\tau = 0$ and the characteristic time τ^*. We note that in general both coherences C and population P will decay for open quantum systems, but only extracting the coherences at various ϕ is needed to reconstruct W_s. In our experiments (see Fig. 3-1), we thus measure the phase-modulated decay of the coherence. As the main decoherence source is dephasing, which leaves populations intact, we simply verify that $P(\tau)$ is constant. In experiments, we compare $P(\tau) = (1 + \langle\sigma_1^z\sigma_2^z(\tau)\rangle)/4$ at $\tau = 0\,\mu$s and $\tau = 40\mu$s and, as expected, observe no decay in $\langle\sigma_1^z\sigma_2^z(\tau)\rangle$. We then study the entanglement decay under a spin echo [47, 21] of varying duration τ. The prepared entangled state ρ evolves under $\mathcal{H}_{\text{int}}$ (which would not affect the ideal state $|\Phi\rangle$) and decoherence. We then apply the measurement modulated at $\phi = \nu\tau$ with $\nu = 15$ kHz. A simple Gaussian decay fit yields a characteristic decoherence time $T_2 = 31(3)\mu s$ of the double-quantum coherence $|\langle 00|\rho|11\rangle|$, such that taking a constant $P = 0.374(1)$, we obtain the time $\tau^* = 33(3)\mu s$ until which entanglement can be detected.

Finally, while we have shown that we can create entanglement in our system, the state fidelity is far from optimal. To improve the quality of entanglement in our hybrid system and investigate the source of non-ideality, we probe the entanglement as a function of repetitive state initialization steps. In this way, we can distinguish between initialization I and control errors in U (Fig. 3-2).

We repeat the HHCP plus laser polarization block $N = \{1, 3, 5\}$ times (as described in [22, 104]) to create $\rho_0(N)$, then prepare the entangled state $\rho(N)$ and measure the witness $\langle W_s(N)\rangle$ with fixed control operations. The result is shown in Fig. 3-2. With increasing N we observe an increase in the overall fidelity $F_s(N)$, due to an increase in both the population difference (inferred from $P(N)$) as well as the double-quantum coherence $C(N)$. We note that explicitly verifying an increase in coherence is of practical importance, because specific applications, e.g., classical field sensing with GHZ states — the topic of the Chapter 4 — depend strictly on the

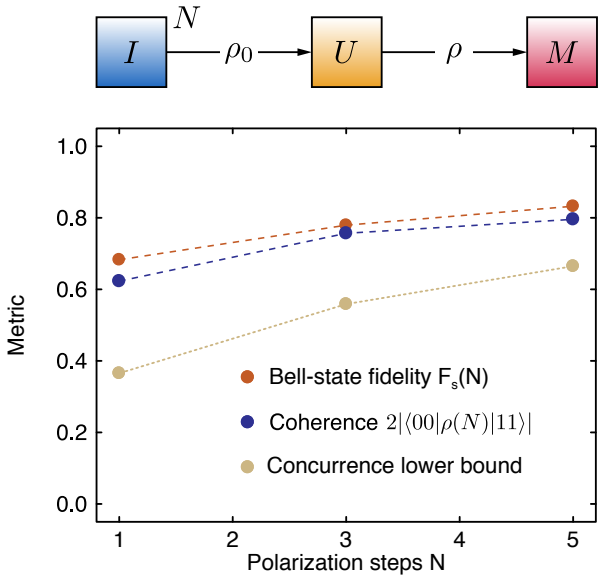

Figure 3-2: **Improved entanglement detection allows improved bound to entanglement**: Given imperfect state initialization step that prepares ρ_0 with sub-unit purity, it is possible to improve purity by N repetitive initialization steps. We plot as a function of N the following results of the subspace witness: namely, the Bell state fidelity $F_s(N) = P(N) + |\langle 00|\rho(N)|11\rangle|$, the coherence $2|\langle 00|\rho(N)|11\rangle| = 2\max_\phi[C(\phi)] \leq F_s(N)$, and the resulting lower bound to concurrence. With $N > 1$ we observe the expected improvement in purity, from $P(N) = (1+\langle\sigma_1^z\sigma_2^z(N)\rangle)/4$, that leads to improved $F_s(N)$. We also verify the increase in double-quantum coherence generated $|\langle 00|\rho(N)|11\rangle|$, which is of practical importance given that specific applications such as entanglement-enhanced sensing with GHZ states benefit directly from larger quantum coherence and not directly the fidelity itself. In addition, we note that the subspace witness $\langle W_s\rangle$ improves bound to entanglement (via concurrence) over the typical 'state' witness $\langle W_\psi\rangle$ due to improved Bell state fidelity. The errorbars are smaller than the dots for all plots. The applicability of improved bound for specific GME states by $\langle W_s\rangle$ is discussed in the text. *Adapted from [104].*

amount of coherence (not necessarily fidelity) of the entangled state.

Lower-bound to Entanglement Finally, we conclude the Section remarking on the connection to entanglement quantification. As may be expected, the subspace witness, which yields a larger violation, gives a tighter bound on the amount of entanglement generated (Fig. 3-2). While such a (quantitative) relation might seem intuitive (and expected), a 'general' way to relate entanglement detection to entanglement quantifiers is not known. However, for the two-qubit case, it has been shown [8] that one can relate Bell fidelities F_ψ to the entanglement of formation, and thereby

to any other related metrics such as the well-known concurrence. More specifically, the lower-bound to the two-qubit concurrence is $C_2(\rho) \geq \max(0, -2W_\psi)$, with $C_2 = 1$ for maximally entangled states. This relation makes it clear that to obtain an entanglement measure one should optimize over all state witnesses. While the subspace witness only optimizes over a restricted set of states, it still provides a stricter bound than the state witness, $C_2 \geq -2W_s \geq -2W_\psi$.

3.1.2 Genuine Multipartite Entanglement (GME)

Finally, we discuss the case for $n > 2$, i.e., detection of genuine multipartite entanglement (GME) via the subspace witness. More specifically, we address the three main aspects of interest: its applicability, its limit (due to measurement cost), and lower-bounding entanglement (beyond detection).

Applicability Recall that the state witness W_ψ detects the class of NPT states, including but not limited to the famous GME states: GHZ, W, and Dicke states. Given that the subspace witness $\langle W_s \rangle = \min \langle W_\psi \rangle$ detects the same states witnessed by W_ψ, it also detects all NPT entangled states.

However, this improved detection comes at an increased measurement cost that we now discuss.

Measurement Cost We first define the measurement cost: whereas W_ψ requires a single fidelity measurement $N = 1$, $\langle W_s \rangle$ requires $N = d(d-1) + 1$ measurements, where d is the dimension of the subspace spanned by the relevant entangled-state basis. We show this explicitly below.

To this end, we first parameterize a multipartite entangled state $|\psi(\vec{\phi})\rangle$ in the computational basis $|k\rangle$ as:

$$|\psi(\vec{\phi})\rangle = \sum_{k=0}^{d-1} a_k e^{-i\phi_k} |\vec{k}\rangle, \tag{3.11}$$

where a_k is the probability amplitude, $\phi_k = \vec{k} \cdot \vec{\phi}$ is the $|\vec{k}\rangle$-dependent phase given a

preset n-length vector of phases $\vec{\phi} = \{\phi_j\}^n$ for every j-th qubit, and d is the dimension of the subspace spanned by the set $\{|k\rangle\}$ specifying $|\psi\rangle$.

While such expression could describe any pure state of n qubits, we are interested in NPT entangled states $|\psi\rangle$ for which state witnesses W_ψ are valid, such as GHZ, W, or Dicke states. For instance, for a general n-qubit GHZ state $|\psi_k\rangle = (|k\rangle + e^{-i\phi}|\bar{k}\rangle)/\sqrt{2}$, we have $a_k = 1/\sqrt{2}$ and the subspace of interest is spanned by $\{|k\rangle, |\bar{k}\rangle\}$ of dimension $d = 2$. For a W state $|W(n)\rangle = \sum_{k=1}^{n} e^{-i\phi_k}|k\rangle/\sqrt{n}$, we have $a_k = 1/\sqrt{n}$ with the subspace of dimension $d = n$ spanned by states $\{|k\rangle\}$ in the one-excitation manifold.

Given this parameterization, the fidelity F_ψ again reduces to a simple expression $F_\psi(\vec{\phi}) = P + C(\vec{\phi})$ with $\vec{\phi} = \{\phi_k\}$ for $k = 1, \ldots, d$. Here, $P = \sum_{k=0}^{d-1} a_k^2 \rho_{kk}$ and $C(\vec{\phi})$ is just a sum similar to Eq. 3.4 extended to all many-body coherences ρ_{jk} of interest:

$$C(\vec{\phi}) = 2 \sum_{j=0}^{d-2} \sum_{k>j}^{d-1} a_j a_k \vec{c}_{jk} \cdot \vec{o}_{kj}, \tag{3.12}$$

where $\vec{c}_{jk} = (\mathrm{Re}(\rho_{jk}), \mathrm{Im}(\rho_{jk}))$ and $\vec{o}_{kj} = (\cos\phi_{kj}, \sin\phi_{kj})$ with $\phi_{kj} = \phi_k - \phi_j$.

Thus to extract the 'subspace' witness $\langle W_s \rangle$ (as was done in $n = 2$ case above) we must identify all $d(d-1)/2$ many-body coherences ρ_{jk} by again solving the set of linear equations given by multiple measurements $F_\psi(\vec{\phi})$, containing a total of $d(d-1)+1$ unknowns. (An explicit example to measure the subspace witness with multiple coherence terms in W state is given in the Appendix of [104].)

Therefore the subspace dimension d, and its scaling with the number of qubits n, sets the limit of which entangled states we can tackle, given that we want to be efficient with respect to QST.

For GHZ states, $d = 2$ is constant and independent of n: in other words, for any n-qubit quantum processor, one can extract the subspace-maximized GHZ witness with just 3 measurements, a very efficient protocol. Indeed, experimentally such subspace-optimized fidelity has been observed with ~ 20 qubits in superconducting and neutral atom systems [121, 84, 102]. We also note that using a 10-qubit register in diamond up to a 7-qubit GHZ state was witnessed with state fidelity 0.589(5) [14]

which could be further optimized with such subspace witness measurement.

For W states, $d = n$: since this is still polynomial in n, all subspace-optimized W_s witnesses will be efficient with respect to QST.

In contrast, for Dicke states, $d = \binom{n}{k} = \binom{n}{n-k}$ with k excitations: therefore, only for very lowly- (highly-) excited Dicke states will $\langle W_s \rangle$ prove efficient with respect to QST.

Lower-bound to Entanglement Finally, the role of the subspace witness as an intermediate metric between entanglement witnesses (detection) and entanglement measures (quantification) can be made more concrete by noting that it can, beyond detection, yield a lower-bound to entanglement given knowledge of the population of ρ also for GME states.

More specifically, the lower bound to an entanglement measure called the GME concurrence C_{GME} [74], related to the separability criteria [44], can be estimated efficiently from experiments as it requires the knowledge of only specific matrix elements of ρ. Both the lower bound to C_{GME} and separability criteria take the form of a difference between the many-body coherences ρ_{jk} within the subspace of interest and appropriate population terms outside the subspace. Similar to entanglement witnesses, these quantities change sign for separable states, as the difference between coherences and population terms changes sign.

For instance, for $n = 3$, the lower bound to GME concurrence is given by:

$$C_{\mathrm{GME}}(n=3) \geq \rho_{18} - \sum_{k,\bar{k}\neq 1,8} \sqrt{\rho_{kk}\rho_{\bar{k}\bar{k}}}, \tag{3.13}$$

where the first term is $\rho_{18} = \langle 000|\rho|111\rangle$, and the second term is the sum of populations outside the GHZ subspace.

We note that the subspace witness $\langle W_s \rangle$ alone is insufficient in providing the lower bound to GME concurrence: $\langle W_s \rangle$ can only provide the first term, as it identifies the true (maximum) coherences of interest. Thus the second term of populations must be identified from additional measurements, but for systems with individual qubit

readout, a single measurement setting (every qubit along z) suffices to identify all the population terms.

Conclusion Having developed a novel metric to more accurately detect entanglement in quantum devices in the presence of local unitary errors, we experimentally demonstrated its advantage over the conventional witness based on the state fidelity with the two-qubit entangled state generated with NV and X electronic spins.

In the next section, we characterize the noise experienced by our quantum register. More specifically, as the first step to accurately characterize the noise affecting a multi-qubit device, we demonstrate a method to build a self-consistent classical noise model for individual qubits.

3.2 Nanoscale Characterization of Spatio-temporal Noise Correlation

In this Section, we present our first step towards investigating the spatio-temporal correlation in the noise experienced by two nearby qubits.

More specifically, given our two nearby electronic spins NV and X (singled out from the larger spin bath), we characterize the noise experienced by the two qubits, as the first step to characterize the correlation between them.

For two spatially proximal qubits, it is expected in general that the noise they experience are correlated, given that they (partially) share the same bath. Aside from the fundamental interest of understanding the correlation effected by various (quantum) baths existing in various QIP platforms, verifying and quantifying the correlated noise across qubits is also of practical interest.

Perhaps one obvious application is in quantum sensing, to reveal also the correlation in the signal arising from a complex (quantum) target of interest, by utilizing spatially separated sensors. Another application of interest would be in characterization of a multi-qubit device, to more completely model and understand their decoherence, and possibly improve two-qubit operations. Furthermore, correlated noise

has also implications for quantum error correction (QEC).

More specifically, for QEC to be successful, the physical qubits must have error probability below a so-called error threshold [101, 62, 59, 1]. Typically, this threshold for the QEC code of interest is estimated assuming independent noise for each qubit, that each qubit has its own independent bath. Thus characterizing the noise correlation between qubits will help test the hypothesis of correlated noise. In the case of non-zero correlation, such characterization could further help either theoretically better estimate of the threshold given the knowledge of correlated noise, or iteratively engineer qubits towards more independent noise should the correlated noise significantly reduce the threshold.

In fact, practical proposals of noise correlation have been recently proposed and as well demonstrated in a proof-of-concept experiment with engineered noise [108, 117]. Then, in relation to our system of proximal spin qubits interacting with the native spin bath, it would be of fundamental interest to understand correlation in the noise effected by the spin bath between the spatially separated qubits.

To that end, as the first step to characterization of correlation *between* the noise experienced by a qubit pair, we set the goal to characterize the noise *itself* experienced by the qubit pair.

Goal More specifically, the goal of this Section will be to build a 'self-consistent' (classical) noise model for each of the two proximal qubits NV and X.

Here we note a few definitions. First, by a 'noise model' $\hat{S}(\omega)$, we mean an effective classical noise process that can (approximately) reproduce the effect of the (quantum) bath, i.e., the qubit decoherence. Second, by a 'self-consistent' noise model $\hat{S}(\omega)$, we mean that the fully-characterized noise model (i.e., with its structure and all its parameters estimated) should be predictive, numerically reproducing at least all the observed measurements of decoherence.

Should such a self-consistent single-qubit noise model be attainable, it would be also of both practical and fundamental interest. More practically, prior knowledge of the noise model can help tailor more robust quantum circuits to minimize decoherence;

and in the limit of negligible correlated noise, the single-qubit noise model should be sufficient for a multi-qubit device. More fundamentally, a good noise model not only provides a physical understanding of the (quantum) bath reduced to a simple classical noise process, but perhaps more importantly gives quantitative characterization (via the identified model parameters) of the bath that the probe qubit is interacting with.

In other words, even by probing individual qubits in spatial proximity, one may gain nontrivial insight into the (quantum) bath of interest. By the end of the Section, by comparing the noise model of the electronic spin bath extracted from the NV and X spins, we will gain some (quantitative) insight into the microscopic structure of the spin bath seen by both qubits.

Potential Problem A priori, there is a potential problem towards our Goal to find a noise model for our two qubits that is self-consistent across various experiments or measurements of decoherence.

In principle, for a qubit or a qutrit, it was shown that a classical noise model is always possible for its evolution under a fixed dynamics (i.e., a fixed 'experiment'), whether or not the noise source is quantum [25].

However, this attained noise model may not be predictive under a different controlled dynamics or experiment. If this is the case, such a noise model is neither so useful in practice nor a 'good' characterization of the (quantum) bath itself–which should be independent of (control on) the qubit.

In fact, this problem of an inconsistent noise model was explicitly demonstrated for an electronic spin in a nuclear spin bath [51]. More specifically, in the weak system-bath interaction regime (with respect to internal bath Hamiltonian H_B), a classical noise model from a particular dynamics could predict decoherence under other dynamics; however, there was a 'phase' transition at a sufficiently strong interaction regime (with respect to H_B), when this noise model failed to be predictive.

Main Results In light of this potential problem, we report our Main Results for the Section.

For the NV spin, it is possible to devise a protocol to build a self-consistent noise model that bridges between the various dynamics, namely Ramsey (R), Echo (E), and CPMG (CP_m) experiments.

For the nearby X spin, it is not possible (yet). Here, the reason may be a technical one, and not in principle, and hence may be reconciled with further work.

Finally, as mentioned above, by comparison of the noise model of the electronic spin bath from NV and X, we are able to gain, while partial, quantitative insight into the physical structure of the microscopic spin environment of NV and X.

3.2.1 Self-consistent Noise Model for NV

Before delving into the details below, we first report the main result: for the NV, we are able to devise a protocol to build a noise model $\hat{S}^{NV}(\omega)$ that is at least self-consistent over all observed dynamics, namely $\{R, E, CP_m\}$. The resulting NV noise model is:

$$\hat{S}^{NV}(\omega) \;=\; \sum_{k=1}^{2} S_k^{OU}(\omega|b_k, \tau_k) + S_0 + S_n(\omega)$$

More specifically, first we verify a double-OU structure, indicating the presence of effectively two distinct electronic spin baths, distinguished by the timescale of their internal dynamics τ_c.

We also observe a noise baseline $S_0 > T_1^{-1}$ that is an order of magnitude larger than the minimum possible (i.e., the qubit energy-relaxation rate T_1) but also not dominated by our control fidelity (pulse errors) in the explored noise frequency range. While we leave for future work to quantitatively decouple or bound the control-induced noise, if the control-induced noise is sufficiently small, this suggests there may be possibly more (quantum) noise source to the NV bath inside the current S_0 component (as inferred from CPMG).

Finally, we observe at specific frequencies certain 'resonance' peaks $S_n(\omega)$. These peaks are expected to be due to the microscopic (resolved) nuclear spins interacting

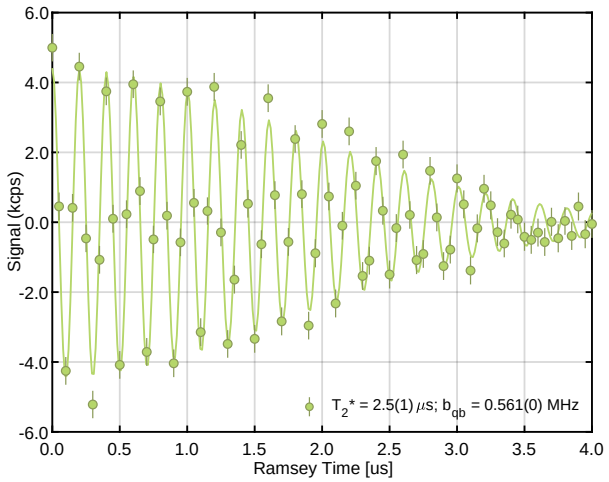

Figure 3-3: **NV Ramsey.** The NV Ramsey experiment R is measured (data points) and fitted to a sinusoidal Gaussian (line).

with the NV [111]. While we leave the exploration of the nearby nuclear environment for future work, e.g., for purpose of building a nuclear spin register, we indeed verify for one peak a single coherent oscillation as expected from entangling with a single nuclear spin.

Given: Ramsey R

We first analyze the (simplest) measurement of decoherence, the Ramsey R, of the NV center shown in Fig. 3-3. First, we observe a Gaussian form of decay, suggesting the NV is dominated by low-frequency noise. If the underlying noise spectrum (and hence a good model) of this NV is a single OU noise source, $S^{NV}(\omega) = S^{OU}(\omega|b, \tau_c)$, then as discussed above, R provides the estimate of $b = 0.56$ MHz, one of two bath model parameters.

Before we move on, we remark on the (rather obvious) insufficiency of only having a subset of knowledge on decoherence (i.e., a subset of $\{R, E, CP_m\}$).

First, in order to extract any meaningful information—i.e., estimate one of the two model parameters—we made two assumptions.

The first was that the noise model is dominated by a single noise source at low frequency, $\hat{S}^{NV}(\omega) = S^{OU}(\omega|b, \tau_c)$ which may not be true. More specifically, recalling the filter function of R admits zero-frequency noise, there could be other undesired

noise sources not associated with the spin bath, e.g., due to (classical) static B-field fluctuations b_{cl} from the external magnet. In other words, we naively assume for now that $b \gg b_{cl}$, such that $\sigma^2 = b^2 + b_{cl}^2 \sim b^2$.

The second was that this OU model should satisfy $(b\tau_c) \gg 1$, which is not guaranteed a priori. Thus to verify this assumption, we need to estimate τ_c of this particular assumed OU source above.

Finally, we recall our goal of building a self-consistent model. Given that we do not yet have a fully-characterized noise model $\hat{S}(\omega)$—i.e., since missing τ_c—we cannot yet check for 'self-consistency' of our proposed model. More specifically, we would check for self-consistency by plugging $\hat{S}(\omega)$ into Eq. 1.9, to to see if our *model* $\hat{S}(\omega)$ can independently predict and reproduce the *measured* NV R decay. By the end of the next section, we will have a few candidate noise models.

Given: Echo E

We now analyze the NV decay under echo, shown in Fig. 3-4. We will do this in (iterative) steps, starting with the simplest possible model that could explain the observed decay E, and checking for self-consistency with the known measurements $\{R, E\}$.

We start with the observation that E can be described well by a simple-exponential decay: e^{-T/T_0}, with $T_2 = 48(2)\mu$s. Therefore, there are two viable noise models $\hat{S}(\omega)$: either white noise $\hat{S}(\omega) = S_0 = 2T_0^{-1}$ or fast OU $\hat{S}(\omega) = S^{OU}(\omega|(b\tau_c) = (bT_0)^{-1} \sim 1)$.

However, both these models are not consistent with R: i.e., neither the decay shape nor timescale of decay is predicted. More specifically, both models predict a simple-exponential R decay, whereas we observe a Gaussian R. As well, both models predict that the timescale of decay in R should equal E, i.e., $T_2^* = T_2$, whereas we see $T_2^* \ll T_2$.

In conclusion, the noise model is not given by a single source of either OU or white noise.

Here, we then make the hypothesis that there should exist at least one quasi-static OU noise source, motivated by the expectation of an electronic spin bath. More

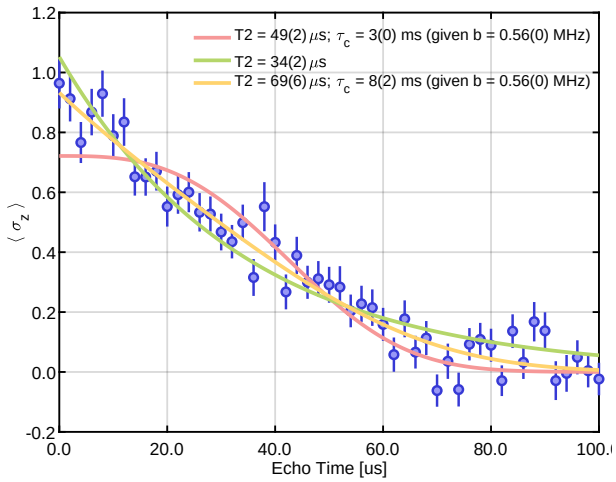

Figure 3-4: **NV Echo.** The NV Echo data E (data points) is fitted to $e^{-(T/T_2)^3}$ (red), e^{-T/T_0} (green), and $e^{-T/T_0-(T/T_2)^3}$ (yellow line) (see main text for discussion).

practically, we try fitting to the combined (competing) decay form $e^{-T/T_0-(T/T_2)^3}$, which in the case of a good fit suggests two viable models: either a double-OU model or an OU + white model.

Here we find a good fit—and better than the simple-exponential fit by RMSE—as seen in Fig. 3-4. Therefore, we have two viable models $\hat{S}_{1,2}$ including either 1 or 2 OU sources: $\hat{S}_1(\omega) = S_{sl}^{OU}(\omega|b, \tau_c) + S_0$ or $\hat{S}_2(\omega) = S_{sl}^{OU}(\omega|b_s, \tau_s) + S_f^{OU}(\omega|b_f, \tau_f)$.

Now we want to check for self-consistentcy of each proposed model. But note that while the first model $\hat{S}_1(\omega)$ is fully characterized (i.e., all model parameters are estimated), while the double-OU model is not (yet).

Numerically calculating $\chi_{R,E}(T)$ under $\hat{S}_1(\omega)$, we find it is consistent with the observed $\{R, E\}$, as seen in Fig. 3-5. In other words, it cannot be ruled out (yet).

In contrast, as $\hat{S}_2(\omega)$ is not fully characterized, we need more knowledge of decoherence. We find in the next section this model will be consistent given more measurements of decoherence, while the $\hat{S}_1(\omega)$ model, while simpler, is no longer self-consistent with the larger set of knowledge.

Given: CPMG CP_m

Here we analyze the final set of measurements, shown by the noise spectrum reconstructed via a set of CPMG CP_m experiments in Fig. 3-6. The measured spectrum

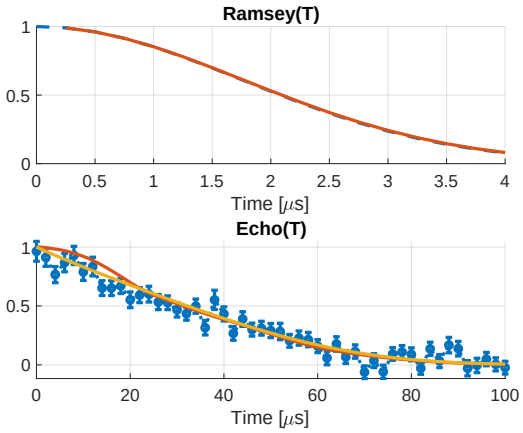

Figure 3-5: **Predicted NV Ramsey and Echo under $\hat{S}_1(\omega)$: Single OU and White Noise Model.** We verify the consistentcy of the single-OU + white noise model $\hat{S}_1(\omega)$ given its numerical reproduction (red line) of the observed decoherence (blue data). The fit of E to the combined decay (yellow line) is shown for reference.

can be explained by a minimal model: $\hat{S}^{CP}(\omega) = S^{OU}(\omega) + S_0 + S_n(\omega)$.

The first term—the (double) OU noise of interest as discussed thus far—is to account for the observed fall-off in the lower end of the measured spectrum $S_{CP}(\omega_m)$ in Fig. 3-6.

The second term is the white noise to account for observed apparent baseline $S_{CP}(\omega_m) > 0$. Of course, a priori we do not expect zero noise $S_{CP}(\omega_m) \to 0$, since even in presence of zero spin fluctuation we should reach the limit $\min_\omega[S_{CP}(\omega)] \sim T_1^{-1} \sim (3\text{ms})^{-1} < 1$ kHz limit. Here we observe $S_0^{CP} \sim 6(1)$ kHz, which is larger than T_1^{-1}, and thus contains more sources of noise. While we do not know the exact (physical) cause of this larger baseline, we give a short discussion. Recall that every point on the noise spectrum $S(\omega_m)$ —including the observed baseline S_0^{CP}—contains contributions from both the 'decohering' noise (i.e., the noise of interest, due to the quantum bath) as well as imperfect control-induced noise (from pulse errors, which is undesired). While it would be ideal to further analyze the contribution due to control-induced error so as to decouple (i.e., subtract) from the observed $S(\omega_m)$, for now we simply note that the dominant component of S_0^{CP} is not the (undesired) pulse errors. In the limit of pulse error-dominated CPMG experiments, the 'baseline' of $S_{CP}(\omega_m)$ should monotonically increase with ω as $\omega = N/T$, with number of pulses

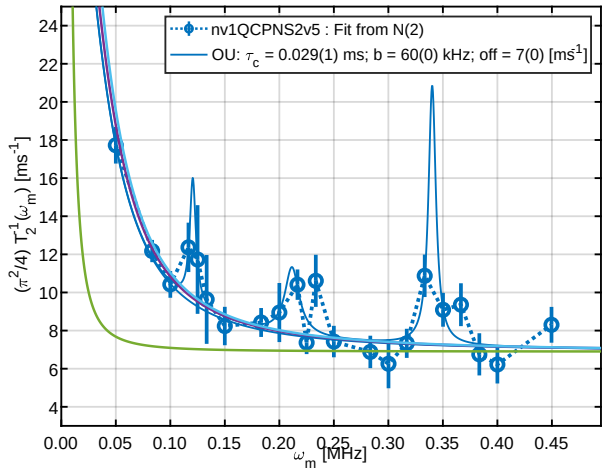

Figure 3-6: **NV Noise Spectrum.** The NV noise spectrum $S^{CP}(\omega_m)$ is measured and fitted to a multi-Lorentizan function (blue line) motivated by its simple noise model $\hat{S}^{CP}(\omega) = S^{OU}(\omega) + S_0 + S_n(\omega)$. More specifically, we observe (and fit well to): the zero-mean Lorentzian given by OU noise $S^{OU}(\omega)$, an overall baseline (well above the $S_0^{CP} > T_1^{-1}$ limit), and additional features (peaks) $S_n(\omega)$ at specific resonances that should arise from the microscopic nuclear environment interacting with this NV. See main text for discussion. The green, purple, and cyan lines are discussed in a later figure.

N. Therefore, the observed 'stable' baseline (over the sampled frequency range) could indicate the presence of noise that is not averaged out by CPMG.

Finally, the third term is to account for the (three) 'features' (peaks) in the noise spectra at certain 'resonance' frequencies. While we leave further characterization of these peaks for future work, these likely originate from resolved nuclear spins in the microscopic environment of the NV. This occurs because CPMG does not cancel interaction from (anisotropic) coupling to nearby nuclear spins [96]. In fact, the CPMG experiments done here (via sweeping N at fixed τ_m) is analogous to the state-of-the-art method of nuclear spin detection (via sweeping τ_m at fixed N) [111]. To gain confidence the peaks should originate from interacting nuclear spin(s), we probe one of the peaks and observe coherent oscillation—as expected for entangling with a nuclear spin. While we leave this for future work, characterizing this resolved nuclear spin(s) will be advantageous to build up a nuclear spin register for the NV for more powerful QIP applications.

We now return to the main interest of a self-consistent noise model. Minimally, we

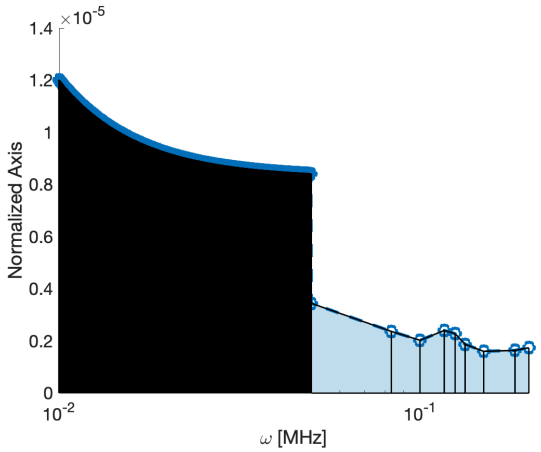

Figure 3-7: **Comparing Proposed Noise Model with Measured Noise Spectrum: Single OU + White Noise** Though the noise model candidate $\hat{S}_1$ could reproduce (via $\chi_{R,E}$) the observed decoherence measurements $\{R, E\}$, it is not consistent with the larger set of knowledge of decoherence $\{R, E, S^{CP}(\omega_m)\}$. The left-hand side (black region) is the proposed noise model from $\{R, E\}$; the right-hand side (blue region) is the measured spectrum $S^{CP}(\omega_m)$ (data points).

want to distinguish between the two proposed models from $\{R, E\}$: $\hat{S}_1(\omega)$ and $\hat{S}_2(\omega)$. To do so, we will check for continuity between these proposed noise models (i.e., the low-frequency noise spectrum informed by $\{R, E\}$) and the measured high(er)-frequency spectrum $S^{CP}(\omega_m)$.

First consider $\hat{S}_1(\omega)$, which was already fully characterized. Even though $\hat{S}_1(\omega)$ could reproduce the observed $\{R, E\}$, it is not consistent with $S^{CP}(\omega_m)$ as seen in Fig. 3-7. More specifically, it is mismatched in both the magnitude ($\frac{\hat{S}_1(\omega_m)}{S^{CP}(\omega_m)} \sim 2-4$) as well as the slope/shape of the spectrum near the boundary.

Now consider the double-OU model $\hat{S}_2(\omega)$, whose missing parameters we must first identify. Assuming continuity at the boundary, i.e., $S^{CP}(\omega_m) - S_0^{CP} = S_2(\omega)$, we can solve for the one unknown given this one equation.

Similarly, given the fully characterized $\hat{S}_2(\omega)$, we first check for consistency between the two sets $\{R, E\}$ and $\{S(\omega_m)\}$, by numerically plotting the model $\hat{S}_2(\omega)$ against the measured OU part of the spectrum $S^{CP}(\omega_m) - S_0^{CP}$. This is plotted in Fig. 3-9.

Finally, as a (final) requirement for self-consistency, we check if $\hat{S}_{double}(\omega)$ can also

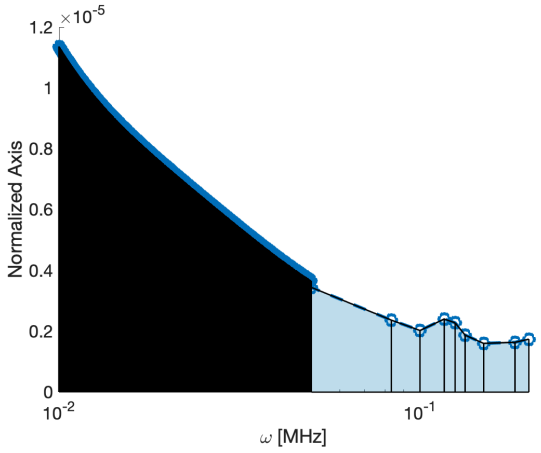

Figure 3-8: **Comparing Proposed Noise Model with Measured Noise Spectrum: Double OU Noise Sources** In contrast with candidate model $\hat{S}_1$, we find continuity between the double-OU candidate model $\hat{S}_2$ (left-side, black region) and the directly measured noise spectrum $S^{CP}(\omega_m)$ (right-side, blue region).

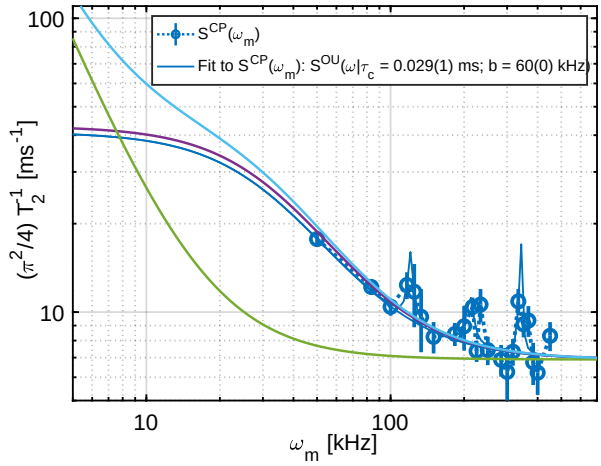

Figure 3-9: **NV Noise Spectrum (Log-log Plot): Testing Consistentcy with Proposed Noise Model(s) from Decoherence Measurements under Ramsey and Echo.** The measured NV noise spectrum $S^{CP}(\omega_m)$ (data points) is compared with the proposed double-OU noise model $\hat{S}_2(\omega) = \hat{S}^{OU}_{slow}(\omega) + \hat{S}^{OU}_{fast}(\omega)$ (cyan line). Surprisingly, we find a near-perfect match (within experimental uncertainty) between the double-OU model and the measured spectrum, indicating the accuracy of the proposed model over (now) wider frequency, beyond the working range of CPMG-based 1QNS. Furthermore, piecing out the individual OU sources (green $\hat{S}^{OU}_{slow}(\omega)$ and purple $\hat{S}^{OU}_{fast}(\omega)$), $S^{CP}(\omega_m)$ can be completely obvlious to the most dominant low-frequency noise (green line) due to its limited working range.

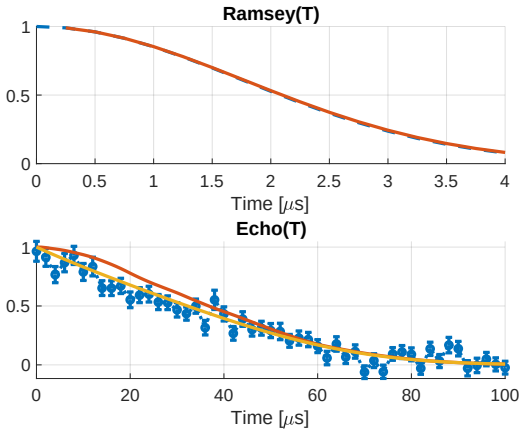

Figure 3-10: **Predicted NV Ramsey and Echo: Double OU Noise Model.** We verify the self-consistentcy of double-OU noise model given its numerical reproduction (red line) of the observed decoherence (blue data). The fit of $E(T)$ to the combined decay (yellow line) is shown for reference.

reproduce the observed $\{R, E\}$ in Fig. 3-10. While its total RMSE in $\chi_E(T)$ is slightly larger than that estimated from $\hat{S}_{double}(\omega)$, it still accounts for the dominant part of the decay. And perhaps more importantly, this is the only model self-consistent with the larger set of measurements, $\{R, E, S(\omega_m)\}$, over the larger range of frequencies.

For one final remark, the order of analysis (studying $\{R, E\}$ first) to reach a self-consistent model is not unique. One could have just as well formed a model from $S^{CP}(\omega_m)$ first. In this case, by simply fitting $S^{CP}(\omega_m)$ to the 3-term model $\hat{S}^{CP}(\omega_m)$ above to a multi-Lorentzian function, we independently get the same parameters of (b_f, τ_f). This is in principle possible because the 'slow' OU spectrum has fully decayed well before ω_{min}—and thus the measured $S^{CP}(\omega_m)$ is completely blind to near zero-frequency noise. The fact of 'missing' noise power is highlighted when attempting to reproduce $\{R, E\}$ numerically via $\chi(T)$. The predicted $\chi(T)$ does not lead to an appreciable decay, given that the current noise model lacks more than 90% of the true underlying noise power as stored in the (missing) slow OU source.

To summarize, for the case of an electronic spin qubit interacting with a many-body e-spin bath, we achieve a self-consistent noise model by combining measurements of decoherence in the full set $\{R, E, S^{CP}(\omega_m)\}$ that is strictly improved with more measurements.

We now apply the same protocol to characterize the bath of another electronic spin, that is nearby (interacting) with the NV spin we have just analyzed.

3.2.2 Self-consistent Noise Model for X

Before the analysis, we first state our (tentative) result: we could not yet verify a noise model for the dark spin X that is self-confident with the observed $\{R, E, CP_m\}$. However, this may be a technical problem, and not one of principle as in Section 3.2, and thus may be reconciled with further work. The tentative noise model for X is:

$$\hat{S}^X(\omega) \quad = \quad S^{OU}_{slow}(\omega|b_s, \tau_s) + S_0 + S_n(\omega)$$

More specifically, we first verify a (dominant) quasi-static single-OU structure, indicating that X samples noise from (one) electronic spin bath with slow internal dynamics τ_c. This is in contrast with NV, which was observed to sufficiently sample noise from another group of spins with faster τ_c. We leave the comparison of the quasi-static spin bath—as observed by either NV or X—for the next section.

We also observe a noise baseline $S_0 > T_1^{-1}$ that is an order of magnitude larger than the minimum possible (i.e., the qubit energy-relaxation rate T_1), as was observed with the NV. However, this baseline is larger than that of the NV: $(S_0^X/S_0^{NV}) \sim$ 2-3. Given that the control fidelity for X has been significantly reduced (whose reason will be important with respect to our ultimate objective of noise correlation spectroscopy), we must first identify whether this observed S_0^X is dominantly the 'true' noise (i.e., due to the bath), and not 'false' noise (due to control or pulse error). This missing technical piece of information is the reason for the yet tentative result. Nonetheless, if we naively assume that the observed S_0^X is not dominated by control errors, then the above noise model $\hat{S}^X(\omega)$ is self-consistent.

Finally, similarly with the NV, we also observe at certain 'resonance' peaks $S_n(\omega)$, expected to result from the microscopic (resolved) nuclear spins interacting with X [96, 111].

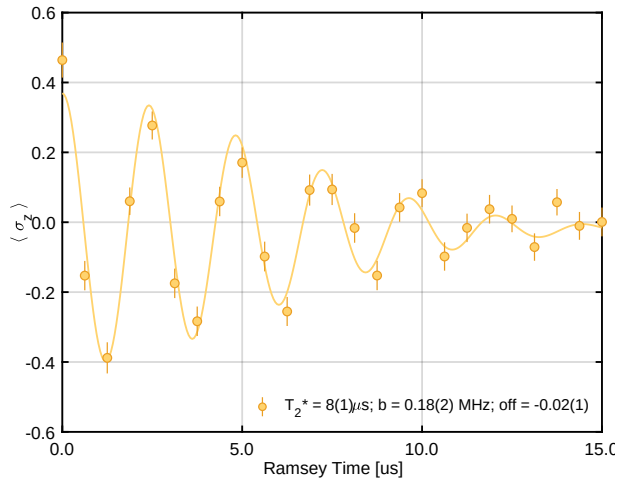

Figure 3-11: **X Ramsey.** The X Ramsey experiment $R(T)$ is measured (data points) and fitted to a sinusoidal Gaussian (line).

Given: Ramsey R

Here, we carry out the same analysis as with the NV, with the same assumption of dominant quasistatic OU noise and negligible classical field fluctuation. Then, we estimate that X sees an effective noise strength $b^X = 0.20(2)$ MHz. This is approximately 3 times weaker noise strength (and 3 times longer coherence time) than that of the NV.

Given: Echo E

We now analyze the echo of spin X, where we observe another striking difference in the effective baths experienced by the nearby e-spins NV and X.

The most apparent difference is in the observed E decay shape: it is described well by a decay that is cubic in exponential (quasi-static OU). In other words, the dark spin X samples dominantly from the quasi-static spin bath, such that a single quasistatic OU model is self-consistent with $\{R, E\}$. In contrast, the NV sampled noise sufficiently strongly from another electronic spin bath (with faster τ_c), such that it cannot be described by a single OU.

Via the same fitting procedure as that of NV, the dark spin X echo is fit equally well (by RMSE) to both $\{e^{-(T/T_2)^3}, e^{-T/T_0-(T/T_2)^3}\}$. This suggests there are 3 viable

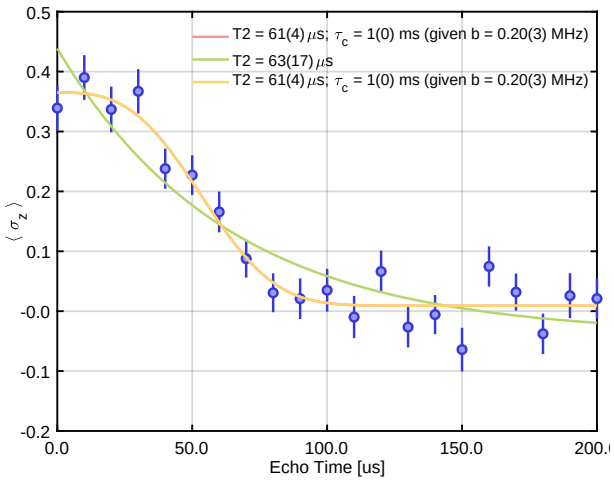

Figure 3-12: **X Echo (Unmodulated Readout Phase).** The X Echo experiment $E(T)$ is measured (data points) and fitted to a cubed-exponential decay (pink line—overlapping with yellow line) and a simple-exponential decay (green line). In contrast with NV decoherence under $E(T)$, X shows a cubed-exponential decay, and hence dominated by quasi-static OU noise. Also, in contrast with NV $E(T)$, X $E(T)$ is not well-described a simple-exponential. Finally, as done for NV $E(T)$, we also fit to the combined decay of simple- and cubed-exponential (yellow line). In this (typical) unmodulated $E(T)$ decay envelope, the fit simply converges to the cubed-exponential. We will see that in the readout-phase-modulated $E(T)$ data—to introduce artificial phase modulation in the signal—we are able to find an equally good fit (by RMSE) to the combined decay.

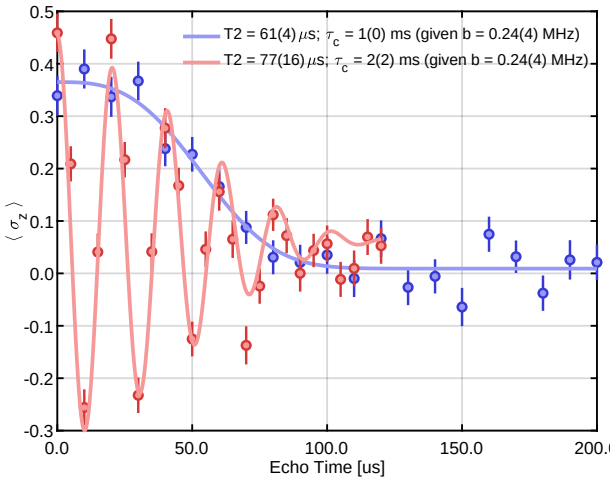

Figure 3-13: **X Echo (Modulated Readout Phase).** The X Echo experiment $E(T)$ is measured also with the phase of the readout $\pi/2$-pulse modulated, in order to introduce artificial oscillation. (While the two $E(T)$ experiments are identical, they are measured with(out) readout signal modulation to increase confidence in the fit result.) Indeed, when fitted to a cubed-exponential (not shown), they independently yield the same T_2. Regarding the fit to the combined decay (lines)—motivated by the successful double-OU noise model for NV— while the fit of unmodulated signal converges to the cubed-exponential (due to likely best RMSE), the fit of the modulated signal is able to find just as good fit (by RMSE).

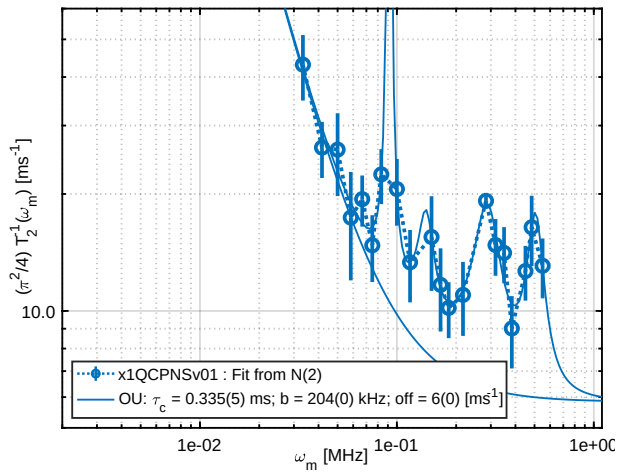

Figure 3-14: **X Noise Spectrum: At (Relatively) Large Rabi Power** Ω_0 The X noise spectrum $S^{CP}(\omega_m|\Omega_0 = 2.5\text{MHz})$ is estimated and fitted to a multi-Lorentzian function (blue line) motivated by its simple noise model $\hat{S}^{CP}(\omega) = S^{OU}(\omega) + S_0 + S_n(\omega)$. Similarly with NV, we observe (and fit well to): the zero-mean Lorentzian given by OU noise $S^{OU}(\omega)$, an overall baseline (well above the $S_0^{CP} > T_1^{-1}$ limit), and additional features (peaks) $S_n(\omega)$ at specific resonances that should arise from the microscopic nuclear environment interacting with this X. However, we notice the observed noise magnitude is (statistically) significantly larger with respect to not only the measured NV spectrum but also more importantly the proposed noise models from X $\{R, E\}$. We explore the cause of this in the main text.

models: $\hat{S}_{slow}$ (i.e., a single OU), $\hat{S}_1$ (i.e., a single OU + white), and $\hat{S}_2$ (double OU).

Again, the first two of the three models are fully characterized and hence can be numerically checked for self-consistentcy with existing knowledge $\{R, E\}$—and they are. The double-OU model, as before, requires further knowledge to characterize. Therefore, we turn to 1QNS in attempt to reach the most accurate model.

Given: Noise Spectrum $S(\omega_m|\Omega_0 = 2.5\textbf{MHz})$

First, we report the reconstructed noise spectrum $S^{CP}(\omega_m|\Omega_0 = 2.5\text{MHz})$ of dark spin X using Rabi power $\Omega_0 = 2.5\text{MHz}$ in Fig 3-14.

While this measured $S^{CP}(\omega_m)$ is well-modeled by the same 3-term model used for the NV spectrum, we see one problem: this measured spectrum is not consistent with any of the 3 models proposed from $\{R, E\}$.

More specifically, the first two out of the three viable models ($\hat{S}_{slow}$ and $\hat{S}_1$) are al-

ready fully characterized with $\{R, E\}$ and hence can be numerically compared against the measured $S^{CP}(\omega_m \geq \omega_{min})$ to check for continuity. Instead, we observe a significant mismatch, in both the magnitude and slope/shape for these two models. On the other hand, the double OU model requires at least one data point $S^{CP}(\omega_m)$ which carries information of a (double) Lorentzian. However, due to the large magnitude of $S^{CP}(\omega_m)$, we end with an imaginary estimate of τ_c (given a negative argument under the square root).

To diagnose the problem, we hypothesize that this inconsistency between the two sets of decoherence measurements $\{R, E\}$ and $S^{CP}(\omega_m)$ is caused by the presence of near-resonant *and* interacting spins (NRI-X) with the dark spin X.

We note this hypothesis is not a priori intuitive from the measurement of $S^{CP}(\omega_m|\Omega_0 = 2.5\text{MHz})$ alone. However, if this is true, this could explain the larger-than-expected noise magnitude, i.e., decay rate under CPMG. In fact, in the presence of NRI-X, we would not be performing a true (1-qubit) CPMG; rather, we would be co-driving (off-resonantly) a group of these near-resonant and interacting spins along with X. In other words, we would not be measuring the desired 1-qubit CPMG decay of the X spin, but rather a (faster) multi-qubit (SEDOR) decay [29].

If this hypothesis is true, then ideally we should be able to confirm it from the simpler experiment of (nominal) echo $E(T|\Omega_0 = 2.5\text{MHz})$ on the X spin. More specifically, in the presence of NRI-X, we expect to observe either a coherent oscillation(s) (as expected given coupling to just a few spins, resolved within T_2^X) or instead just a faster decay (a *group* of spins, unresolvable within T_2^X). Indeed, we observe a signal containing small-amplitude oscillation(s).

Given the confidence that $\Omega_0 = 0.25$ MHz should allow (true) 1-qubit control, we attempt to reconstruct a more accurate 1-qubit noise spectrum $S^{CP}(\omega_m|\Omega_0 = 0.25\text{MHz})$. Recalling the working range of CPMG-based 1QNS, we will only be able sample a very limited, low-frequency end of the spectrum $S^{CP}(\omega_m \ll \Omega_0 = 0.25\text{MHz})$; however, given a good estimate of OU parameters with a limited sample of the NV $S^{CP}(\omega_m)$, we hope to still be able to distinguish between the 3 models even with this limited range.

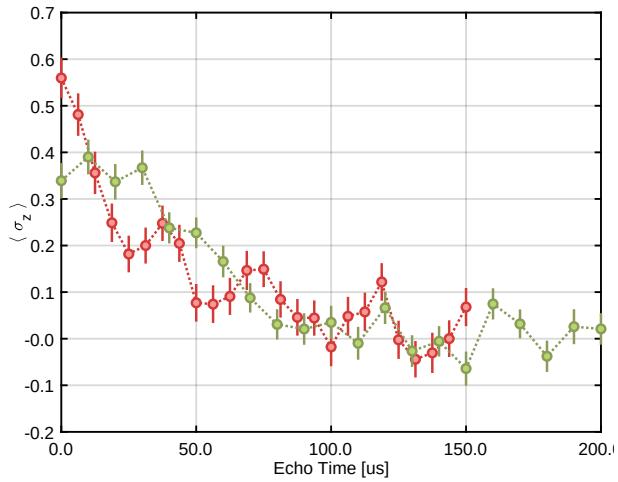

Figure 3-15: **X Echo: At (Relatively) Large Rabi Power Ω_0.** The X Echo experiment $E(T|\Omega_0 = 2.5\text{MHz})$ is measured (red data points), shown against the reference $E(T|\Omega_0 = 0.25\text{MHz})$ (green data points). While we leave quantitative analysis for future work, we observe the larger Rabi Ω_0 introduces small-amplitude oscillations. This supports the hypothesis of the presence of near-resonand and interacting (NRI-X) spins for our X spin (see main text for discussion). In other words, at larger Rabi Ω_0, we can no longer perform desired (1-qubit) echo or cpmg experiments with our X spin, given that we also co-drive (off-resonantly) these NRI-X spins.

Given: Noise Spectrum $S(\omega_m|\Omega_0 = 0.25\textbf{MHz})$

Thus reconstructing $S^{CP}(\omega_m|\Omega_0 = 0.25\text{MHz})$ in Fig. 3-16, we simply observe a flat line, suggesting a (large) white noise baseline.

Returning to the goal of a self-consistent noise model, in fact, the measured baseline S_0^{CP} is equal (within 1 error bar) to $\hat{S}_1$, the (single OU and white)-noise model predicted from $\{R, E\}$.

However, there is one technical problem with continuing with analysis: given the significantly weaker Ω_0 (and long pulse length $L = (2\Omega_0)^{-1}$), the control or pulse fidelity $F_\pi|\Omega_0 = 0.25$ MHz is significantly reduced with respect to either $F_\pi|\Omega_0 = 2.5$ MHz (or that of NV) as shown in Fig. 3-17. Recalling that the $S^{CP}(\omega_m)$ contains both the (desired) noise from the bath as well as the (undesired) control-induced decay, with increased pulse error, we are no longer as confident in $S^{CP}(\omega_m)$, at least relative to our results from $\{R, E\}$ (which only contain 2-3 pulses). Therefore, we have further work to ideally decouple the pulse error from the spectrum $S^{CP}(\omega_m|\Omega_0 = 0.25)$—and

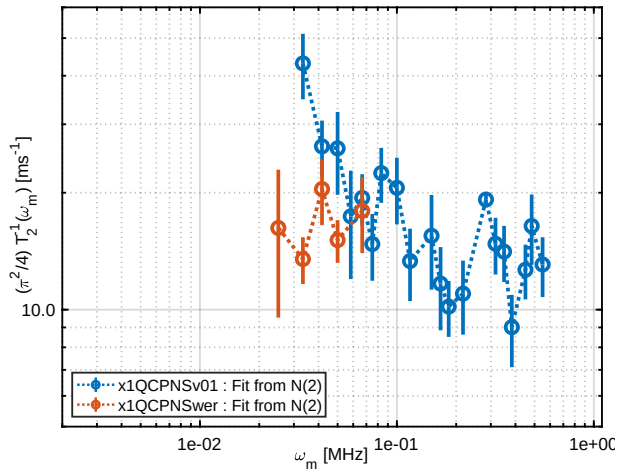

Figure 3-16: **X Noise Spectrum: At Weak Rabi Power** Ω_0 The X noise spectrum $S^{CP}(\omega_m|\Omega_0 = 0.25\text{MHz})$ (red data) is re-measured at low Rabi power in its allowed (limited) range, plotted against the previous estimate $S^{CP}(\omega_m|\Omega_0 = 2.5\text{MHz})$ (blue data). In support of the hypothesis of the presence of near-resonant and interacting spins for X (NRI-X), we observe weaker noise or decay rate at smaller Ω_0, despite the worse control pulse fidelity F_π. Unfortunately, given the worse F_π, there should be increased contribution from pulse error in the measured $S^{CP}(\omega_m|\Omega_0 = 0.25\text{MHz})$. Therefore, before checking for self-consistency in our noise models for X, we should estimate and decouple the pulse error contribution from $S^{CP}(\omega_m|\Omega_0 = 0.25\text{MHz})$.

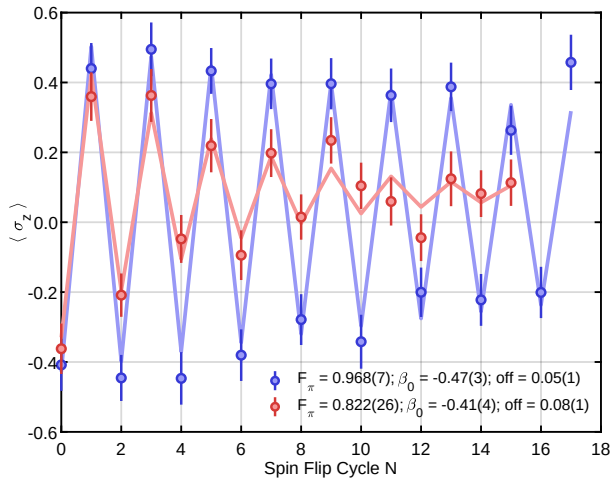

Figure 3-17: **X Control Fidelity: Two-tone π-pulse Fidelity** We characterize the state fidelity of the calibrated two-tone π-pulse F_π used to simultaneously drive both hyperfine resonances of the X electronic spin. We observe a reduced F_π at reduced Rabi power Ω_0, most likely due to decay during the (weaker and longer) driving pulse.

this should the last missing piece to reach a self-consistent, single-qubit noise model for 2 nearby spins.

Before we end this section, we make one final remark about this observation of the potential presence of (a group of) NRI-X spins.

Consider first no NRI-X spins, and that we have perfect control fidelity on the dark spin X $F_\pi \neq F_\pi(\Omega_0)$ at any Rabi power Ω_0. In such a case, we would recover the true (1-qubit) $S^{CP}(\omega_m)$ at any Ω_0: $S^{CP}(\omega_m|\Omega_0 = 2.5\text{MHz}) = S^{CP}(\omega_m|\Omega_0 = 0.25\text{MHz})$.

Now we add in the more realistic condition that $F_\pi(\Omega_0 = 2.5\text{MHz}) > F_\pi(\Omega_0 = 0.25\text{MHz})$. Then, necessarily we should measure $S^{CP}(\omega_m|\Omega_0 = 2.5\text{MHz}) < S^{CP}(\omega_m|\Omega_0 = 0.25\text{MHz})$. However, we observe the opposite, as seen in Fig. 3-16.

In other words, this suggests that the noise (i.e., decay rate) at $\Omega_0 = 2.5$ MHz is significantly larger than that at $\Omega_0 = 0.25$ MHz—in spite of the smaller control-induced noise. Thus, the 'true' noise contribution (due to the bath) is somehow being affected at larger $\Omega_0 = 2.5$ MHz, i.e., the bath is somehow affected. Then one consistent picture would be the presence of spins in the bath of X that are *near-resonant* with X (so they are co-driven by drive resonant with X) and as well *interacting* (so not to be not canceled out by X Echo or CPMG pulses). Furthermore,

likely there is a group or multiple of such NRI-X spins, leading to the faster decay.

In fact, the presence of NRI-X is prohibitive of our ultimate objective: characterization of correlations in the noise between spatially proximal qubits. Limited to weak Rabi Ω_0, it significantly limits the working range of the methods recently proposed for two-qubit noise cross-correlation spectroscopy [108, 117]. While there may be a possibility to study a weakly driven bath at a compromised Rabi $\Omega_0 > 0.25$ MHz, it will still be against our original intent of characterizing the correlated noise induced by the natural (unperturbed) electronic spin bath on two spatially nearby spins.

However, the presence of NRI-X may also leave open a possible interesting future work. More specifically, if these NRI-X spins can be coherently controlled, e.g., are part of the spin bath with long τ_c, we may be able to utilize the X spin to characterize the smaller, 'coherent' part of the bath (instead of characterizing the larger, 'incoherent' bath per our original intent). If this can be achieved, this would demonstrate increased scalability of dark electronic spin registers in solid-state QIP systems [32].

3.2.3 Comparison of the Quasi-static Electronic Spin Bath as Observed from Two Proximal Spins

A priori (before experiments), given that NV and X are two (nearby) electronic spins, and the noise model describes the effect of the (same) bath they interact with, we expect qualitatively that they should have the same noise sources or overall structure. And indeed the (tentative) noise models, consistent with experiments, observe this:

$$\begin{aligned} \hat{S}^{NV}(\omega) &= S^{NV}_{slow}(\omega|b_s,\tau_s) + S^{NV}_{fast}(\omega|b_f,\tau_f) + S^{NV}_0 + S^{NV}_n(\omega) \\ \hat{S}^{X}(\omega) &\sim S^{X}_{slow}(\omega|b_s,\tau_s) + S^{X}_0 + S^{X}_n(\omega) \end{aligned}$$

Thus rather what is interesting would be in the (varying) details, where the differences should arise from differences in the exact microscopic configuration of the bath centered around each spin.

Therefore in this section we give a (limited) comparison of the noise models, i.e., of only the self-consistent components. Recall from above that, for the case of dark spin, we have not yet verified which of $\hat{S}_{1,2}$ is self-consistent. More specifically, we do not know if $S^X_{fast}(\omega|b_f, \tau_f)$ should exist (as may be expected from $\hat{S}^{NV}(\omega)$), given that it may be presently hidden inside S^X_0, which may be over-estimated due to control-induced error. Therefore, leaving this for future work, we limit the discussion to the two terms that are (approximately) self-consistent: $S_{slow}(\omega|b_s, \tau_s)$ and $S_n(\omega)$.

$S_n(\omega)$: Given Microscopic 'Nuclear' Environment

One 'common' noise source for both NV and X are the peaks observed at certain 'resonance' frequencies under CPMG: $S_n(\omega)$. These 'resonances' are expected to originate from coherent interaction with (resolved) nuclear spins, in which case the peak positions should be given by the nuclear Larmor frequency and the hyperfine interaction strengths [111]. For one resonance peak of NV, we indeed observe a coherent oscillation as expected from entangling with a single nuclear spin. We note that further work to identify the (interaction Hamiltonian with) the nuclear spins would be advantageous to build a nuclear register around the central electronic spin.

For the purpose of comparison, assuming (some of) these peaks are indeed due to nuclear spins, then we expect that the nuclear 'resonances' observed by NV are not observed by X or vice versa—due to their (most probable) distance of 9nm (with coupling strength $d \sim 60$ kHz). For a rough estimate, imagining a nuclear spin in the center of the two electronic spins, we may expect a dipolar coupling strength of $d' \sim (\Delta r)^3/(\gamma_e/\gamma_n)d \sim 2^3/10^3 d \sim 0.01d$, which is too weak to be detected within the coherence time of either spin (as seen by their measured noise spectrum). If instead the nuclear spin were brought closer to the NV, then it should have a higher (lower) chance of being detected by NV (X).

$S^{OU}_{slow}(\omega|b, \tau_c)$: Given Quasi-static Electronic Spin Bath

Finally, we compare the (model of) the quasi-static electronic spin bath as seen by either NV and X. More specifically, we compare the model parameters (b, τ_c).

Recall that from Ramsey experiment, we could estimate b, assuming that any (true) classical field fluctuation $b_{cl} \ll b$ of interst. In this case, we found $b^{NV}/b^{X} \sim 3$.

Recall that $b^2 = \sum_k b_k^2$, where b_k is the coupling strength between the central qubit to k-th spin of the bath [34]. Hence, given that b depends on the exact microscopic spin bath configuration with respect to the central qubit, a priori it is not surprising they should be different. Furthermore, if this b belongs to a quasistatic OU (as was verified), then there is a (linear) relationship between b and e-spin concentration (averaged over many bath configuration realizations) [120]. Therefore, $b^{NV}/b^{X} \sim 3$ also implies that X spin sees a roughly 3-fold more dilute electronic spin configuration than that of X. While there may be more than one cause, one physical cause may be due to the (spread of) the ion-implanted nitrogen or electron donors into the diamond, yielding (approximately) a Gaussian concentration profile.

Aside from the difference in b, perhaps more interesting, is seen in our estimates of τ_c for the slow bath: the X experiences a quasi-static bath with 2-4 times faster dynamics than that seen by the NV (albeit the same order of magnitude). Here we make some qualitative analysis of this observation.

A priori, this is perhaps more surprising than the difference observed in b's, because τ_c is a (qubit-independent) intra-bath parameter. If indeed NV and X were seeing exactly the same spin bath, we should readily expect different coupling b (since this depends on the relative position between qubit and bath) but the same internal dynamics τ_c. Therefore, the small but statistically significant difference in τ_c suggests that, while the quasi-static spin bath for NV and X is 'similar,' it should not be exactly the same.

Perhaps what is more surprising is that the X bath dynamics is *faster* ($\tau_c^{NV}/\tau_c^{X} > 1$)—in spite of it being effectively 3-fold more dilute and weaker intra-bath dipolar coupling. Therefore, what this observation suggests is this: the microscopic X bath, while more dilute on average, should be composed of spins closer in resonance, relative to those comprising the NV bath. This comes from estimation of the spin flip-flop rate via Fermi's golden rule[125]: the flip-flop rate should be proportional to the dipolar coupling strength (squared) of the spin pair but approximately inversely proportional

to their difference in resonance (squared).

While this inference into the bath composition – i.e., (i) a heterogenous spin bath seen by NV and X and (ii) relatively closer-in-resonance bath spins for X – will remain a speculation, we already have some (even if weak) evidence in support of the speculation. First, we have evidence for the heterogeneity of the electronic spin bath. This is seen from (every) electronic spin coherently coupled to the NV (see Fig. 2-2): all of the observed electronic spins have a difference in resonance $\Delta\omega > 1 - 7$ MHz (given by their individual nuclear hyperfine interaction), which is $2 - 4$ orders of magnitude larger than the observed dipolar coupling strengths. Second, the evidence that the X bath may contain spins closer in resonance (compared to the bath of NV) may be related to the reason we could not achieve a self-consistent noise model for X. The presence of near-resonant spins interacting with X acts as the bath of X that, despite potentially weaker intra-bath coupling, may flip-flop faster due to smaller off-resonance between the spins.

Conclusion As the first step to characterize the coherence of a multi-qubit register, we characterized the noise experienced by two spatially proximal qubits – and found two varied results.

For the NV qubit which is well isolated (distinguishable) from the bath, it was possible to build a classical noise model that is self-consistent with a varied set of dynamics – indicating an accurate characterization of the bath. For the X qubit, it was not possible – rather, we found evidence for a more complex and quantum X qubit that may involve a group of near-resonant, interacting electronic spins. Hence, while a self-consistent model allows an accurate characterization of the unknown, potentially quantum bath, the preclusion of a self-consistent model may instead signal the presence of an interesting bath to further investigate. For instance, in this specific case, the presence of a coherently interacting group of electronic spins may help further scale up the quantum register of electronic spins, beyond the coherence time of the central NV spin.

Chapter 4

Demonstrate a quantum information task: Quantum sensing

Having characterized the quantum register and verified two-qubit entanglement in the previous Chapter, in this Chapter we put the device to the test to demonstrate quantum advantage in sensing.

In other words, the first quantum information task of interest for our electronic spin register is in sensing, given that single-qubit sensors in the solid-state, most prominently with NV center in diamond, have proved excellent sensors of nanoscale local fields [75, 112, 67, 27, 20]. (Whereas an ensemble sensor of large n, with the advantage of significantly enhanced SNR, would measure averaged fields over a larger volume.)

Entangled states have been touted to bring quantum advantage to sensing [12], but given increased complexity to generate and control such states leave open the question of whether quantum advantage can be achieved in practice [54]. In this Chapter, we address this question starting from the simplest system of two electronic spins. In other words, the question we want to answer in this Section is: can the performance (sensitivity) of this single-qubit sensor be enhanced if given access to a nearby electronic spin?

As of yet, 'true' quantum sensing via entanglement with an electronic spin register, while proposed, has not been explored experimentally [41, 36, 43, 63, 95]; this will

the topic of this Chapter.

Goal The goal of this Chapter will be to demonstrate a path towards quantum advantage in nanoscale sensing, by use of one additional nearby electronic spin.

To this end, we first define a gain in sensitivity $g \equiv \frac{\eta^1}{\eta^e}$, in order to compare the sensitivity of the single-qubit sensor η^1 vs. the two-qubit entangled sensor η^e. By analyzing the main factors determing g, we see what conditions will allow quantum advantage $g > 1$.

Then, we will experimentally demonstrate the path towards quantum advantage in two steps. More specifically, we first characterize the sensitivity of our single-qubit (NV) sensor η^1 and that of $n = 2$-entangled (NV and X) sensor η^e.

However, as it will prove difficult to achieve $g > 1$ via entanglement-enhancement alone, we demonstrate an independent method to further enhance sensitivity, by utilizing the electronic spin register not only as an entangled sensor but also a memory after sensing.

Problem The main challenge in achieving quantum advantage for sensing with entanglement, as we will see below in detail, is the 'cost' of entanglement, or the degraded sensitivity due to generating (and measuring) entangled states.

Recall that an n-qubit maximally-entangled sensor promises an n-fold enhancement in sensitivity. (Where maximally-entangled states are the Bell states for $n = 2$ and GHZ states for $n > 2$.) In comparison, an ensemble of n uncorrelated qubits—equivalently a single qubit measured n times if not considering time as a resource—only yields only a $\sqrt{n}$ enhancement in SNR, just as in a classical sensing scheme. This sensitivity gain of $\sqrt{n}$ is the main motivation for entanglement-enhanced sensing [12, 54].

While the $\sqrt{n}$-scaling gain in sensitivity should promise quantum advantage in the limit of large n, for the purpose of sensing with nanoscale resolution, there is a limit to the sensor size n. In other words, there is only a finite n available for improvement. In such a case, other factors affecting sensitivity η—besides the n improvement—will

be significant.

More concretely, working against $\sqrt{n}$-fold enhancement in sensitivity is the accompanied cost to generate, maintain, and readout the desired entangled state, which is strictly larger with respect to (ensemble of) single qubits. As we will see below, there are 3 main factors that will degrade the sensitivity η: (i) decreased state-preparation-and-measurement fidelity for entangled states, (ii) faster decoherence of n-entangled states, and (iii) increased idle time required to prepare and measure entangled states, which instead one could have used on the sensing task to increase SNR. These 3 factors work in concert to decrease the possible amount of entanglement-enhanced advantage.

Main Results We first state our main results.

As the first step towards the goal, we demonstrate entanglement-enhanced sensing with our two-qubit system of NV and X electronic spins, by verifying an n-factor improvement (where $n = 2$) over the working range or bandwidth $\omega_{ac} \equiv (2\pi)\tau^{-1}$ of the sensor. However, due to the cost associated with entanglement, our particular two-qubit device does not achieve $g > 1$.

Given the difficulty of achieving $g > 1$ via entanglement alone, we demonstrate an independent way to extend the upper bound in sensitivity for the $n = 2$-qubit device by a factor $\text{SNR(M)} \leq \sqrt{M}$. This, inspired by the repetitive readout of a nearby nuclear spin [57], is achieved by repurposing the dark electronic spin X as a classical memory bit after its sensing task. By querying the electronic memory bit M times, the two-qubit device can gain enhanced sensitivity by a factor $\text{SNR(M)} \leq \sqrt{M}$.

4.0.1 Gain in Sensitivity g

To compare (any) two sensors, one natural metric of interest is to compare their sensitivities η for the same sensing task. Given our Goal to demonstrate quantum advantage with an $n = 2$-entangled sensor vs. a $n = 1$ sensor, we define as our metric

of interest the gain g:

$$\begin{aligned} g &\equiv \frac{\eta^1}{\eta^e}, \\ &= g_{N=1}\sqrt{\frac{N_e}{N_1}}, \\ g_{N=1} &= \frac{\eta^1_{N=1}}{\eta^e_{N=1}}. \end{aligned}$$

Just as with sensitivity η, g can be pieced out as the single-shot component $g_{N=1}$, which then can be improved (or degraded) when considering equal experiment time $T = N(\tau + t_{idle})$ for both sensors. More specifically, $g_{N=1}$ determines which sensor is better at a particular sensing task, after a single operation $N = 1$. But this metric $g_{N=1}$ does not consider time as a resource. Therefore, setting the (same) total allowed experiment time for both sensors $T_e = T_1$, we can more fairly compare both sensors. Then, the (relative) repetition rate of the sensor $\frac{N_e}{N_1}$ has the final say in whether $g > 1$ can be achieved.

As is expected, for the same sensing task (i.e., same sensing time $\tau \equiv \omega_{ac}^{-1}$) given to both sensors, we will strictly observe:

$$\sqrt{\frac{N_e}{N_1}} = \sqrt{\frac{\tau + t_1}{\tau + t_e}} < 1.$$

This is because, on top of the (same) time t_1 to initialize and read the central qubit (NV), the quantum sensor additionally requires initialization time t_{init} (to initialize the additional electronic spin from the environment) and $t_{entangle} + t_{disentangle}$ (to generate and then readout the entangled state):

$$\begin{aligned} t_e &= t_1 + t_{add}, \\ t_{add} &= t_{init} + t_{entangle} + t_{disentangle}. \end{aligned}$$

Therefore, if the quantum sensor is to achieve quantum advantage $g > 1$, it must

first secure a sufficiently large single-shot gain $g_{N=1}$:

$$g > 1 \;\; \Rightarrow \;\; g_{N=1} > \left(\sqrt{\frac{N_e}{N_1}}\right)^{-1} > 1.$$

Then, by plugging in the sensitivity calculated above (Eq. 1.5), we can identify what factors determine $g_{N=1}$:

$$g_{N=1} \;\; = \;\; n\left(\frac{\alpha_n}{\alpha_1}\right)\left(\frac{e^{-\chi_n(\tau)}}{e^{-\chi_1(\tau)}}\right).$$

Here, note that the uncertainty in signal σ_S has canceled out, as it is the same for both sensors given that for both measure through the (same) NV.

We can now more concretely separate the 'good' terms (i.e., > 1) vs. the 'bad' (< 1)—or equivalently, the entanglement-enhancement vs. its cost.

The first term $n > 1$ is the n-fold enhancement due to entanglement. This n is independent of τ (hence any specific sensing task) and enhances g for all τ .

The second term $\frac{\alpha_n}{\alpha_1} < 1$—as the first cost of entanglement— pertains to the increased complexity of the quantum circuit required to generate entanglement. More specifically, it compares how much n-body coherence of an n-maximally entangled state ($n = 2$ for Bell states; $n > 2$ for GHZ states) can be prepared and measured vs. a single qubit: $\frac{\alpha_n}{\alpha_1} = \frac{(\langle 00..0|\rho|11..1\rangle + h.c.)}{\langle 0|\rho|1\rangle + h.c.}$. It is strictly below 1 for the same reason $t_e > t_1$: in *addition* to the (same) single-qubit controls, the quantum sensor requires multi-qubit control to (dis)entangle and to initialize. Given that no gate is perfect, even a single additional gate leads to a strict sub-unity. Finally, $\frac{\alpha_n}{\alpha_1}$ is also independent of τ, because it simply quantifies how good of an n-maximally entangled state can be prepared (and meaured) vs. a single qubit—independent of whether or not the prepared quantum states are then utilized for sensing.

Finally, the third term $\frac{e^{-\chi_n(\tau)}}{e^{-\chi_1(\tau)}} \leq 1$—as the second cost of entanglement—pertains to the faster decoherence of n-maximally entangled states. As we will see in the next Chapter, the exact form of decay $\chi(\tau)$ will depend on both the underlying (quantum) bath and the specific quantum circuit/control applied to the qubits. Nonetheless,

to build intuition, we recall the simple example of decoherence of an n-maximally entangled state under independent Markovian bath: $\chi_n(\tau) = n\Gamma\tau$, where Γ is the decoherence rate for a single qubit [54]. Then we have $\frac{e^{-\chi_n(\tau)}}{e^{-\chi_1(\tau)}} = e^{-(n-1)\Gamma\tau} \leq 1$: the n-maximally entangled sensor decoheres exponentially faster, working against the (polynomial) n-fold enhancement in sensitivity. Or put another way, recalling that $\tau \equiv \omega_{ac}^{-1}$, this exponential decay in τ will limit the 'working range' or bandwith of the frequencies ω_{ac} of the AC fields the entangled sensor can sense (with quantum advantage).

To summarize, the (quantum) gain depends on four factors:

$$g = n \left(\frac{\alpha_n}{\alpha_1}\right) \left(\frac{e^{-\chi_n(\tau)}}{e^{-\chi_1(\tau)}}\right) \sqrt{\frac{\tau + t_1}{\tau + t_e}} \tag{4.1}$$

whereby save the $n > 1$ entanglement-enhancement, the relative control infidelity $\frac{\alpha_n}{\alpha_1} < 1$, the faster decoherence $\frac{e^{-\chi_n(\tau)}}{e^{-\chi_1(\tau)}} < 1$, and increased idle time $\sqrt{\frac{\tau+t_1}{\tau+t_e}} < 1$ (not spent on task of interest: sensing) associated with n-maximally entangled sensor will favor $g < 1$.

4.0.2 Entanglement-enhanced Sensing

Here we report our first experimental characterization of our two sensors in order to extract the (quantum) gain $g(\tau)$ over the working range τ. As for notation regarding the two sensors of interest, for the rest of the section we may refer to the $n = 1$-qubit sensor (i.e., the NV) as a 'classical' sensor and the $n = 2$-qubit sensor (i.e., the maximally entangled Bell state of NV and X) as the 'entangled' or 'quantum' sensor

The quantum circuit of the entanglement-enhanced sensing protocol is shown in Fig. 4-1. The ϕ-block shown in Fig. 4-1a is accounts for the sensing task of interest (here, spin echo AC magnetometry) of duration $\tau \equiv \omega_{ac}^{-1}$. Recalling Eq. 1.4, the sensing signal yields phase $\phi \propto nb\tau$, where b is the parameter of interest, and n is the gain in sensing rate due to entanglement. However, in order to perform the sensing task of interest, the rest of the protocol is required (in order) to initialize the NV and X spins [50, 68, 72], then entangle to a maximally-entangled Bell state [22, 104], then

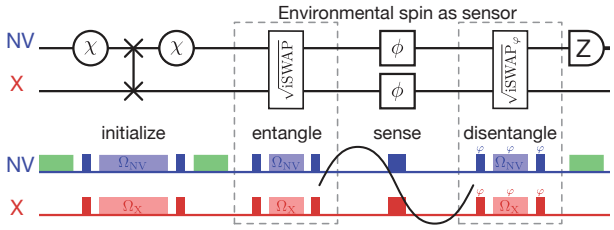

Figure 4-1: **Entanglement-enhanced sensing protocol.** Quantum circuit (top) and specific pulse sequence (bottom) of the sensing protocol for the $n = 2$-qubit system composed of a single NV and one nearby X electronic spin. *Adapted from [22].*

disentangle to readout the phase ϕ. This 'idle' time t_{idle}^{qm} or any time not used for the task of interest can be significant (with respect to τ) and hence in achieving quantum advantage.

For our system, in the limit of fast single-qubit driving (i.e., sufficiently large Rabi Ω_0), the $n = 1$ sensor (NV) requires $t_{idle}^{cl} = 2L$, where $L \sim 2.6\mu$s is the laser pulse length to initialize and read the NV state. Whereas the $n = 2$ sensor requires

$$\begin{aligned} t_{idle}^{qm} &= t_{idle}^{cl} + t_{init} + t_{entangle} + t_{disentangle}, \\ &= t_{idle}^{cl} + ((2d)^{-1} + L) + (4d)^{-1} + (4d)^{-1}, \\ &= t_{idle}^{cl} + L + d^{-1}, \end{aligned} \tag{4.2}$$

where $d \sim 60$ kHz is the coupling strength between NV and X. Given that d determines the length of (dis)entangling gates and SWAP gates used for initialization, the t_{idle}^{qm} is (almost) inversely proportional to d and hence significantly benefits from stronger coupling.

Having described the sensing protocol, we experimentally execute the protocol to perform AC magnetometry with both $n = 1$ and $n = 2$ sensors. For experimental simplicity, all $n = 2$ protocols are performed by addressing only 1 of 2 hyperfine transitions of the X electronic spin (thereby reducing signal by half, whose effect will be discussed below).

A typical AC magnetometry experiment, sweeping b at fixed τ, is shown in Fig. 4-2. By fitting to the expected sinusoidal signal (Eq. 1.4), we directly verify $n = 2$-fold

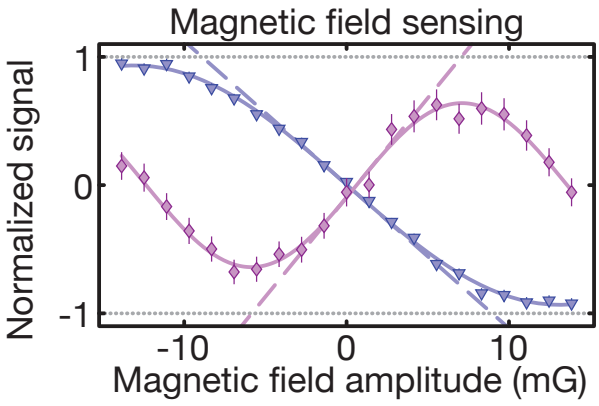

Figure 4-2: **Typical AC magnetometry experiment.** The AC magnetometry experiment— sweeping the amplitude b of externally applied B-field $b(t) = b\sin(\omega_{ac}t)$, with the spin echo sequence applied to the sensor qubit(s)—is shown. Fitting both sensor signals $S_{n=1}(b)$ for NV (blue data points) and $S_{n=2}(b)$ for NV-X entangled (purple data points) to the expected sinusoidal (lines) directly verifies (full) $n = 2$-enhancement. Furthermore, by extracting the slope $\left|\frac{dS}{db}\right|$ (dashed lines) and the uncertainty σ_S (errorbar) at the optimal working point ($b = 0$), we directly extract the (single-shot) sensitivity $\eta_{N=1}$ of each sensor, and in turn the (single-shot) gain $g_{N=1}$. *Adapted from [22].*

increase in sensing rate for the entangled sensor.

Now to extract gain g, we (only) need to measure the single-shot sensitivity $\eta_{N=1}$ of each sensor, as seen by:

$$
\begin{aligned}
g &= g_{N=1}\sqrt{\frac{\tau + t_1}{\tau + t_e}}, \\
g_{N=1} &= \frac{\eta^{cl}_{N=1}}{\eta^{qm}_{N=1}}, \\
\eta_{N=1} &= \frac{\sigma_S}{\left|\frac{dS}{db}\right|_{max}}.
\end{aligned}
$$

Here, $\left|\frac{dS}{db}\right|_{max}$ and σ_S are exactly the slope and uncertainty, respectively, at the optimal working point of the sensor $b = 0$ (Fig. 4-2). Repeating the AC magnetometry experiment at $\tau = 2, 10, 20\mu$s, we report the gain $g(\tau)$ in Fig. 4-3, which we will discuss shortly.

In order to more completely characterize our sensors (in addition to the (direct) AC magnetometry experiments at $\tau = 2, 10, 20\mu$s), we further predict the sensitivity

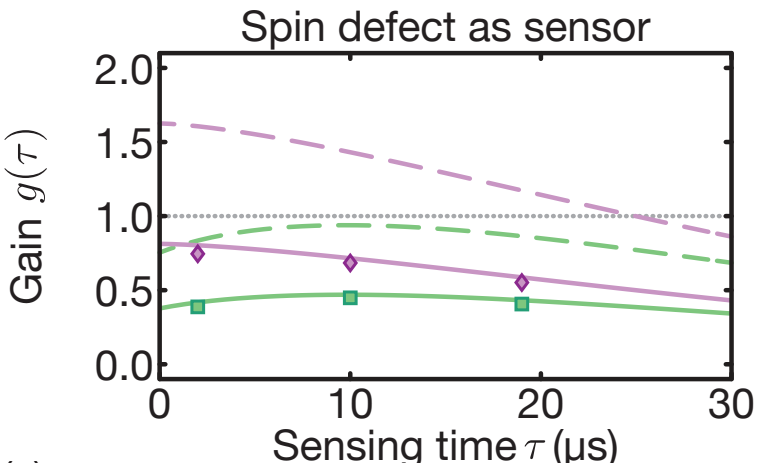

Figure 4-3: **Gain in sensitivity: Entanglement-enhanced.** The (quantum) gain $g \equiv \eta_1/\eta_e$ in the sensitivity is shown across the working range τ of the two sensors, where $g > 1$ means quantum advatange. *Adapted from [22].*

over the entire working range of τ, via:

$$\begin{aligned} g &\equiv \frac{\eta^1}{\eta^e}, \\ &= n\left(\frac{\alpha_n}{\alpha_1}\right)\left(\frac{e^{-\chi_n(\tau)}}{e^{-\chi_1(\tau)}}\right)\sqrt{\frac{\tau+t_1}{\tau+t_e}} \end{aligned}$$

In other words, the only missing information is $\alpha_n(\tau) \equiv \alpha_n e^{-\chi_n(\tau)}$, which is the n-qubit decoherence through the sensing protocol (i.e., spin echo) of length τ. Therefore, from the spin-echo experiment in Fig. 4-4, we can extract both parameters.

First, we find the relative signal contrast of:

$$\frac{\alpha_n}{\alpha_1} = \frac{0.78(6)}{0.96(3)} \sim 0.81$$

As expected, the quantum circuit (to prepare the sensor state) for $n = 1$ qubit is nearly perfect, yielding single-qubit coherence $\alpha_1 = 0.96(3)$. In contrast, the quantum circuit to prepare $n = 2$-maximally entangled state only achieves $\alpha_{n=2} = 0.78(6)$. Given that the $n = 2$ quantum circuit consists of 4 two-qubit (dis)entangling gates between NV and X spins (Fig. 4-1), we can crudely approximate that each two-qubit entangling gate has a 'fidelity' of $F_{entangle} \sim 0.78^{1/4} \sim 0.94$.

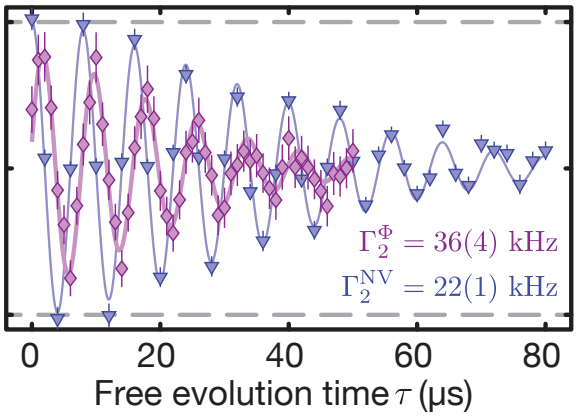

Figure 4-4: **Decoherence under spin echo of $n = 2$ entangled sensor vs. $n = 1$ single-qubit sensor.** The $n = 2$-entangled sensor (of NV and X spins) under spin echo (purple data points) decoheres exponentially at approximately twice the rate than that of the $n = 1$-qubit sensor (NV). *Adapted from [22].*

Second, we also find as expected an exponentially faster decoherence for the entangled sensor. More specifically, fitting each signal to $S_n(\tau) \equiv e^{-(\Gamma\tau)^p}$, we find $p \sim 1.6$ for both sensors and the decoherence rates:

$$\Gamma_{n=2} \sim 2\Gamma_{n=1}$$

We can now predict the gain $g(\tau)$ over all working range τ, which is plotted in Fig. 4-3 (solid lines): and the predicted sensitivities reproduce the direct AC magnetometry measurements at $\tau = 2, 10, 20\mu$s.

We now discuss the results in Fig. 4-3.

For simplicity, first consider the single-shot gain $g_{N=1}(\tau)$ (purple), which does not consider time $T = N(\tau + t_{idle})$ as a resource. Recall that the data points (and solid line) are from experiments, during which we addressed only one half of the available nuclear population of X. Therefore, if we could remove the nuclear spin degree of freedom of X (e.g., via simultaneous driving of both hyperfine transitions or via polarizing the nuclear spin), then in such a 'best' case scenario we could achieve the (purple) dashed lines (multiplied by a factor of 2). Then we find $g_{N=1}(\tau) > 1$ for a large range of τ.

However, we now take time T into account by considering the t_{idle} of each sensor.

This results in the true gain $g(\tau) = g_{N=1}(\tau)\sqrt{\frac{\tau+t_1}{\tau+t_e}}$ (green). Similarly, while the data points (and solid line) reflect only half-driven nuclear population, we can project to the best case scenario (dashed line) by multiplying by 2 to remove the nuclear spin degree of freedom. However, even in such a case, we find $g(\tau) < 1$ for the entire working range τ.

In other words, given our system parameters (d, Γ_n) and control parameters $(F_{entangle})$, entanglement (alone) is insufficient to allow quantum advantage $g > 1$.

Therefore, in order to improve upon the entanglement-enhancement allowed for $n > 1$ systems, we further demonstrate the use of the second qubit as a memory bit.

4.0.3 Entanglement- & Memory-enhanced Sensing

Given entanglement alone, recall that g upper-bounded by n:

$$\begin{aligned} g &= n\left(\frac{\alpha_n}{\alpha_1}\right)\left(\frac{e^{-\chi_n(\tau)}}{e^{-\chi_1(\tau)}}\right)\sqrt{\frac{\tau+t_1}{\tau+t_e}} \\ &\leq g_{max} = n, \end{aligned}$$

where the equality would be achieved given instantaneous two-qubit gates that are of the same fidelity as single-qubit gates and the same rate of decoherence for the $n > 1$-maximally entangled sensor—which in principle is not possible. But short of achieving $g = 2$, it was in practice to realize even $g > 1$ due to the 'costs' of entanglement.

Therefore, in this section, we demonstrate an independent method to extend the upper-bound:

$$g_{max} = n \quad \rightarrow \quad g'_{max} = n\mathrm{SNR}(M)$$

where $\mathrm{SNR}(M \geq 1) \leq \sqrt{M}$ is the resulting SNR after M number of measurements made on the $n = 2$ system.

We show that this can be achieved by a modified sensing (+ memory) protocol as in Fig. 4-5. More specifically, after the sensing and disentangling gate, the sensed

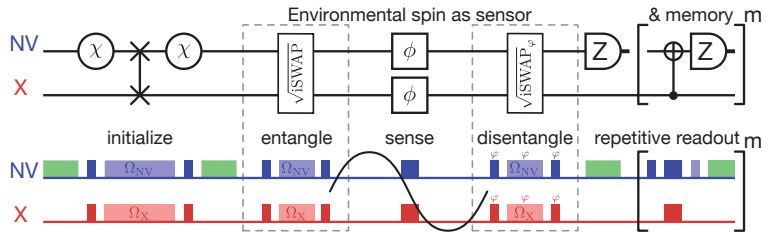

Figure 4-5: **Environment-assisted sensing: Entanglement- and memory-enhanced.** Quantum circuit (a.) and specific pulse sequence (b.) of the modified sensing protocol for the $n = 2$-qubit system composed of a single NV and one nearby X electronic spin. It include the optional 'repetitive readout' block [57], iterated m times. More specifically, given the sensed information ϕ is stored in the X spin population after the disentangling gate, there is the option to further utilize the X as a (classical) memory bit, from which additional (classical) SNR gain of $\sqrt{m}$ may be possible *Adapted from [22].*

information ϕ is stored in both the NV and the X spin population. Then, whereas the first ($M = 1$) measurement via green laser re-initializes the NV, ϕ is still stored in the X spin population. This allows the possibility to further utilize the X spin as a (classical) memory bit, from which one could make $M - 1$ more measurements [57].

Then, in the ideal case—of zero depolarization of X under green illumination as well as a perfect two-qubit entangling gate to readout X population—it would be possible to infinitely benefit in SNR by $\sqrt{M}$ with increasing M. But realistically, there is partial depolarization of X under green illumination as well as imperfect two-qubit gates, and hence a limit to maximum achievable $1 \leq \text{SNR} < \sqrt{M}$.

To first demonstrate we can extend the upper-bound $g_{max} = n \rightarrow nSNR(M)$, we re-perform the AC magnetometry experiment under the modified protocol with repeated readout on the X spin. Indeed, on top of the $n = 2$-fold entanglement-enhancement (seen from the oscillation rate), we demonstrate that one could further gain SNR $< \sqrt{M}$ as seen in Fig. 4-6. More specifically, we observe $\text{SNR}(m = 6) \sim 2 < \sqrt{6} \sim 2.4$.

Thus under the 'hardware-efficient' protocol—where the second qubit is re-purposed

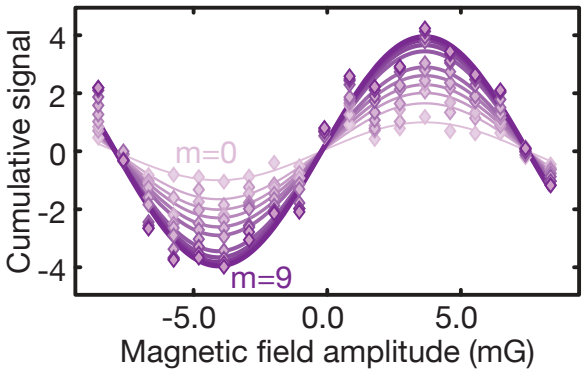

Figure 4-6: **Repeated readout of optically dark electronic spin X.** Repeating the AC magnetometry experiment under the modified procotol—with additional $(m-1) = 8$ queries made to the X spin as a classical memoery bit. We observe the (ideal) SNR scaling $\sqrt{m}$ up to a few m; however, given imperfect two-qubit control and non-zero X depolarization under laser illumination, the maximum SNR saturates by several m. *Adapted from [22].*

as a memory bit after entangled sensing—we have the (modified) gain:

$$g' = g'_{N=1}\sqrt{\frac{\tau + t_1}{\tau + t'_e}},$$
$$g'_{N=1} = g_{N=1}\mathrm{SNR}(M),$$
$$t'_e = t_e + (M-1)t_{entangle},$$

where $t_{entangle} = (4d)^{-1}$. As seen from the last two equations, the enhancement by $\frac{g'_{N=1}}{g_{N=1}} = \mathrm{SNR}(M)$—like entanglement—is not free but has a cost: $t'_e - t_e = (M-1)(4d)^{-1}$. Given that (approximately) $t_e \propto d^{-1}$, in the limit of strong coupling, $(d\tau) \gg 1$, one benefits not only in entanglement-only sensing, but also further with repeated readout of X.

Now we report the final result of gain g' as a function of increasing number of repeated measurements $m = M - 1$ in Fig. 4-7 at $\tau = 20\mu$s. As before, the (purple) green color refers to (single-shot) gain; the filled (empty) data points are the experimentally measured (projected, multiplied by 2).

First, we observe that the gain g monotonically increases with m until $m = 6$—

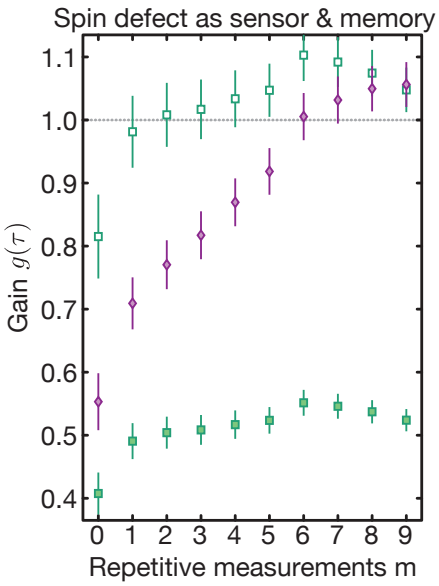

Figure 4-7: **Entanglement- and Memory-enhanced Gain in Sensitivity for $n = 2$-qubit Sensor.** *Adapted from [22].*

due to sufficiently increasing SNR(m). Perhaps more importantly, by $m = 2$, it is possible to achieve quantum advantage $g' > 1$. Recall from above that, given our system parameters (d, Γ) and control fidelity ($F_{entangle}$), entanglement alone was insufficient to achieve quantum advantage at any τ over the entire working range. But by extending the possible gain via re-purposing the second qubit as a memory, it is possible to achieve quantum advantage $g' > 1$. Finally, we observe that after the monotonic rise up to $m = 6$, the gain g starts to decrease with m, not only due to saturating SNR(m) but also with increasing time cost.

Finally, to generalize beyond our specific $n = 2$ spin system, we map the possible gain g, g' as a function of system parameters (d, Γ) around our own. We observe the region of $g > 1$ (dark green) increases with increasing d (equivalently decreasing idle time t_{idle}^{qm} spent to generate and measure entangled states); and furthermore the region of $g' > 1$ (light green) due to faster memory query time. On the other hand, the y-axis shows the relative decoherence rate of the two qubits, motivated by the fact that (even) for two spatially proximal qubits their decoherence is not identical (which will be further elucidated in the next Chapter). In such a case, depending on the specific sensing task, the central spin may benefit more from entangling with a

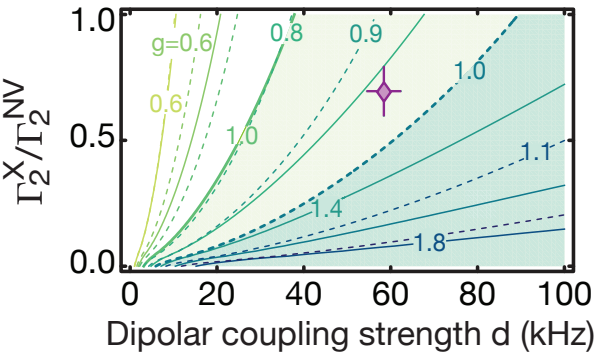

Figure 4-8: **Projected Gain of $n = 2$ Sensor.** We show numerically the projected gain in sensitivity—given observed control fidelity and removed nuclear spin-1/2 degree of freedom—as a function of the $n = 2$ system parameters: coupling strength d and relative decoherence rate Γ. Entanglement-enhanced (only) gain $g > 1$ is shown in dark green region; entanglement- and memory-enhanced $g' > 1$ is the (larger) light green region. Purple diamond shows our particular system parameters: while with entanglement alone $g < 1$, with entanglement and repetitive readout $g' > 1$. Finally, note the (strong) dependence of g, g' on the interaction strength d, which determines the rate of entangling (and initialization) to reduce idle time of the $n > 1$-entangled sensor. On the other hand, the relative decoherence of each qubit is motivated by the fact that even for spatially proximal qubits, the effective bath seen by each qubit may not be identical (to yield the same T_2 or decay profile). In this case, the central qubit may further benefit from entangling with a nearby spin of longer coherence. *Adapted from [22].*

nearby spin of longer coherence time.

Conclusion In this Chapter, we demonstrate environment-assisted sensing with a two-qubit electronic spin register to achieve quantum advantage in sensing of classical fields. While entanglement alone may be insufficient to achieve practical quantum advantage at realistic system parameters (Fig. 4-8), we find the additional enhancement via a repetitive readout scheme can significantly increase the area of quantum advantage. Therefore, depending on the system parameters of the electronic spin register, environment-assisted sensing can significantly enhance the sensitivity of sensing external fields at the nanoscale.

Chapter 5

Conclusion and Outlook

In this thesis, we set our goal to develop small-scale quantum information processors based on electronic spins in diamond. In contrast to the more developed nuclear spin register around a central NV, an electronic spin register is expected to enable new applications thanks to its stronger coupling between spins and to external fields, e.g., as a platform to demonstrate enhanced sensing, develop novel characterization tools for general quantum devices, and prototype a scalable architecture for quantum computation. In this thesis, we have taken three critical steps towards our goal to demonstrate the potential advantages of an electronic spin register. Here, we review our main results and their significance, and provide an outlook on potential future steps to build upon the results and developed methods.

As the first step, we developed a general method to systematically scale up a system of electronic spins, starting with a central NV center in diamond, by identifying the Hamiltonian of unknown spins near the NV. As knowledge of the system Hamiltonian is required for good coherent control over the system, this is the first step we take to develop a register of electronic spins. Utilizing this method, we characterized the Hamiltonian of two unknown electron-nuclear spin defects interacting with the NV – which have not yet been reported in previous literature based on spectroscopy of ensemble spins. This result demonstrates that our method to characterize electron-nuclear spin defects at the single-molecule level can enable further exploration of electronic spin clusters in various solid-state systems. More specifically, it not only

enables identification of various possible spin complexes in the host crystal with further characterization of the nuclear spin species, but also simultaneously realizes a controllable quantum register of electronic spins.

Given the controllable quantum register of electronic spins, we characterized this device with respect to two important aspects: entanglement and decoherence.

First, given that entanglement is critical for many quantum information tasks, an accurate characterization of the entanglement generated by a quantum device is desired. To this end, we developed a method to detect entanglement that is more robust in the presence of local unitary control errors. More specifically, in comparison to the conventional entanglement witness based on state fidelity, our proposed metric (the subspace witness) is insensitive to any combination of single-qubit phase errors accrued during the state-preparation-and-measurement of the target entangled state. This robustness comes however at the cost of additional measurements, which however scales favorably for important classes of entangled states. Not only does this metric yield a more accurate characterization of the entanglement generated by the device, it also facilitates the estimation of a lower bound for entanglement via the metric called GME concurrence.

Second, given that the lifetime of quantum devices is limited by decoherence, a practical (classical) and predictive noise model for the device is desired. Therefore, as a first step to characterize the noise affecting a multi-qubit device, we demonstrated a protocol to build a self-consistent classical noise model for individual qubits. Applying this protocol to two spatially nearby qubits, we reported two results. For the NV qubit – sufficiently isolated/distinguishable from its bath – it is possible to build a classical noise model that is self-consistent with a varied set of dynamics (namely, Ramsey, Echo, and CPMG experiments). However, for the nearby X qubit, this is not possible, possibly due to a more complex and quantum bath for X. More specifically, we find evidence for the presence of near-resonant spins interacting with X – such that driving X at sufficient Rabi power also partially drives the bath of X – giving rise to a noise model that must be changed as a function of (ideally bath-independent) Rabi power. The two results offer two potential outlooks. First, given qubits for which a self-

consistent noise model is possible – suggesting a qubit well isolated from the bath – their noise model can be used to simultaneously characterize the bath and as well develop more robust quantum gates and circuits. Second, given qubits for which a self-consistent noise model is not possible – this may suggest a more complex and sufficiently quantum bath that could be further explored. In the case of our electronic spin X, the presence of near-resonant, interacting spins may offer a way to further scale up our register of electronic spins upon further characterization.

Finally, given our electronic spin register, we demonstrated a quantum information task in quantum sensing. More specifically, we demonstrated environment-assisted sensing, utilizing the NV center and one additional electronic spin from the environment, to achieve practical quantum advantage. We first verified entanglement-enhanced sensing with the two-qubit entangled sensor – but find the sensitivity gain via entanglement is insufficient to overcome the necessary costs of entanglement that degrade sensitivity. Therefore, to take one step further towards quantum advantage, we enhanced the sensitivity by utilizing the additional electronic spin as a classical memory register (after entangled sensing). We find that, as a function of electronic spin system parameters, the sensitivity enhancement via both entanglement and memory significantly increases the area of quantum advantage.

The results and general methods developed in this thesis pave the way towards building multi-qubit quantum information processors based on a register of electronic spins. Furthermore, going beyond n=2 spins, more interesting applications can be explored, including but not limited to (hardware-efficient) quantum error correction, error corrected sensing, three-qubit entangling gates, generation of genuine multipartite entangled states, and more. Finally, as a more immediate outlook given our particular system, it may be possible to further scale up the size of the quantum register, building upon the discovery of not only resolved nuclear spin(s) nearby the NV but also possibly a group of coherently coupled electronic spins around X. This latter step would allow further scaling of the electronic spin register beyond the coherence time of the central spin.

Bibliography

[1] Dorit Aharonov and Michael Ben-Or. Fault-Tolerant Quantum Computation with Constant Error Rate. *SIAM Journal on Computing*, 38(4):1207–1282, January 2008.

[2] Gonzalo A. Álvarez and Dieter Suter. Measuring the Spectrum of Colored Noise by Dynamical Decoupling. *Physical Review Letters*, 107(23):230501, November 2011.

[3] M. K. Atumi, J. P. Goss, P. R. Briddon, F. E. Shrif, and M. J. Rayson. Hyperfine interactions at nitrogen interstitial defects in diamond. *Journal of Physics: Condensed Matter*, 25(6):065802, January 2013.

[4] B. I. Bantysh, D. V. Fastovets, and Yu I. Bogdanov. High-fidelity quantum tomography with imperfect measurements. In *International Conference on Micro- and Nano-Electronics 2018*, volume 11022, page 110222N. International Society for Optics and Photonics, March 2019.

[5] Erik Bauch, Connor A. Hart, Jennifer M. Schloss, Matthew J. Turner, John F. Barry, Pauli Kehayias, Swati Singh, and Ronald L. Walsworth. Ultralong Dephasing Times in Solid-State Spin Ensembles via Quantum Control. *Physical Review X*, 8(3):031025, July 2018.

[6] Erik Bauch, Swati Singh, Junghyun Lee, Connor A. Hart, Jennifer M. Schloss, Matthew J. Turner, John F. Barry, Linh M. Pham, Nir Bar-Gill, Susanne F. Yelin, and Ronald L. Walsworth. Decoherence of ensembles of nitrogen-vacancy centers in diamond. *Physical Review B*, 102(13):134210, October 2020.

[7] J. S. Bell. On the Einstein Podolsky Rosen paradox. *Physics Physique Fizika*, 1(3):195–200, November 1964.

[8] Charles H. Bennett, David P. DiVincenzo, John A. Smolin, and William K. Wootters. Mixed-state entanglement and quantum error correction. *Physical Review A*, 54(5):3824–3851, November 1996.

[9] Marcel Bergmann and Otfried Gühne. Entanglement criteria for Dicke states. *Journal of Physics A: Mathematical and Theoretical*, 46(38):385304, September 2013.

[10] M. Block, B. Kobrin, A. Jarmola, S. Hsieh, C. Zu, N.L. Figueroa, V.M. Acosta, J. Minguzzi, J.R. Maze, D. Budker, and N.Y. Yao. Optically Enhanced Electric Field Sensing Using Nitrogen-Vacancy Ensembles. *Physical Review Applied*, 16(2):024024, August 2021.

[11] Yu I. Bogdanov, B. I. Bantysh, N. A. Bogdanova, A. B. Kvasnyy, and V. F. Lukichev. Quantum states tomography with noisy measurement channels. In *International Conference on Micro- and Nano-Electronics 2016*, volume 10224, page 102242O. International Society for Optics and Photonics, December 2016.

[12] J. J . Bollinger, Wayne M. Itano, D. J. Wineland, and D. J. Heinzen. Optimal frequency measurements with maximally correlated states. *Physical Review A*, 54(6):R4649–R4652, December 1996.

[13] Mohamed Bourennane, Manfred Eibl, Christian Kurtsiefer, Sascha Gaertner, Harald Weinfurter, Otfried Gühne, Philipp Hyllus, Dagmar Bruß, Maciej Lewenstein, and Anna Sanpera. Experimental Detection of Multipartite Entanglement using Witness Operators. *Physical Review Letters*, 92(8):087902, February 2004.

[14] C. E. Bradley, J. Randall, M. H. Abobeih, R. C. Berrevoets, M. J. Degen, M. A. Bakker, M. Markham, D. J. Twitchen, and T. H. Taminiau. A Ten-Qubit Solid-State Spin Register with Quantum Memory up to One Minute. *Physical Review X*, 9(3):031045, September 2019.

[15] Jonas Bylander, Simon Gustavsson, Fei Yan, Fumiki Yoshihara, Khalil Harrabi, George Fitch, David G. Cory, Yasunobu Nakamura, Jaw-Shen Tsai, and William D. Oliver. Noise spectroscopy through dynamical decoupling with a superconducting flux qubit. *Nature Physics*, 7(7):565–570, July 2011.

[16] Jianming Cai, Fedor Jelezko, and Martin B. Plenio. Hybrid sensors based on colour centres in diamond and piezoactive layers. *Nature Communications*, 5(1):4065, September 2014.

[17] P. Cappellaro, J. S. Hodges, T. F. Havel, and D. G. Cory. Principles of control for decoherence-free subsystems. *The Journal of Chemical Physics*, 125(4):044514, July 2006.

[18] P. Cappellaro, J. S. Hodges, T. F. Havel, and D. G. Cory. Control of qubits encoded in decoherence-free subspaces. *Laser Physics*, 17(4):545–551, April 2007.

[19] John F. Clauser, Michael A. Horne, Abner Shimony, and Richard A. Holt. Proposed Experiment to Test Local Hidden-Variable Theories. *Physical Review Letters*, 23(15):880–884, October 1969.

[20] A. Cooper, E. Magesan, H. N. Yum, and P. Cappellaro. Time-resolved magnetic sensing with electronic spins in diamond. *Nature Communications*, 5(1):3141, January 2014.

[21] Alexandre Cooper, Won Kyu Calvin Sun, Jean-Christophe Jaskula, and Paola Cappellaro. Environment-assisted quantum-enhanced sensing with electronic spins in diamond. *arXiv:1811.09572 [quant-ph]*, November 2018.

[22] Alexandre Cooper, Won Kyu Calvin Sun, Jean-Christophe Jaskula, and Paola Cappellaro. Environment-assisted Quantum-enhanced Sensing with Electronic Spins in Diamond. *Physical Review Applied*, 12(4):044047, October 2019.

[23] Alexandre Cooper, Won Kyu Calvin Sun, Jean-Christophe Jaskula, and Paola Cappellaro. Identification and Control of Electron-Nuclear Spin Defects in Diamond. *Physical Review Letters*, 124(8):083602, February 2020.

[24] J. Cramer, N. Kalb, M. A. Rol, B. Hensen, M. S. Blok, M. Markham, D. J. Twitchen, R. Hanson, and T. H. Taminiau. Repeated quantum error correction on a continuously encoded qubit by real-time feedback. *Nature Communications*, 7(1):11526, May 2016.

[25] Daniel Crow and Robert Joynt. Classical simulation of quantum dephasing and depolarizing noise. *Physical Review A*, 89(4):042123, April 2014.

[26] Łukasz Cywiński, Roman M. Lutchyn, Cody P. Nave, and S. Das Sarma. How to enhance dephasing time in superconducting qubits. *Physical Review B*, 77(17):174509, May 2008.

[27] G. de Lange, D. Ristè, V. V. Dobrovitski, and R. Hanson. Single-Spin Magnetometry with Multipulse Sensing Sequences. *Physical Review Letters*, 106(8):080802, February 2011.

[28] G. de Lange, Z. H. Wang, D. Ristè, V. V. Dobrovitski, and R. Hanson. Universal Dynamical Decoupling of a Single Solid-State Spin from a Spin Bath. *Science*, 330(6000):60–63, October 2010.

[29] Gijs de Lange, Toeno van der Sar, Machiel Blok, Zhi-Hui Wang, Viatcheslav Dobrovitski, and Ronald Hanson. Controlling the quantum dynamics of a mesoscopic spin bath in diamond. *Scientific Reports*, 2(1):382, April 2012.

[30] Rogerio de Sousa. Electron Spin as a Spectrometer of Nuclear-Spin Noise and Other Fluctuations. In Marco Fanciulli, editor, *Electron Spin Resonance and Related Phenomena in Low-Dimensional Structures*, Topics in Applied Physics, pages 183–220. Springer, Berlin, Heidelberg, 2009.

[31] C. L. Degen, F. Reinhard, and P. Cappellaro. Quantum sensing. *Reviews of Modern Physics*, 89(3):035002, July 2017.

[32] M. J. Degen, S. J. H. Loenen, H. P. Bartling, C. E. Bradley, A. L. Meinsma, M. Markham, D. J. Twitchen, and T. H. Taminiau. Entanglement of dark electron-nuclear spin defects in diamond. *Nature Communications*, 12(1):3470, June 2021.

[33] David P. DiVincenzo. The Physical Implementation of Quantum Computation. *Fortschritte der Physik*, 48(9-11):771–783, 2000.

[34] V. V. Dobrovitski, A. E. Feiguin, D. D. Awschalom, and R. Hanson. Decoherence dynamics of a single spin versus spin ensemble. *Physical Review B*, 77(24):245212, June 2008.

[35] F. Dolde, H. Fedder, M. W. Doherty, T. Nöbauer, F. Rempp, G. Balasubramanian, T. Wolf, F. Reinhard, L. C. L. Hollenberg, F. Jelezko, and J. Wrachtrup. Electric-field sensing using single diamond spins. *Nature Physics*, 7(6):459–463, June 2011.

[36] F. Dolde, I. Jakobi, B. Naydenov, N. Zhao, S. Pezzagna, C. Trautmann, J. Meijer, P. Neumann, F. Jelezko, and J. Wrachtrup. Room-temperature entanglement between single defect spins in diamond. *Nature Physics*, 9(3):139–143, March 2013.

[37] S. Felton, A. M. Edmonds, M. E. Newton, P. M. Martineau, D. Fisher, D. J. Twitchen, and J. M. Baker. Hyperfine interaction in the ground state of the negatively charged nitrogen vacancy center in diamond. *Physical Review B*, 79(7):075203, February 2009.

[38] Evan M. Fortunato, Lorenza Viola, Jonathan Hodges, Grum Teklemariam, and David G. Cory. Implementation of universal control on a decoherence-free qubit. *New Journal of Physics*, 4:5–5, February 2002.

[39] Torsten Gaebel, Michael Domhan, Iulian Popa, Christoffer Wittmann, Philipp Neumann, Fedor Jelezko, James R. Rabeau, Nikolas Stavrias, Andrew D. Greentree, Steven Prawer, Jan Meijer, Jason Twamley, Philip R. Hemmer, and Jörg Wrachtrup. Room-temperature coherent coupling of single spins in diamond. *Nature Physics*, 2(6):408–413, June 2006.

[40] Sevag Gharibian. Strong NP-Hardness of the Quantum Separability Problem. *arXiv:0810.4507 [quant-ph]*, October 2008.

[41] G. Goldstein, P. Cappellaro, J. R. Maze, J. S. Hodges, L. Jiang, A. S. Sørensen, and M. D. Lukin. Environment-Assisted Precision Measurement. *Physical Review Letters*, 106(14):140502, April 2011.

[42] B. L. Green, M. W. Dale, M. E. Newton, and D. Fisher. Electron paramagnetic resonance of the ${\mathrm{N}}_{2}{\mathrm{V}}\hat{}\ensuremath{-}$ defect in $\hat{15}\mathrm{N}$-doped synthetic diamond. *Physical Review B*, 92(16):165204, October 2015.

[43] M. S. Grinolds, M. Warner, K. De Greve, Y. Dovzhenko, L. Thiel, R. L. Walsworth, S. Hong, P. Maletinsky, and A. Yacoby. Subnanometre resolution in three-dimensional magnetic resonance imaging of individual dark spins. *Nature Nanotechnology*, 9(4):279–284, April 2014.

[44] Otfried Gühne and Michael Seevinck. Separability criteria for genuine multiparticle entanglement. *New Journal of Physics*, 12(5):053002, May 2010.

[45] Otfried Gühne and Géza Tóth. Entanglement detection. *Physics Reports*, 474(1):1–75, April 2009.

[46] Leonid Gurvits. Classical Deterministic Complexity of Edmonds' Problem and Quantum Entanglement. In *Proceedings of the Thirty-Fifth Annual ACM Symposium on Theory of Computing*, STOC '03, pages 10–19, New York, NY, USA, 2003. ACM.

[47] E. L. Hahn. Spin Echoes. *Physical Review*, 80(4):580–594, November 1950.

[48] R. Hanson, V. V. Dobrovitski, A. E. Feiguin, O. Gywat, and D. D. Awschalom. Coherent Dynamics of a Single Spin Interacting with an Adjustable Spin Bath. *Science*, 320(5874):352–355, April 2008.

[49] R. Hanson, F. M. Mendoza, R. J. Epstein, and D. D. Awschalom. Polarization and Readout of Coupled Single Spins in Diamond. *Physical Review Letters*, 97(8):087601, August 2006.

[50] S. R. Hartmann and E. L. Hahn. Nuclear Double Resonance in the Rotating Frame. *Physical Review*, 128(5):2042–2053, December 1962.

[51] S. Hernández-Gómez, F. Poggiali, P. Cappellaro, and N. Fabbri. Noise spectroscopy of a quantum-classical environment with a diamond qubit. *Physical Review B*, 98(21):214307, December 2018.

[52] Masashi Hirose and Paola Cappellaro. Coherent feedback control of a single qubit in diamond. *Nature*, 532(7597):77–80, April 2016.

[53] Michał Horodecki, Paweł Horodecki, and Ryszard Horodecki. Separability of mixed states: Necessary and sufficient conditions. *Physics Letters A*, 223(1):1–8, November 1996.

[54] S. F. Huelga, C. Macchiavello, T. Pellizzari, A. K. Ekert, M. B. Plenio, and J. I. Cirac. Improvement of Frequency Standards with Quantum Entanglement. *Physical Review Letters*, 79(20):3865–3868, November 1997.

[55] Lawrence M. Ioannou. Computational complexity of the quantum separability problem. *arXiv:quant-ph/0603199*, March 2006.

[56] J. Isoya, H. Kanda, Y. Uchida, S. C. Lawson, S. Yamasaki, H. Itoh, and Y. Morita. EPR identification of the negatively charged vacancy in diamond. *Physical Review B*, 45(3):1436–1439, January 1992.

[57] L. Jiang, J. S. Hodges, J. R. Maze, P. Maurer, J. M. Taylor, D. G. Cory, P. R. Hemmer, R. L. Walsworth, A. Yacoby, A. S. Zibrov, and M. D. Lukin. Repetitive Readout of a Single Electronic Spin via Quantum Logic with Nuclear Spin Ancillae. *Science*, 326(5950):267–272, October 2009.

[58] N. Kalb, A. A. Reiserer, P. C. Humphreys, J. J. W. Bakermans, S. J. Kamerling, N. H. Nickerson, S. C. Benjamin, D. J. Twitchen, M. Markham, and R. Hanson. Entanglement distillation between solid-state quantum network nodes. *Science*, 356(6341):928–932, June 2017.

[59] A. Yu. Kitaev. Fault-tolerant quantum computation by anyons. *Annals of Physics*, 303(1):2–30, January 2003.

[60] J. R. Klauder and P. W. Anderson. Spectral Diffusion Decay in Spin Resonance Experiments. *Physical Review*, 125(3):912–932, February 1962.

[61] Sebastian Knauer, John P. Hadden, and John G. Rarity. In-situ measurements of fabrication induced strain in diamond photonic-structures using intrinsic colour centres. *npj Quantum Information*, 6(1):1–6, June 2020.

[62] Emanuel Knill, Raymond Laflamme, and Wojciech H. Zurek. Resilient Quantum Computation. *Science*, 279(5349):342–345, January 1998.

[63] Helena S. Knowles, Dhiren M. Kara, and Mete Atatüre. Demonstration of a Coherent Electronic Spin Cluster in Diamond. *Physical Review Letters*, 117(10):100802, September 2016.

[64] Ryogo Kubo. Generalized Cumulant Expansion Method. *Journal of the Physical Society of Japan*, 17(7):1100–1120, July 1962.

[65] G. Kucsko, P. C. Maurer, N. Y. Yao, M. Kubo, H. J. Noh, P. K. Lo, H. Park, and M. D. Lukin. Nanometre-scale thermometry in a living cell. *Nature*, 500(7460):54–58, August 2013.

[66] Paul G. Kwiat, Andrew J. Berglund, Joseph B. Altepeter, and Andrew G. White. Experimental Verification of Decoherence-Free Subspaces. *Science*, 290(5491):498–501, October 2000.

[67] Abdelghani Laraoui, Jonathan S. Hodges, and Carlos A. Meriles. Magnetometry of random ac magnetic fields using a single nitrogen-vacancy center. *Applied Physics Letters*, 97(14):143104, October 2010.

[68] Abdelghani Laraoui and Carlos A. Meriles. Approach to Dark Spin Cooling in a Diamond Nanocrystal. *ACS Nano*, 7(4):3403–3410, April 2013.

[69] D. A. Lidar, I. L. Chuang, and K. B. Whaley. Decoherence-Free Subspaces for Quantum Computation. *Physical Review Letters*, 81(12):2594–2597, September 1998.

[70] S. Liggins, M. E. Newton, J. P. Goss, P. R. Briddon, and D. Fisher. Identification of the dinitrogen $\langle 001\rangle$ split interstitial H1a in diamond. *Physical Review B*, 81(8):085214, February 2010.

[71] Gang-Qin Liu, Xi Feng, Ning Wang, Quan Li, and Ren-Bao Liu. Coherent quantum control of nitrogen-vacancy center spins near 1000 kelvin. *Nature Communications*, 10(1):1344, March 2019.

[72] P. London, J. Scheuer, J.-M. Cai, I. Schwarz, A. Retzker, M. B. Plenio, M. Katagiri, T. Teraji, S. Koizumi, J. Isoya, R. Fischer, L. P. McGuinness, B. Naydenov, and F. Jelezko. Detecting and Polarizing Nuclear Spins with Double Resonance on a Single Electron Spin. *Physical Review Letters*, 111(6):067601, August 2013.

[73] J. H. N. Loubser and J. A. van Wyk. Electron spin resonance in the study of diamond. *Reports on Progress in Physics*, 41(8):1201–1248, August 1978.

[74] Zhi-Hao Ma, Zhi-Hua Chen, Jing-Ling Chen, Christoph Spengler, Andreas Gabriel, and Marcus Huber. Measure of genuine multipartite entanglement with computable lower bounds. *Physical Review A*, 83(6):062325, June 2011.

[75] J. R. Maze, P. L. Stanwix, J. S. Hodges, S. Hong, J. M. Taylor, P. Cappellaro, L. Jiang, M. V. Gurudev Dutt, E. Togan, A. S. Zibrov, A. Yacoby, R. L. Walsworth, and M. D. Lukin. Nanoscale magnetic sensing with an individual electronic spin in diamond. *Nature*, 455(7213):644–647, October 2008.

[76] Seth T. Merkel, Jay M. Gambetta, John A. Smolin, Stefano Poletto, Antonio D. Córcoles, Blake R. Johnson, Colm A. Ryan, and Matthias Steffen. Self-consistent quantum process tomography. *Physical Review A*, 87(6):062119, June 2013.

[77] V. Meyer, M. A. Rowe, D. Kielpinski, C. A. Sackett, W. M. Itano, C. Monroe, and D. J. Wineland. Experimental Demonstration of Entanglement-Enhanced Rotation Angle Estimation Using Trapped Ions. *Physical Review Letters*, 86(26):5870–5873, June 2001.

[78] B. A. Myers, A. Ariyaratne, and A. C. Bleszynski Jayich. Double-Quantum Spin-Relaxation Limits to Coherence of Near-Surface Nitrogen-Vacancy Centers. *Physical Review Letters*, 118(19):197201, May 2017.

[79] B. A. Myers, A. Das, M. C. Dartiailh, K. Ohno, D. D. Awschalom, and A. C. Bleszynski Jayich. Probing Surface Noise with Depth-Calibrated Spins in Diamond. *Physical Review Letters*, 113(2):027602, July 2014.

[80] Boris Naydenov, Friedemann Reinhard, Anke Lämmle, V. Richter, Rafi Kalish, Ulrika F. S. D'Haenens-Johansson, Mark Newton, Fedor Jelezko, and Jörg Wrachtrup. Increasing the coherence time of single electron spins in diamond by high temperature annealing. *Applied Physics Letters*, 97(24):242511, December 2010.

[81] P. Neumann, I. Jakobi, F. Dolde, C. Burk, R. Reuter, G. Waldherr, J. Honert, T. Wolf, A. Brunner, J. H. Shim, D. Suter, H. Sumiya, J. Isoya, and J. Wrachtrup. High-Precision Nanoscale Temperature Sensing Using Single Defects in Diamond. *Nano Letters*, 13(6):2738–2742, June 2013.

[82] Leigh M. Norris, Dennis Lucarelli, Virginia M. Frey, Sandeep Mavadia, Michael J. Biercuk, and Lorenza Viola. Optimally band-limited spectroscopy of control noise using a qubit sensor. *Physical Review A*, 98(3):032315, September 2018.

[83] Leigh M. Norris, Gerardo A. Paz-Silva, and Lorenza Viola. Qubit Noise Spectroscopy for Non-Gaussian Dephasing Environments. *Physical Review Letters*, 116(15):150503, April 2016.

[84] A. Omran, H. Levine, A. Keesling, G. Semeghini, T. T. Wang, S. Ebadi, H. Bernien, A. S. Zibrov, H. Pichler, S. Choi, J. Cui, M. Rossignolo, P. Rembold, S. Montangero, T. Calarco, M. Endres, M. Greiner, V. Vuletić, and M. D. Lukin. Generation and manipulation of Schrödinger cat states in Rydberg atom arrays. *Science*, 365(6453):570–574, August 2019.

[85] Christian Osterkamp, Johannes Lang, Jochen Scharpf, Christoph Müller, Liam Paul McGuinness, Thomas Diemant, R. Jürgen Behm, Boris Naydenov, and Fedor Jelezko. Stabilizing shallow color centers in diamond created by nitrogen delta-doping using SF6 plasma treatment. *Applied Physics Letters*, 106(11):113109, March 2015.

[86] Preeti Ovartchaiyapong, Kenneth W. Lee, Bryan A. Myers, and Ania C. Bleszynski Jayich. Dynamic strain-mediated coupling of a single diamond spin to a mechanical resonator. *Nature Communications*, 5(1):4429, July 2014.

[87] G. Massimo Palma, Kalle-Antti Suominen, and Artur K. Ekert. Quantum Computers and Dissipation. *Proceedings of the Royal Society of London. Series A: Mathematical, Physical and Engineering Sciences*, 452(1946):567–584, December 1996.

[88] Asher Peres. Separability Criterion for Density Matrices. *Physical Review Letters*, 77(8):1413–1415, August 1996.

[89] Linh M. Pham, Stephen J. DeVience, Francesco Casola, Igor Lovchinsky, Alexander O. Sushkov, Eric Bersin, Junghyun Lee, Elana Urbach, Paola Cappellaro, Hongkun Park, Amir Yacoby, Mikhail Lukin, and Ronald L. Walsworth. NMR technique for determining the depth of shallow nitrogen-vacancy centers in diamond. *Physical Review B*, 93(4):045425, January 2016.

[90] Yuting Ping, Brendon W. Lovett, Simon C. Benjamin, and Erik M. Gauger. Practicality of Spin Chain Wiring in Diamond Quantum Technologies. *Physical Review Letters*, 110(10):100503, March 2013.

[91] Dinesh Pinto, Domenico Paone, Bastian Kern, Tim Dierker, René Wieczorek, Aparajita Singha, Durga Dasari, Amit Finkler, Wolfgang Harneit, Jörg Wrachtrup, and Klaus Kern. Readout and control of an endofullerene electronic spin. *Nature Communications*, 11(1):6405, December 2020.

[92] M. Pompili, S. L. N. Hermans, S. Baier, H. K. C. Beukers, P. C. Humphreys, R. N. Schouten, R. F. L. Vermeulen, M. J. Tiggelman, L. dos Santos Martins, B. Dirkse, S. Wehner, and R. Hanson. Realization of a multinode quantum network of remote solid-state qubits. *Science*, 372(6539):259–264, April 2021.

[93] Andreas Reiserer, Norbert Kalb, Machiel S. Blok, Koen J. M. van Bemmelen, Tim H. Taminiau, Ronald Hanson, Daniel J. Twitchen, and Matthew Markham. Robust Quantum-Network Memory Using Decoherence-Protected Subspaces of Nuclear Spins. *Physical Review X*, 6(2):021040, June 2016.

[94] Y. Romach, C. Müller, T. Unden, L. J. Rogers, T. Isoda, K. M. Itoh, M. Markham, A. Stacey, J. Meijer, S. Pezzagna, B. Naydenov, L. P. McGuinness, N. Bar-Gill, and F. Jelezko. Spectroscopy of Surface-Induced Noise Using Shallow Spins in Diamond. *Physical Review Letters*, 114(1):017601, January 2015.

[95] E. L. Rosenfeld, L. M. Pham, M. D. Lukin, and R. L. Walsworth. Sensing Coherent Dynamics of Electronic Spin Clusters in Solids. *Physical Review Letters*, 120(24):243604, June 2018.

[96] L. G. Rowan, E. L. Hahn, and W. B. Mims. Electron-Spin-Echo Envelope Modulation. *Physical Review*, 137(1A):A61–A71, January 1965.

[97] Filip Rozpędek, Raja Yehia, Kenneth Goodenough, Maximilian Ruf, Peter C. Humphreys, Ronald Hanson, Stephanie Wehner, and David Elkouss. Near-term quantum-repeater experiments with nitrogen-vacancy centers: Overcoming the limitations of direct transmission. *Physical Review A*, 99(5):052330, May 2019.

[98] S. Sangtawesin, T. O. Brundage, Z. J. Atkins, and J. R. Petta. Highly tunable formation of nitrogen-vacancy centers via ion implantation. *Applied Physics Letters*, 105(6):063107, August 2014.

[99] Romana Schirhagl, Kevin Chang, Michael Loretz, and Christian L. Degen. Nitrogen-Vacancy Centers in Diamond: Nanoscale Sensors for Physics and Biology. *Annual Review of Physical Chemistry*, 65(1):83–105, 2014.

[100] Lukas Schlipf, Thomas Oeckinghaus, Kebiao Xu, Durga Bhaktavatsala Rao Dasari, Andrea Zappe, Felipe Fávaro de Oliveira, Bastian Kern, Mykhailo Azarkh, Malte Drescher, Markus Ternes, Klaus Kern, Jörg Wrachtrup, and Amit Finkler. A molecular quantum spin network controlled by a single qubit. *Science Advances*, 3(8):e1701116, August 2017.

[101] P.W. Shor. Fault-tolerant quantum computation. In *Proceedings of 37th Conference on Foundations of Computer Science*, pages 56–65, October 1996.

[102] Chao Song, Kai Xu, Hekang Li, Yuran Zhang, Xu Zhang, Wuxin Liu, Qiujiang Guo, Zhen Wang, Wenhui Ren, Jie Hao, Hui Feng, Heng Fan, Dongning Zheng, Dawei Wang, H. Wang, and Shiyao Zhu. Observation of multi-component

atomic Schr\"odinger cat states of up to 20 qubits. *arXiv:1905.00320 [quant-ph]*, May 2019.

[103] Andrew M. Steane. Overhead and noise threshold of fault-tolerant quantum error correction. *Physical Review A*, 68(4):042322, October 2003.

[104] Won Kyu Calvin Sun, Alexandre Cooper, and Paola Cappellaro. Improved entanglement detection with subspace witnesses. *Physical Review A*, 101(1):012319, January 2020.

[105] Youngkyu Sung, Félix Beaudoin, Leigh M. Norris, Fei Yan, David K. Kim, Jack Y. Qiu, Uwe von Lüpke, Jonilyn L. Yoder, Terry P. Orlando, Simon Gustavsson, Lorenza Viola, and William D. Oliver. Non-Gaussian noise spectroscopy with a superconducting qubit sensor. *Nature Communications*, 10(1):3715, September 2019.

[106] A. O. Sushkov, I. Lovchinsky, N. Chisholm, R. L. Walsworth, H. Park, and M. D. Lukin. Magnetic Resonance Detection of Individual Proton Spins Using Quantum Reporters. *Physical Review Letters*, 113(19):197601, November 2014.

[107] P. Szańkowski, G. Ramon, J. Krzywda, D. Kwiatkowski, and \L Cywiński. Environmental noise spectroscopy with qubits subjected to dynamical decoupling. *Journal of Physics: Condensed Matter*, 29(33):333001, July 2017.

[108] Piotr Szańkowski, Marek Trippenbach, and Łukasz Cywiński. Spectroscopy of cross correlations of environmental noises with two qubits. *Physical Review A*, 94(1):012109, July 2016.

[109] Susumu Takahashi, Ronald Hanson, Johan van Tol, Mark S. Sherwin, and David D. Awschalom. Quenching Spin Decoherence in Diamond through Spin Bath Polarization. *Physical Review Letters*, 101(4):047601, July 2008.

[110] T. H. Taminiau, J. Cramer, T. van der Sar, V. V. Dobrovitski, and R. Hanson. Universal control and error correction in multi-qubit spin registers in diamond. *Nature Nanotechnology*, 9(3):171–176, March 2014.

[111] T. H. Taminiau, J. J. T. Wagenaar, T. van der Sar, F. Jelezko, V. V. Dobrovitski, and R. Hanson. Detection and Control of Individual Nuclear Spins Using a Weakly Coupled Electron Spin. *Physical Review Letters*, 109(13):137602, September 2012.

[112] J. M. Taylor, P. Cappellaro, L. Childress, L. Jiang, D. Budker, P. R. Hemmer, A. Yacoby, R. Walsworth, and M. D. Lukin. High-sensitivity diamond magnetometer with nanoscale resolution. *Nature Physics*, 4(10):810–816, October 2008.

[113] Anna Tchebotareva, Sophie L. N. Hermans, Peter C. Humphreys, Dirk Voigt, Peter J. Harmsma, Lun K. Cheng, Ad L. Verlaan, Niels Dijkhuizen, Wim de

Jong, Anaïs Dréau, and Ronald Hanson. Entanglement between a Diamond Spin Qubit and a Photonic Time-Bin Qubit at Telecom Wavelength. *Physical Review Letters*, 123(6):063601, August 2019.

[114] David M. Toyli, Christoph D. Weis, Gregory D. Fuchs, Thomas Schenkel, and David D. Awschalom. Chip-Scale Nanofabrication of Single Spins and Spin Arrays in Diamond. *Nano Letters*, 10(8):3168–3172, August 2010.

[115] Matthew E. Trusheim and Dirk Englund. Wide-field strain imaging with preferentially aligned nitrogen-vacancy centers in polycrystalline diamond. *New Journal of Physics*, 18(12):123023, December 2016.

[116] J. A. van Wyk and G. S. Woods. Electron spin resonance of excited states of the H3 and H4 centres in irradiated type Ia diamonds. *Journal of Physics: Condensed Matter*, 7(29):5901–5911, July 1995.

[117] Uwe von Lüpke, Félix Beaudoin, Leigh M. Norris, Youngkyu Sung, Roni Winik, Jack Y. Qiu, Morten Kjaergaard, David Kim, Jonilyn Yoder, Simon Gustavsson, Lorenza Viola, and William D. Oliver. Two-Qubit Spectroscopy of Spatiotemporally Correlated Quantum Noise in Superconducting Qubits. *PRX Quantum*, 1(1):010305, September 2020.

[118] Vadim Vorobyov, Sebastian Zaiser, Nikolas Abt, Jonas Meinel, Durga Dasari, Philipp Neumann, and Jörg Wrachtrup. Quantum Fourier transform for nanoscale quantum sensing. *npj Quantum Information*, 7(1):1–8, August 2021.

[119] Junfeng Wang, Fupan Feng, Jian Zhang, Jihong Chen, Zhongcheng Zheng, Liping Guo, Wenlong Zhang, Xuerui Song, Guoping Guo, Lele Fan, Chongwen Zou, Liren Lou, Wei Zhu, and Guanzhong Wang. High-sensitivity temperature sensing using an implanted single nitrogen-vacancy center array in diamond. *Physical Review B*, 91(15):155404, April 2015.

[120] Zhi-Hui Wang and Susumu Takahashi. Spin decoherence and electron spin bath noise of a nitrogen-vacancy center in diamond. *Physical Review B*, 87(11):115122, March 2013.

[121] Ken X. Wei, Isaac Lauer, Srikanth Srinivasan, Neereja Sundaresan, Douglas T. McClure, David Toyli, David C. McKay, Jay M. Gambetta, and Sarah Sheldon. Verifying Multipartite Entangled GHZ States via Multiple Quantum Coherences. *arXiv:1905.05720 [quant-ph]*, May 2019.

[122] N. Y. Yao, Z.-X. Gong, C. R. Laumann, S. D. Bennett, L.-M. Duan, M. D. Lukin, L. Jiang, and A. V. Gorshkov. Quantum logic between remote quantum registers. *Physical Review A*, 87(2):022306, February 2013.

[123] N. Y. Yao, L. Jiang, A. V. Gorshkov, P. C. Maurer, G. Giedke, J. I. Cirac, and M. D. Lukin. Scalable architecture for a room temperature solid-state quantum information processor. *Nature Communications*, 3(1):800, April 2012.

[124] Tatsuro Yuge, Susumu Sasaki, and Yoshiro Hirayama. Measurement of the Noise Spectrum Using a Multiple-Pulse Sequence. *Physical Review Letters*, 107(17):170504, October 2011.

[125] Chong Zu, Francisco Machado, Bingtian Ye, Soonwon Choi, Bryce Kobrin, Thomas Mittiga, Satcher Hsieh, Prabudhya Bhattacharyya, Matthew Markham, Dan Twitchen, Andrey Jarmola, Dmitry Budker, Chris R. Laumann, Joel E. Moore, and Norman Y. Yao. Emergent hydrodynamics in a strongly interacting dipolar spin ensemble. *arXiv:2104.07678 [cond-mat, physics:quant-ph]*, April 2021.